TAMPEREEN TEKNILLINEN YLIOPISTO
TAMPERE UNIVERSITY OF TECHNOLOGY

Anssi Arffman

Numerical and Experimental Study on Inertial Impactors

Julkaisu 1372 • Publication 1372

Tampere 2016

Tampereen teknillinen yliopisto. Julkaisu 1372
Tampere University of Technology. Publication 1372

Anssi Arffman

Numerical and Experimental Study on Inertial Impactors

Thesis for the degree of Doctor of Science in Technology to be presented with due permission for public examination and criticism in Tietotalo Building, Auditorium TB109, at Tampere University of Technology, on the 19th of February 2016, at 12 noon.

Tampereen teknillinen yliopisto - Tampere University of Technology
Tampere 2016

Doctoral candidate: Anssi Arffman, M. Sc.
Aerosol Physics Laboratory
Department of Physics
Tampere University of Technology

Supervisor: Jorma Keskinen, prof.
Aerosol Physics Laboratory
Department of Physics
Tampere University of Technology

Pre-examiners: Chuen-Jinn Tsai, prof.
Institute of Environmental Engineering
National Chiao Tung University
Taiwan

Jason Olfert, assoc. prof.
Department of Mechanical Engineering
University of Alberta
Canada

Opponent: Ismo K. Koponen, Ph.D.
National Research Centre for the Working Environment
Denmark

ISBN 978-952-15-3703-5 (printed)
ISBN 978-952-15-3704-2 (PDF)
ISSN 1459-2045

Abstract

One of the most important physical properties that defines the behavior of an aerosol particle is its size. Size defines to a great extent how particles behave in physical and chemical processes. Applying experimental and numerical methods, this thesis studies the fundamentals of the operation of impactors, the instruments that are used to measure the size of aerosol particles.

The first part of the thesis develops a CFD simulation approach, which is suitable for low pressure impactors and their verification. The CFD model is then used to the study parameters that affect the shape of a low pressure impactor's collection efficiency curve. The second part focuses on the applications of these findings by introducing two new impactors: a variable nozzle area impactor (VNAI), designed for detailed study of particle behavior in collisions, and a high-resolution low-pressure cascade impactor (HRLPI), used in combination with electrical detection to measure nanoparticle size distribution.

Simulations showed that the steepness of the collection efficiency curve depends on the uniformity of the impaction conditions in the impactor jet. Conditions were defined in terms of static pressure, velocity, and particle stopping distance profiles in the cross section of the jet. Uniform impaction conditions and a steep cut-curve were achieved at a short throat, low pressure impactor stage.

In the devised VNAI impactor, particles showed very uniform impaction velocities, a fact that was used to examine the critical velocity of the rebound of spherical silver particles. The critical velocities were several orders of magnitude lower than those for micron sized particles. This may be explained by a different material pair used in the experiments and previous studies. The HRLPI was designed based on instrument response simulations to gain maximum information on aerodynamic size distribution and to guarantee robust inversion characteristics in real-time measurement. This was achieved with roughly ten stages per size decade and with slit type, short-throat nozzles.

This thesis sheds light on some still unanswered questions in impactor theory and successfully applies the theory to practise by introducing new high resolution impactors for nanoparticle research

Aknowledgements

Research and development conducted in this study has been performed in the Aerosol Physics Laboratory of the Department of Physics at Tampere University of Technology during the years 2009 - 2015. I want to thank most sincerely my supervisor, professor Jorma Keskinen for his sharp-eyed guidance and offering me the inspiring workplace for several years. Professor Jyrki Mäkelä I would like to thank for introducing me to BUONAPART-E project that has trained my international co-operation skills. I am deeply grateful to Dr. Jaakko Yli-Ojanperä for his assistance in designing and calibrating the impactors, and for the many encouraging discussions at work and beyond. I want to thank Dr. Marko Marjamäki for the assistance in publishing the first paper of my thesis, and the recreational activities outside the office.

I have had pleasure to work with several young geniuses during these busy years. I want to acknowledge Mr. Heino Kuuluvainen for grabbing me into the fundamental aerosol physics research and sharing the authorship of the final paper. Mr. Juha Harra I would like to thank for keeping up uncompromising scientific quality in the measurements, and for the assistance in preparing manuscripts. Mr. Antti Rostedt and Dr. Panu Karjalainen I want to thank for sharing the office room for many years, and sharing your expertise in many fruitful discussions we have had in business, as well as, outside of the laboratory. I want to thank all co-authors of the papers. Each of you had a role there and you did it excellent. I acknowledge the whole Aerosol Physics Group personnel, also former members, for the helpful and pleasant working environment.

I want to thank official pre-examiners of my thesis, professor Chuen-Jinn Tsai and associate professor Jason Olfert. Your valuable comments and suggestions gave the final touch for the quality of thesis. I want to thank my opponent Dr. Ismo Koponen for accepting the invitation.

I want to thank all my friends for just being friends and staying my friends. Your contribution to my studies should not be underestimated. I want to thank my parents and family for being always interested in what I have been doing and especially for the early years that have far-reached impact on my studies. I want to thank Elsa and David for devoting on my education: your contribution has helped me a lot. Finally, I want to thank the two most important persons in my life. Iita, I want to thank you for sharing your life with me and for the support and understanding I have received during all the years. Eeli, our little chatter, I want to thank you for keeping dad's thoughts out of work for a couple of hours everyday.

This research has been funded by the European Unions Seventh Framework Programme (FP7/2007-2013) under the Grant Agreement n°280765 (BUONAPART-E). This thesis reflects only the authors' views, and the Community is not liable for any use made of the information contained therein.

Articles included in this thesis

Paper 1	Arffman, A., Marjamäki, M. and Keskinen, J., Simulation of low pressure impactor collection efficiency curves, *Journal of Aerosol Science*, 42, 329-340, 2011.
Paper 2	Arffman, A. and Yli-Ojanperä, J. and Keskinen, J., The influence of nozzle throat length on the resolution of a low pressure impactor – An experimental and numerical study, *Journal of Aerosol Science*, 53, 76–84, 2012.
Paper 3	Arffman, A., Kuuluvainen H., Harra J., Vuorinen, O., Juuti, P., Yli-Ojanperä, J., Mäkela, J., Keskinen J., The critical velocity of rebound determined for sub-micron silver particles with a variable nozzle area impactor *Journal of Aerosol Science*, 86, 32–43, 2015.
Paper 4	Arffman A., Yli-Ojanperä, J., Kalliokoski, J., Harra, J., Pirjola, L., Karjalainen, P., Rönkkö, T., Keskinen J., A high-resolution low-pressure cascade impactor, *Journal of Aerosol Science*, 78, 97–109, 2014.

Author's contribution to the publications

Paper 1: I carried out the simulations and wrote most of the paper.

Paper 2: I performed the simulations and measured most of the experimental results. I designed the critical dimensioning of the impactor stage and wrote most of the paper.

Paper 3: I designed the HRLPI cascade impactor. I performed the calibration measurements, and wrote most of the text. I participated to all laboratory test measurements.

Paper 4: We share equal contributions with Mr. Heino Kuuluvainen in preparing the study. I designed the variable nozzle area impactor, and performed all necessary simulations. I participated in measurements and data analysis.

Symbols and abbreviations

λ	Regularization parameter
$\mathbf{I}$	ELPI current vector
$\mathbf{K}$	Kernel matrix
$\mathbf{L}$	Second derivative matrix
μ	Gas viscosity
ρ_g	Gas density
ρ_p	Particle density
A_i	Stream line area (i:th particle)
C_c	Cunningham slip correction factor
C_i	Particle concentration
d_{80}, d_{50}, d_{20}	Particle sizes corresponding 80%, 50% and 20% collection efficiencies
E	Collection efficiency
E_i	Collection efficiency of the stage i
E_{ch}	Charging efficiency
f	Particle size distribution
I_i	Current of stage i
I_{ip}	Impaction parameter describes the impaction conditions
k_i	Kernel function of the stage i
L	Jet-to-plate distance
l	Effective tube length
L_S	Stopping distance of particle
P_{ip}	Pressure above impaction plate
S_{ip}	Particle stopping distance (distance from the collection plate where axial velocity is zero)
T	Nozzle throat length
V_j	Jet velocity
V_0	Particle velocity before impaction
V_{jet}	Average jet velocity
$v_{g,i}$	Gas flow velocity (i:th particle)
W	Nozzle diameter or width

AAC	Aerodynamic Aerosol Classifier
APM	Aerosol Particle Mass analyzer
APS	Aerodynamic Particle Sizer
BUONAPART-E	EU (FP7) project for scaling-up metal nanoparticle production
DMA	Differential mobility analyzer
DOS	Dioctylsebacate or diethylhexylsebacate
ECG	Evaporation-condensation particle generator
EEPS	Engine Exhaust Particle Sizer
ELPI	Electrical low pressure impactor
HRLPI	High-resolution low-pressure cascade impactor
LPI	Low pressure impactor
NanoSMPS	Nanoparticle Scanning Mobility Particle Sizer
PM	Particulate mass
SCAR	Single Charged Aerosol Reference
SEM	Scanning electron microscope
SMPS	Scanning mobility particle sizer
TEM	Transmission electron microscope
VNAI	Variable nozzle area impactor

Contents

Chapter 1

Introduction

Nanoparticles, which today constitute a broad field of research, belong to air pollutants, are frequently used in scientific research, and increasingly in engineering applications. They form via natural processes, such as the breathing of a pine tree cell (Kulmala et al., 2000) and in manmade processes, such as internal combustion (Kittelson, 1998). For engineering applications, such as fiber optics, they can also be produced synthetically (Hutter and Fendler, 2004; Kruis et al., 1998). In the above processes, nanoparticles exist at some point in an aerosol phase; that is, they comprise a system of carrier gas and particles suspended in it. In an aerosol, particles are in constant motion because of Brownian motion, turbulence in fluid flow, and possible external and internal forces. They can settle on surrounding surfaces, exchange vapors with the carrier gas, and agglomerate by sticking to each other in collisions. Because of their highly dynamic nature, an aerosol sample should be characterized by measuring it in real time whenever possible.

One of the most important physical properties that defines the behavior of an aerosol particle is its size. Size defines to a great extent how particles behave in physical and chemical processes, such as deposition, agglomeration, particle charging, and chemical reactions. Aerosol emitted from a single source has usually a logarithmic normal size distribution, and its size range can cover one to three orders of magnitude. This is why measuring the size distribution of an aerosol is usually a challenging task. Particle size is an ambiguously defined quantity, even with macroscopic objects. This is why in aerosol science particles are measured in equivalence sizes, which are defined based on how particles behave in physical processes. One widely used equivalent size is the aerodynamic size, which is defined through the terminal velocity of a particle. The aerodynamic size of a particle is the size of a spherical unit density ($1\,\mathrm{g\,cm^{-3}}$) particle, which has the same terminal velocity as a real particle. Depending on the size range, several different instruments can be used to measure the aerodynamic size of particles. This thesis studies one of the most widely used classes of instruments in aerosol science for measuring aerodynamic size, that is, impactors. In principle, an impactor impinges an aerosol stream on a surface. Particles with sufficient inertia separate from streamlines and impact on a surface and adhere there. In other words, the impactor classifies particles into two different size fractions. The particle size whose collection efficiency is 50% is called the cutpoint of the impactor. Impactor stages can be connected in series to measure the particle size distribution. Such impactors are known as cascade impactors.

Used for over 100 years to classify particles according to their size, impactors are a rather mature field of aerosol science. Impactor science focuses on understanding the shape of the collection efficiency curve and the cut-off size of the impactor. Besides collection efficiency, recent decades have witnessed studies on the impaction conditions and impaction velocities of particles. The current state of theory can now describe a change in the cut-off size with flow conditions (Hari et al., 2006; Mercer and Chow, 1968) and partly explain the non-ideal shape of the collection efficiency curve (Gómez-Moreno et al., 2002; Jurcik and Wang, 1995). Since 1970, impactor designs have followed the instructions based on the extensive study of Marple and Liu (1974), who numerically simulated the collection efficiency curves of laminar jet impactors as a function of numerous flow and geometry describing parameters. Several researchers have studied impactors experimentally and numerically. To mention a few, Biswas and Flagan (1984) and Flagan (1982) investigated the collection efficiency characteristics of a high jet velocity impactor, Kauppinen et al. (1986) studied the collection efficiency of a multi-nozzle cascade impactor, and Vinchurkar et al. (2009) numerically simulated a low jet velocity Andersen cascade impactor. To reach sub-100 nm cutpoints, Stern et al. (1962) introduced low pressure impactors. In a low pressure impactor, the cutpoint is reduced by increasing the slip correction factor by decreasing pressure.

Several researchers have introduced a variety of impactors for various applications. The most widely used are probably standard particulate mass impactors (PM). They are used as part of research setups and instruments to remove large particles from an aerosol sample or to measure the mass concentration of a particular size fraction. The best known cascade impactors are probably the Andersen impactor (Andersen, 1985), which was developed originally for size fractionation of viable airborne particles, and the Berner impactor (Berner, 1972), which has been used to measure particle mass distribution in the range of approximately 100 nm to 10 µm. The latest significant effort in impactor technology is probably the development of the Electrical Low Pressure Impactor (ELPI) by Keskinen et al. (1992). They succeeded in combining electrical detection of particles and cascade impactor measurement techniques, enabling thus measurement of size distribution in real time. The ELPI has been further studied in detail by Marjamäki et al. (2005); Marjamäki (2003); Marjamäki et al. (2000).

Though impactors are of straightforward construction and have been used for a long time in aerosol research, the non-ideal shape of the collection efficiency curve remains an unanswered question, which involves especially low pressure impactors. If the shape of the collection efficiency curve could be made sharper, new opportunities would open up for measuring size distribution and studying nanoparticle collisions. With sharp cut-curve impactor stages, the cutpoints of a cascade impactor could be packed more densely to allow an increase in size resolution. Densely packed cutpoints automatically minimize the greatest source of error especially in impactor measurement, the particle bounce. A sharp cut-curve also leads to uniform impaction velocities of monodisperse particles, which helps to study particle properties via controlled energy impactions. In this thesis, sharp cut-curve impactors are developed by understanding the fundamental phenomena underlying the operation of a low pressure impactor.

1.1 Objectives and scope

Over the last decades, interest in aerosol research has been drawn to nanometer size particles, a focus that has set new challenges for particle size and characterization instruments. Class of impactors, capable of measuring nanoparticles, apply generally high jet velocity and low operation pressure to bring the cutpoints to the sub-micron range. However, the details of low pressure impactors have not yet been fully worked out. For example, the shape of the collection efficiency curve cannot yet be controlled in the light of current knowledge. Yet such control is a necessary prerequisite, for example, to increase the size resolution of cascade impactors, because collection efficiency curves must rapidly increase with particle size to bring the cutpoints close to each other without creating cross talk between consecutive stages. In this case, interpretation of measurement results is straightforward, because the collection efficiency curves of the impactor can be approximated with step functions (the cutpoint concept, see, for example, Kauppinen et al. (1986); Keskinen et al. (1992)).

Low pressure impactors have also been used to study the properties of particles by observing their behavior as a function of impaction velocity in low pressure impactors (Friedlander, 1999; Ihalainen et al., 2014; Virtanen et al., 2010). In these applications, it is inherently important to be able to reliably predict the impaction velocity of the studied particles to control the impaction energy. Because currently impaction velocity cannot be measured for nanoparticles by direct optical measurement, numerical simulation methods must be used instead. To be able to correctly predict impaction velocities, simulation methods must be properly validated, and their operational limits must be recognized.

This thesis strives to answer the still open questions about traditional low pressure impactors:

- Which factors determine the shape of an impactor's collection efficiency curve?
- What type of information can we extract reliably with a numerical impactor model?
- What are the impaction velocities of different size particles in a low pressure impactor and what affects their velocities?
- What is the optimal number of stages and the shape of the collection efficiency curve in a low pressure cascade impactor?

The thesis aims to study in detail the operation of low pressure impactors. The first goal is to develop numerical simulation methods to study the details of the impactor flow field and to explain the relation between the shape of the collection efficiency curve and the flow field properties (**Papers 1** and **2**). The second goal is to apply the knowledge gained by simulations to practice by building and characterizing a new, high-resolution, low-pressure cascade impactor (HRLPI) and a variable nozzle area impactor (VNAI) (**Papers 3** and **4**). The HRLPI is used to measure nanoparticle size distributions under 150nm and the VNAI to study the properties of particles under well known impaction conditions.

Chapter 2

Background

2.1 Instruments to measure particle size

Instruments to measure aerosol particle size distribution can be divided into different categories based on their physical measurement principle. The upper panel in Figure 2.1 maps, in terms of channel resolution and measurement size range, several commercially available or generally known size distribution measurement instruments. The instruments shown in solid lines are real-time (second resolution) and those in dashed lines semi-continuous (minute resolution). References are shown in Figure 2.1. The aerosol particle mass analyzer (APM) classifies particles according to their charge/mass ratio and can be used to measure the particle mass distribution. The aerosol aerodynamic classifier (AAC) classifies particles respect to their aerodynamic size utilizing a centripetal force. It operates without charging and can be used in combination with a particle counter to measure the aerodynamic size distribution. The nanoparticle scanning mobility particle sizer (NanoSMPS) and the Engine exhaust particle sizer (EEPS) measure the size distribution as a function of mobility size and the LASAIR II as a function of optical particle size. The aerodynamic particle sizer (APS) measures the aerodynamic particle size distribution in real time by optical detection. The ELPI+ is an electrical low pressure impactor, which measures the aerodynamic size distribution in real time by electrical detection of particles.

The lower panel in Figure 2.1 compares nominal size resolutions and the measurement size ranges of different cascade impactors. The Andersen, NanoMOUDI, and BernerLPI are commercially available cascade impactors, and the HRLPI is a new cascade impactor introduced in **Paper 4**. The ELPI+ impactor is the cascade impactor used in the ELPI+ instrument. The Andersen, NanoMOUDI, and BernerLPI are cascade impactors for collecting size classified aerosol samples for off-line chemical and mass analysis. Because the HRLPI is fitted in an ELPI instrument body, it can be used for real-time measurement as well.

Comparison of instrument size resolutions is only one narrow aspect of instrument resolution. For example, time resolution and instrument sensitivity are equal or even more important aspects, depending on the case studied. Because they have very narrow measurement channels, differential mobility analyzer (DMA) based instruments may have much higher nominal size resolutions than the ELPI+. The drawback is that their time-resolution is poor compared to the ELPI+ (roughly 15 - 200 s versus 1 s).

Mobility-based instruments based on multiple parallel current measurements (Mirme, 1994; Tammet et al., 2002) include the EEPS and DMS500. They offer a similar or slightly better time resolution than the ELPI+. The HRLPI impactor combined with the ELPI current measurement technology and the EEPS have very similar performance in terms of channel/size range, time-resolution, and sensitivity. The biggest differences are their physical size classification principles, and the fact that in the EEPS also the size classification depends on the charge state of particles. Thus, the EEPS must perform a complicated deconvolution in real time because the current caused by multiply charged particles must be compensated from measurement results. In the HRLPI, the simple cutpoint concept (see, for example, Kauppinen et al. (1986); Keskinen et al. (1992)) is in most cases already enough to determine the shape of the original particle size distribution. The dependency of the size classification on the particle charge state ultimately limits the maximum size that can be measured with the mobility based methods (Levin et al., 2015). The ELPI-type measurement is not limited in large particle sizes by the multiple charging problem, but it is limited by the fine particle losses to the upper stages of impactor when measuring micron sized particles (Moisio et al., 1999).

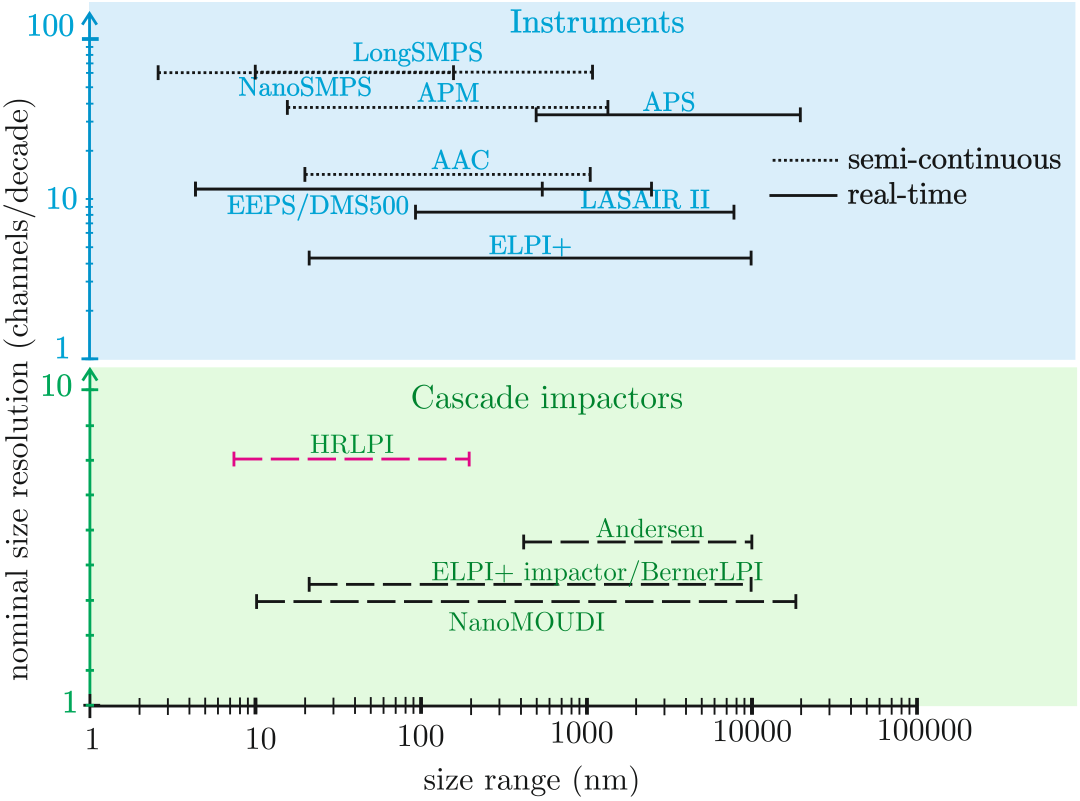

Figure 2.1: Instruments and cascade impactors mapped according to their nominal size resolutions and measurement size ranges. Size resolution is defined as the number of measurement channels per particle size decade. The SMPS, NanoSMPS (Chen et al., 1998), EEPS (Johnson et al., 2004), and APS (Chen et al., 1985) are commercial instruments by TSI, DMS500 (Reavell et al., 2002) and AAC (Tavakoli and Olfert, 2013) by Cambustion Ltd., the APM (Ehara et al., 1996) by Kanomax , the ELPI+ (Järvinen et al., 2014) by Dekati Ltd., and the LASAIR II by Particle Measuring Systems. The NanoMOUDI is a cascade impactor manufactured by MSP, the BernerLPI a cascade impactor by Hauke (BLPI25/0.018 (Stefancová et al., 2011)), and the Andersen a cascade impactor by Copley Ltd. The HRLPI is a cascade impactor developed in **Paper 3**.

2.2 Inertial classification of particles

In an impactor, an aerosol sample is forced to flow through an accelerating nozzle and to form a jet. The jet impinges on the collection substrate after the accelerating nozzle, and particles with sufficient inertia separate from the stream lines. Figure 2.2 (a) shows schematically tracks of different size particles in an impactor nozzle, and in the background colors show the simulated gas velocity field in a high velocity impactor jet.

Figure 2.2 (b) shows schematically the collection efficiency curve of a single impactor stage. Impaction collection begins at the cutpoint (d_{50}) and increases towards increasing particle size. The cutpoint is the particle size at which the impactor collects 50% of sample particles. In an ideal impactor, collection efficiency would be a step function located at d_{50}, but in real impactors it is rounded from both ends of the S-curve (Fuchs, 1978; Hinds, 1998). Details of the shape of the impaction curve are further discussed in the 4.1, as the study seeks to shed light on the topic. After the cutpoint, the collection efficiency starts to decrease because of particle rebound or bounce from the collection substrate. The bounce effect gets enhanced for increasing particle size for two main reasons: the critical velocity of the rebound decreases with particle size, as shown by Dahneke (1971), and the impaction velocity of particles increases (Marple, 1970). In the size range of below 10 nm, the collection efficiency curve rises because of secondary collection mechanisms: diffusion and image charge (de la Mora et al., 1990). Diffusion losses are caused by the Brownian motion of small particles as particles drift toward a decreasing concentration gradient. When a charged particle is brought close to a metallic wall, it induces a similar magnitude but an opposite-sign electrical charge at the wall. The induced charge then pulls the particle towards the wall, generating particle losses.

The impactor cutpoint can be characterized with the critical Stokes number (Stk_{50}). The Stokes number describes the ratio of the particle stopping distance to a characteristic dimension of the flow curvature. Ideally, if the geometry remains constant, the critical Stokes number of the impactor is constant. This allows prediction of the impactor cutpoint if jet velocity, operation temperature, or pressure are changed. However, when flow conditions are changed, also the jet Reynolds number changes. Within a certain Reynolds number and geometry limits, the critical Stokes number remains fairly constant. The Re and Stk_{50} number can be written for an impactor as follows:

$$Re = \frac{\rho_g V_j W}{\mu} \tag{2.1}$$

$$Stk_{50} = \frac{L_S}{W/2} = \frac{\rho_p C_c V_0 d_{50}^2}{9\mu W}, \tag{2.2}$$

where ρ_g is the gas density, V_j the jet velocity, L_S the stopping distance of a particle, ρ_p the particle density, C_c Cunningham slip correction factor, d_{50} the cutpoint of the stage, and μ the gas viscosity.

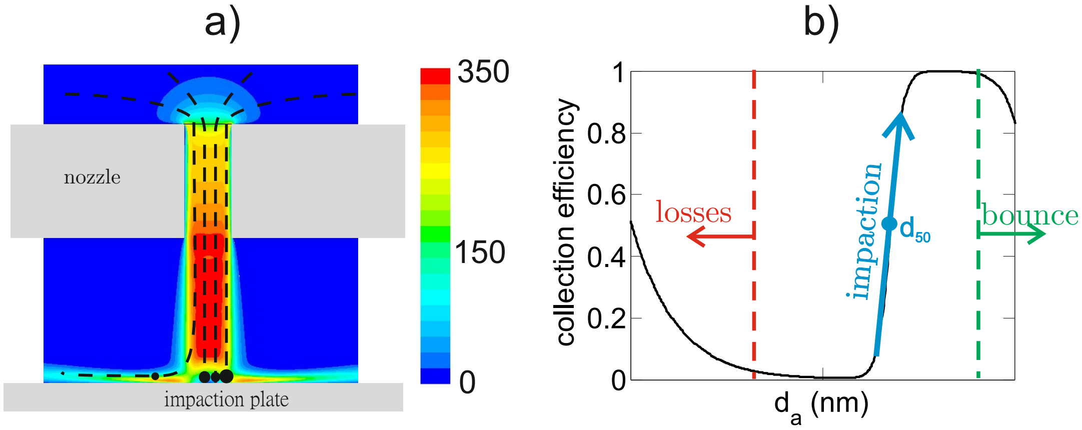

Figure 2.2: In panel a) a schematic of the impactor stage and particle tracks. Color shows velocity. In panel b) a schematic collection efficiency curve of impactor stage.

2.3 Effect of various parameters on resolution

The steepness of an impactor's collection efficiency curve can be regarded as a measure of the stage resolution. It describes the minimum difference in particle size that can be distinghuished by the impactor. Parameters that affect the resolution of an impactor include at least the flow conditions, geometry, and collection substrate properties, such as the surface structure. A thorough review on impactor resolution is compiled by Fuchs (1978) and more recently by Marple and Olson (2011). To reach low cutpoints low pressure impactors (LPI) are utilized. In general the resolution is deteriorated when moving from atmospheric to low pressure conditions, and thus we focus in this thesis to LPIs.

2.3.1 Flow conditions

Figure 2.3 (a) shows important geometrical parameters that characterize impactor operation. Besides geometrical parameters, the Reynolds (Equation (2.2)) numbers of impactors must be similar to guarantee the similarity of impactor flow fields. The primary study on the effect of impactor parameters on impactor operation is by Marple and Liu (1974). They solved numerically the particle tracks and collection efficiencies of laminar atmospheric jet impactors and found that the shape of the collection efficiency curve remains rather sharp and the critical Stokes number constant when the S/W-ratio is in the range of 1 - 5 and Re is in the range of 500 - 3000. Marple deduced from his simulation results that when the collection plate is too far, the jet dissipates and a parabolic velocity profile is formed. This means that particles at different radial distances from the center of the jet have different normal velocities, and that the center of the jet consequently collects smaller particles. The Reynolds number describes the ratio of inertia and friction forces and indicates the shape of the velocity profile after the nozzle. If the number is below 500, a laminar velocity profile develops in the nozzle. The center of the jet starts to collect smaller particles than the boundaries of the jet, where the fluid velocity remains essentially zero because of solid walls. If Re is above 3000, the flow can become turbulent and result in a poor steepness of collection efficiency. Marple also showed that the jet is compressed closer to a collection plate with a high Re, resulting in a shift in the critical Stokes number.

Jurcik and Wang (1995) studied numerically the effect of aerodynamic focusing on the shape of the collection curve of an atmospheric pressure impactor. In their study, they compared collection efficiencies produced by a straight wall nozzle and a nozzle with a gradually converging inlet. They found that when the nozzle was straight walled aerodynamic focusing enriched particles towards the center of the nozzle axis. This means that particles have a more uniform velocity profile in a straight wall nozzle than in a converging nozzle; consequently, the collection efficiency curve of a straight wall nozzle is sharper than that of a gradually converging nozzle.

Only a few systematic, experimental studies are available on impactor resolution. Gómez-Moreno et al. (2002) studied turbulence transition in a low pressure impactor jet and the effect of the collection plate distance on resolution. However, their collection plate distance results cannot be generalized, because they used an impactor preceded by an aerodynamic lens system that focused particles on the symmetry axis of the nozzle. Their experimental setup was optimized to detect the transition from laminar to turbulent flow.

Instead of systematic studies on impactor resolution, a number of papers describe a new type of impactor or cascade impactor, and most studies report calibration results of collection efficiency curves. Figure 2.3 compiles the steepnesses of several commercially available or generally known impactors as a function of three different parameters. Steepness is defined as the ratio of particle sizes corresponding to 80% and 20% collection efficiencies (d_{80}/d_{20}). The closer the steepness parameter is to the value one, the steeper is the change in collection efficiency at the cutpoint. Figure (b) presents the effect of the Re-number on steepness. In general, steepness decreases towards increasing Re-values, but with small Re-numbers, the value of steepness is not determined by the Reynolds number. Figures (c) and

(d) show the effect of jet-to-plate distance and nozzle throat length on the steepness parameter. The deviation is rather large, but the trend seems to be that a shorter jet-to-plate and nozzle throat length increases steepness. A short throat length leaves the jet velocity profile under-developed. A short jet-to-plate distance minimizes dissipation in the free jet, which in turn prevents the development of the velocity profile. In each figure, the other two parameters are limited according to Marple's impactor design criteria. Nevertheless, there is a weak trend in the steepness in figures 2.3 (b), (c), and (d), we can conclude that the measured steepnesses derive either from measurement errors or, for example, from the quality of

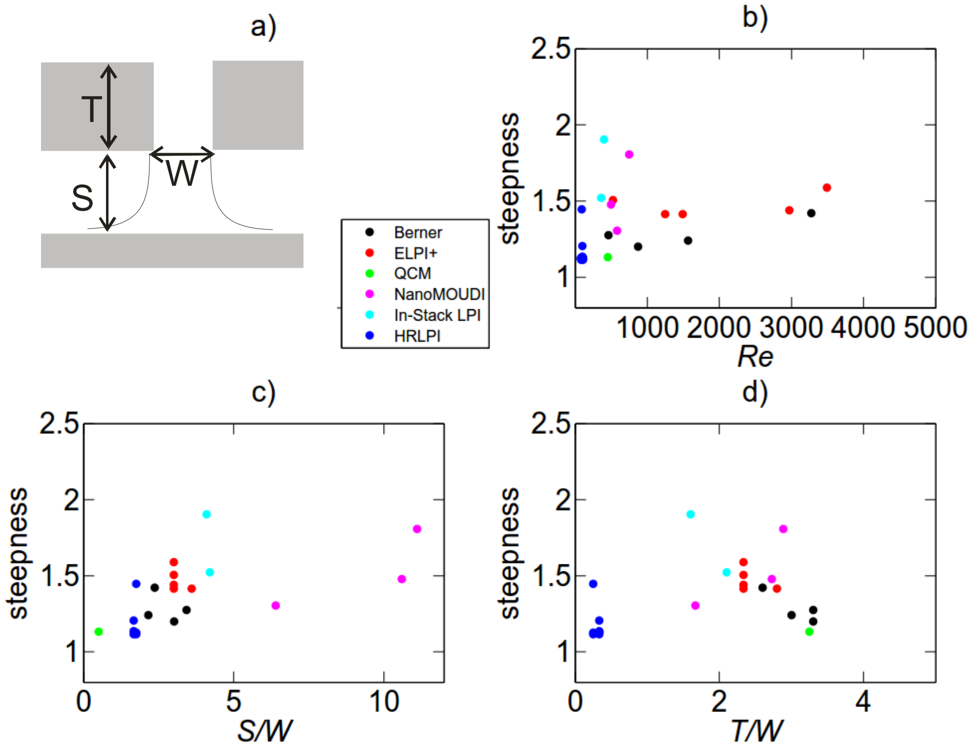

Figure 2.3: a) shows the critical dimensions of an impactor, and figures b), c), and d) show the effect of jet Reynolds number, jet-to-plate distance, and nozzle throat length on the steepness of collection efficiency curve (defined as ratio of particle sizes d_{80}/d_{20}), respectively. Results are extracted from published experimental collection efficiencies ($d_{50} < 200\,\mathrm{nm}$). The cascade impactors are a 10-stage Berner impactor (Stefancová et al., 2011), an ELPI+ (Järvinen et al., 2014), a QCM (Hering, 1987), a MOUDI (Marple et al., 1991), an In-stack low pressure impactor (Vanderpool et al., 1990), and an HRLPI (**Paper 4**).

2.3.2 Collection substrate

The roughness of the collection plate decreases the cutpoint of an impactor and reduces the steepness of the collection efficiency curve. Earlier research is not clear on how the cutpoint is reduced. One suggestion is that surface roughnesses penetrate the boundary layer that is formed above the collection substrate. Some of the flow then encounters roughnesses that stick out of the boundary layer, and particles smaller than the cut-size may hit the micrometer size roughnesses. Porosity introduces similar effects but also excess collection efficiency; that is, collection efficiency does not decay to zero even at small Stokes numbers. Porosity forces part of the jet to penetrate the collection substrate, and a large portion of particles is filtered out from the penetrating fraction. This is the origin of an excessive collection efficiency. The effect of surface roughnesses has been studied, for example, numerically by Huang et al. (2001) and experimentally by Marjamäki and Keskinen (2004a,b).

2.3.3 Bounce

Particle bounce from the surface is a fundamental property of particle-surface interaction though it is also a source of measurement error in impactors. Particles may adhere to or rebound from the collection plate surface after impaction depending on their kinetic energy. Dissipative mechanisms are always present in impaction, and part of the kinetic energy is lost in it. When an intact particle has enough kinetic energy to overcome its energy losses and to climb out of the potential energy well of the surface, it rebounds. The impact velocity that a particle must have to rebound from the surface is called the critical velocity of rebound. Dahneke (1971) derived a theoretical equation for the critical velocity rebound for perfectly spherical particles from an infinite and smooth surface:

$$v_{crit} = \left(\frac{A(1 - C_R^2)}{\pi z_0 \rho_p C_R^2} \right)^{0.5} d_p^{-1}, \tag{2.3}$$

where A is Hamaker's constant, C_R the coefficient of restitution, z_0 the separation between the particle and surface in contact. Hamaker's constant describes the strength of adhesion between two materials. The coefficient of restitution is the ratio of the velocities of intact and bounced particles. In practical cases, the equation is difficult to apply to predicting bounce occurrence, because especially A and also C_R are a material pair specific and known only for a few materials. As shown by the equation, the critical velocity of rebound is theoretically inversely proportional to particle size.

Particle impaction velocity in the impactor is defined by jet velocity and particle size. At the cutpoint, the impaction velocity is close to zero and increases with particle size close to jet velocity (Ihalainen et al., 2014; Marple, 1970; Rennecken and Weber, 2013). Jet velocity in turn is defined by the pressure ratio of upstream and downstream stagnation pressures. With a straight nozzle geometry, the maximum jet velocity is limited by the velocity of sound ($350\,\mathrm{m\,s^{-1}}$) and is reached when the pressure drops roughly to a half in the nozzle. Thus a bounce can be avoided in the impactor by not allowing particles large compared to the cutpoint of the stage to pass the impactor, and by maintaining a low jet velocity. As predicted by Equation (2.3), for small particles, large jet velocities and a wide particle size range can be collected by a single impactor stage without bounce. One widely used method to inhibit bounce is to increase the adhesion between particle and collection plate (Rao and Whitby, 1977) by adding a vacuum grease coating on the collection plate. The method works fine, but after some loading of collection substrates, particles start to impact on other particles, and bounce may be initiated again (Marple and Olson, 2011).

Bounce is not necessarily only a source of error in the measurement, as mentioned above, but it has also been used as a tool to study, for example, the phase state of secondary organic aerosols (SOA, Virtanen et al. (2010)). Virtanen et al. found the amorphous phase state of SOA particles by comparing SMPS particle size distributions and ELPI current distributions. Their method was to simulate from SMPS data the current distributions of an ELPI. Then by observing the differences between simulated and measured current distributions, they concluded that SOA particles must bounce in the impactor of ELPI (Kuuluvainen et al., 2013). Over the last decades, studies have been conducted in the field of engineered nanoparticles on the fragmentation and binding energy of agglomerates (Froeschke et al., 2003; Ihalainen et al., 2014; Seipenbusch et al., 2007, 2010). In these experiments, agglomerates have been impinged on a surface with controlled energy, and the level of their break-up has been observed.

2.4 Kernel functions of a cascade impactor

Kernel functions of a cascade impactor describe how particles are distributed between different stages. The sum of the kernels is one for each particle size. For the cascade impactor the kernel functions can be calculated by:

$$\begin{aligned} k_n(D_p) &= E_n(D_p) \\ k_i(D_p) &= E_i(D_p) \prod_{j=i+1}^{n} [1 - E_j(Dp)], i = (0), 1, ..., n-1, \end{aligned} \tag{2.4}$$

where E_n is the highest cutpoint stage collection efficiency and index $i = 0$ corresponds to the filter stage. E_j:s include also the particle losses that are caused by diffusion and image charging effects. E_j:s are calculated with the following equations:

$$E_j = 1 - (1 - E_j^I)(1 - E_j^S), \tag{2.5}$$

where E_j^I is the collection efficiency by impaction, and E_j^S is the collection efficiency by secondary collection mechanisms, i.e. diffusion and image charge. Conventionally, calibrated collection efficiencies are parameterized to calculate kernels. Parametrizations are composed of two parts: impaction collection (E^I) and diffusion losses (E^s; Brockmann, 2001), as shown in Equation (2.5). The fitted functions are of the form:

$$E^I = \left(1 + (d_{50}/d_p)^{2s}\right)^{-1} \tag{2.6}$$

$$E^S = 1 - e^{kSh} \tag{2.7}$$

$$k = \frac{\pi D l}{Q}$$

$$Sh = 3.66 + \frac{0.2672}{k + 0.10079k^{(1/3)}},$$

where d_{50} is the cutpoint of the stage, s a fitting parameter (describes the steepness of the collection efficiency curve), D the diffusion coefficient ($\mathrm{m^2\,s^{-1}}$), l the effective tube length (length of a tube with similar diffusion losses as the impactor stage) (m), and Q the volumetric flow rate ($\mathrm{m^3\,s^{-1}}$).

Figure 2.4 shows an example of cascade impactor kernel functions (line styles separate adjacent stages). The height of all kernels, except the highest cutpoint stage, are below one because collection efficiency curves of the consecutive stages overlap. Especially the kernel height of the lowest cutpoint stages are even below 0.5. This is because all the preceding stages collect by the secondary collection mechanisms particles that will deposit at the lowest cutpoint stages. Kernel functions can be used to calculate stage responses for a certain input. Because the ELPI uses electrical detection, the particle charger efficiency must be included in response simulation. Currents measured by the ELPI can be integrated from kernel functions by:

$$I_i = \int_0^{d_{p,max}} k_i(d_p) E_{ch}(d_p) f(d_p) dd_p, \tag{2.8}$$

where I_i is the current of stage i, $f(d_p)$ the particle size distribution and E_{ch} the charging efficiency. In theory, the input particle size distribution could be worked out from Equations (2.8) by discretizing the equations into discrete size bins and by numerically solving the derived matrix equation. In practice, the numerical properties of the matrix are such that a straightforward least-squares solution produces a wildly oscillating solution. Inversion methods are then needed to obtain a solution. With inversion problems, a priori information on a solution is used to obtain a physically meaningful solution. One of the simplest is Tikhonov regularization, which assumes a smoothness of solution (see, for example, Hansen (1998)).

By assuming that the k_i is zero elsewhere and one between the $d_{50,i} - d_{50,i+1}$, and by assuming that the E_{ch} and $f(d_p)$ are constant in the same size interval, Equation (2.8) is simplified to:

$$I_i = E_{ch,i} C_i, \tag{2.9}$$

where $E_{ch,i}$ is the charging efficiency at $\sqrt{d_{50,i} \cdot d_{50,i+1}}$ and C_i the particle concentration in the size interval $d_{50,i} - d_{50,i+1}$. In the nominal measurement range of i:th stage, particle concentration can now be calculated by dividing the measured current with the charging efficiency at the center of the measurement channel. This is called the cutpoint concept (Cooper and Guttrich, 1981) applied to an ELPI case (Keskinen et al., 1992). It gives a number of size distribution values similar to that of measured currents. For many purposes, this is enough with the added advantage that is a straightforward and fast to use. Fine particles have significant secondary particle losses to the upper stages in ELPI. This induces an error that can be corrected in some extent with the fine particle correction algorithm by Moisio et al. (1999). Algorithm transfers a current from the large cutpoint stages to low cutpoint stages. In addition to fine particle losses, overlapping kernels introduce an error in cutpoint concept calculation, as shown by Marjamäki (2003).

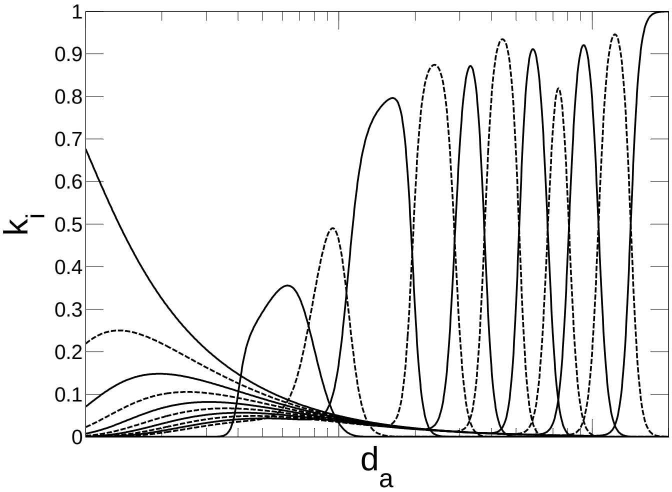

Figure 2.4: Example of impactor kernels.

Chapter 3

Methodology

3.1 Experimental methods

3.1.1 Calibration of components

All impactors in **Papers 2** and **3** and the pressure reduction inlet of the HRLPI were calibrated using electrical detection of particles. Components under calibration were electrically insulated from the instrument housing, and electrometers were used to measure the charge carried by the particles to different components. Component losses or collection efficiencies could be determined from the currents. An electrical calibration method for a single impactor stage was introduced by Hillamo and Kauppinen (1991). Keskinen et al. (1999) showed that electrical calibration can be applied to calibrating a cascade impactor with a multi-channel electrometer. The advantage of the method is good sensitivity to nanoparticle calibration and real-time detection.

For nanoparticles generation of charged monodisperse aerosol is rather straightforward . The evaporation-condensation type (Liu and Lee, 1975) generator (ECG) produces lognormal dioctylsebacte (DOS) aerosol. After the ECG, a radioactive neutralizer and a differential mobility analyzer (DMA, Knutson and Whitby (1975)) in series produce singly charged monodisperse particles. Roughly, above 50 nm, a DMA cannot be used to produce monodisperse particles because of doubly charged larger particles that pass into the DMA sample flow. This passage can be partly avoided by choosing particles from the falling edge of the right-hand side of the size distribution . The problem of multiply charged particles for particles above 50 nm was avoided by using the Singly Charged Aerosol Reference (SCAR, Yli-Ojanperä et al. (2010)). In the SCAR, first singly charged seed particles are produced with the combination of an ECG and a DMA. After this, DOS vapor is condensed onto pre-charged seed particles. After condensation, a second DMA can then be used to classify truly singly charged large particles.

Inlet and charger of HRLPI

The HRLPI operates in highly reduced pressure conditions, and a separate pressure reduction inlet is used to bring the pressure down to the inlet pressure of the impactor. Inlets tested with the HRLPI were calibrated using a reference faraday cup electrometer (FCE). The inlets were assembled to the impactor part as in a normal measurement configuration. The reference FCE measured the concentration of the particles before the impactor, and the concentration after the inlet was measured by the impactor. The penetration of the inlet was calculated from measured currents with the following equations:

$$P_{inlet} = \frac{I_{impactor}}{I_{fce}} \tag{3.1}$$

$$I_{impactor} = \sum_{i=0}^{n} I_i, \tag{3.2}$$

where the n is the number of impactor stages and $i = 0$ is the filter stage. All particles were generated with SCAR.

The charger was calibrated using DOS, NaCl, and silver particles generated with ECG techniques. Monodispersity was accomplished with a DMA after the particle generators. DOS calibrations were done according to the method described in (Marjamäki et al., 2000), whereas the method used for NaCl and Ag calibrations can be found in Marquard et al. (2006).

Impactor

The impactor was calibrated using DOS particles. Particle sizes of up to 30 nm were produced with the ECG. Particle sizes above 30 nanometer were produced using the SCAR instrument. The lowest particle sizes were produced with the ECG generator because the particles produced with the SCAR included a ten-nanometer NaCl nucleus. Because NaCl is of higher density than pure DOS, particle density would have been difficult to control. After generation, particles were classified for size using a TSI's 3071 DMA, which was coupled to the impactor inlet. The impactor was fitted in the ELPI impactor body, and calibration was done according to the electrical calibration method described earlier. The collection efficiency of each stage was calculated from measured stage currents with the following equation:

$$E_i = \frac{I_i}{\sum_{k=0}^{i} I_k}, \tag{3.3}$$

where I_i is the current measured from the i:th stage. In stage numbering, the filter stage corresponds to the index i=0, and the lowest cutpoint stage corresponds to i=1, and the second lowest stage i=2, and so on. The SCAR produced truly singly charged particles, and no multiple charge correction was needed.

3.1.2 Measurement setups to determine critical velocity

In **Paper 3**, the critical velocities of a rebound of 20 nm – 1000 nm spherical silver particles were determined. A variable nozzle area impactor was used to increase the impaction velocity of particles by changing the jet velocity by decreasing the slit length of the nozzle. The slit length value at which particle bounce is initiated is called the critical slit length.

Particle sizes 20 – 200nm

Figure 3.1(a) shows schematically the measurement setup for spherical and monodisperse silver nanoparticles used in **Paper 3** for the size range of 20–200 nm. Particles were generated by an evaporation condensation method, followed by sintering and size selection (Harra et al., 2012; Scheibel and Porstendörfer, 1983). Silver particles formed in dilution after the first furnace, and a subsequent coagulation chamber was used to increase the particle size before the sintering step. To sinter relatively large particles (∼100 nm), two successive furnaces were used. After sintering, a monodisperse mobility particle size distribution was realized with a Vienna-type DMA. Because nitrogen gas used in the sheath flow and as carrier gas in the previous steps, the final sample was extremely dry (RH$<1\,\%$).

Loading of the collection substrate can be avoided by keeping the particle concentration low. A bridge dilution system was used before the impactor to reduce the concentration. When an electrical particle detection is utilized sensitivity can be increased by increasing the charging level of particles. This was achieved by adding a small corona charger after the dilution. The maximum particle area fraction on the impactor plate during measurements was estimated to be approximately 5%. The VNAI and the following filter stage were connected to ELPI electrometers and a vacuum pump, and pressures were measured before and after the impactor. Furthermore, a critical orifice inlet assured a constant volumetric flow rate (1.18 lpm). In addition to electrical collection efficiency measurement, particles were analyzed with a transmission electron microscope (TEM).

Particle sizes 400 – 1000nm

Figure 3.1(b) shows the generation and measurement setup for silver particles in the size range of 400 – 1000 nm. Commercial silver powder was dispersed in water and sprayed with an atomizer aerosol generator. In order to prevent sedimentation, the dispersion was ultrasonificated and stirred with a magnetic mixer before and

(a) Setup for 20 - 200 nm particles.

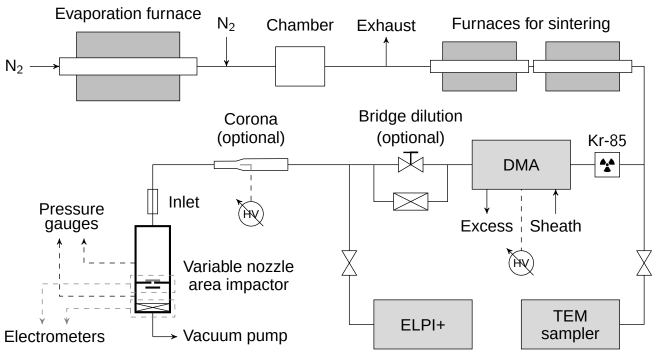

(b) Setup for 400 - 1000 nm particles

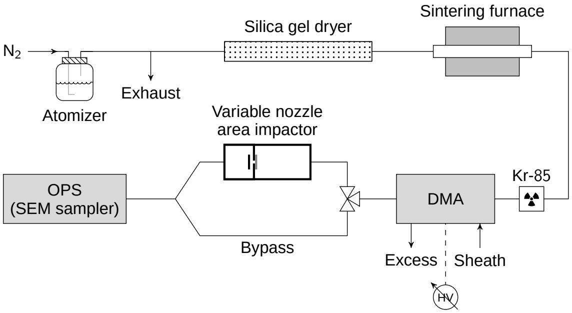

Figure 3.1: Different measurement setups for electrical and optical detection of collection efficiency (**Paper 3**).

during the spraying process, respectively. The aerosol was dried with a silica gel dryer and sintered in a furnace. Particle size selection was carried out with a Vienna-type DMA which was followed by the variable nozzle area impactor. Here the impactor pressure and the flow rate was 960 mbar and 1.0 lpm, respectively. After the DMA aerosol includes also doubly and triply charged particles, electrical detection was not feasible to measure collection efficiency. Instead, an optical particle sizer (OPS, TSI 3330) was used as a particle counter to distinguish the multiply charged particles. A reference particle concentration was measured by bypassing the impactor. Particle samples were analyzed also with a scanning electron microscope (SEM).

3.1.3 Test measurements of the HRLPI

In **Paper 4**, the HRLPI was devised and tested for performance and compared in laboratory measurements with five commercial instruments (for instruments, corresponding abbreviations, measurement size ranges, and flow rates, see Table 3.1). Size ranges were in mobility or aerodynamic diameters, depending on the classification method of the corresponding instrument. HRLPI, EELPI, and ELPI+ particle size distributions were calculated using the cutpoint concept (Kauppinen et al., 1986; Keskinen et al., 1992). Fine particle losses were corrected as presented by Moisio et al. (1999), and the penetration of the inlet was included in the size distribution calculation. EEPS and SMPSs results were exported using the measurement software export. Figure 3.2 shows the setup for laboratory measurements. The sample flow was diluted after the HRLPI to have similar current signal levels for the HRLPI, EELPI, and ELPI+. The EELPI was used without a trap voltage, and the ELPI+ was used at the default factory settings, which included trap voltage (20 V). The electrometer zero levels were subtracted from the measured signals. Charger ions collected by the few highest cutpoint stages in the EELPI and the measurement artefact introduced by the ions were compensated by zero level correction. The dilution ratio and the sampling line losses were also corrected from measured size distributions.

Manufacturer/Instrument	Abbreviation	Measurement range (nm)	Flow Rates (lpm)
TSI/Nano SMPS	NanoSMPS	2-65	Sample 1.5, Sheat 15
TSI/Long SMPS	LongSMPS	10-245	Sample 1.5, Sheat 15
TSI/Engine Exhaust Particle Sizer	EEPS	5.6-560	10
Dekati/Classic ELPI	EELPI	6-10,000	10
Dekati/ELPI+	ELPI+	6-10,000	10
-/HRLPI	HRLPI	3-200	1

Table 3.1: List of instruments in the laboratory measurements. TSI's 3025 Ultrafine CPCs were used in the NanoSMPS and LSMPS configurations.

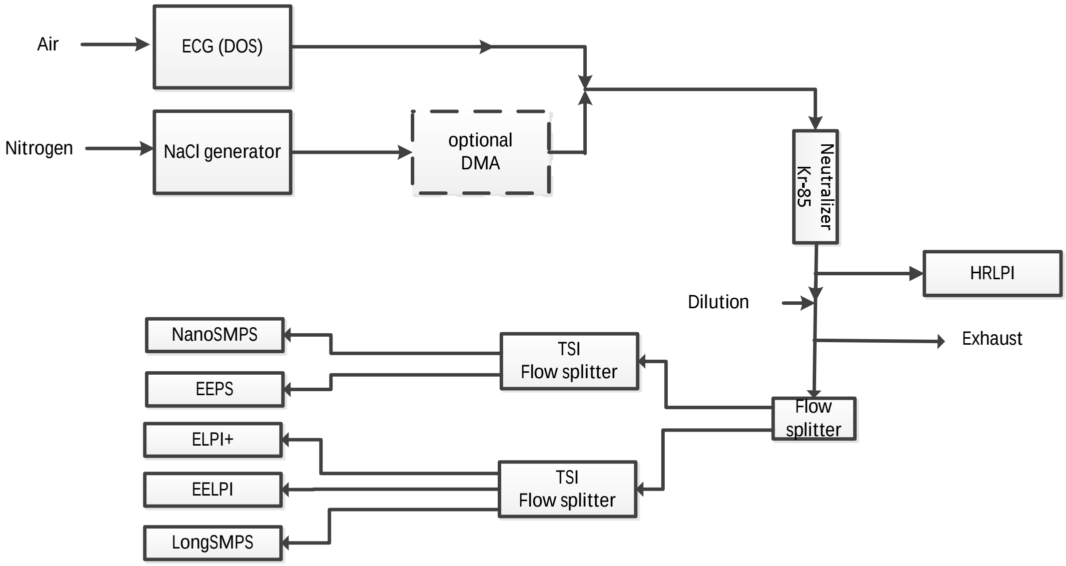

Figure 3.2: Setup for HRLPI laboratory test measurements (**Paper 4**).

3.2 Numerical methods

3.2.1 Modeling impactors

In **Papers 1-4**, the impactors were numerically simulated to study their collection efficiencies and particle impaction velocities. The core of the model was to numerically solve the Navier-Stokes equations (NSE) that describe the flow field inside the impactor. The second part of the problem was to solve particle tracks in a simulated flow field and to calculate from the track data the collection efficiency of the LPI. An integral part of solving the NSE was also to set correct boundary conditions for the problem. In principle, every researcher could code their own solver for the NSE, but the non-linear terms in NSE equations are the origin of turbulence, which complicates the solution. Fortunately, complex fluid dynamics problems are so ubiquitous in industry as to have contributed to the ready availability of commercial computational fluid dynamics (CFD) solvers.

Flow field

The flow field inside the impactor nozzles was simulated by solving the Favre averaged (density-weighted time averaging) NSE by employing the CFD package of Fluent 6 (**Paper 1**) and ANSYS Fluent 14.0 (**Papers 3** and **4**). The Favre averaged versions of the NSE equations must be used when the flow is compressible as it is in the case of a low pressure impactor. Time averaging the original NSE equations produces extra correlation terms in the original equations, and a so-called turbulence model is needed to close the equation system. The turbulence model used in this study was the SST-$k-\omega$-model (Menter, 1994), which consists of two convection diffusion type partial differential equations for the turbulence parameters k and ω. The k parameter is the turbulence kinetic energy, which describes the intensity of turbulent velocity fluctuations, and ω is the specific dissipation rate of turbulence kinetic energy. The turbulence transfer equations are coupled via turbulent viscosity to the NSE equations, and all equations are solved simultaneously. SST-$k-\omega$-model was chosen because it has been reported to be not very sensitive to the inflow boundary values of turbulence quantities (Menter, 1994). The flow field was solved numerically all the way down to the viscosity-affected laminar sublayer at the solid surfaces by adapting computation grids near the walls. Symmetry boundary conditions were used in simulations to help to reduce the computational burden, though they also limited the investigation to a single nozzle from each stage. Consequently, the effects related to the interaction between adjacent jets at multi-nozzle impactor stages could not be seen in the modeling results.

With LPI simulations, the set of feasible boundary conditions is, for example, the mass flow rate at the flow inlet, symmetry plane or axis, zero flow velocity and particle capture at the walls, and outflow stagnation pressure. Also inflow boundary conditions had to be set for turbulence quantities, and they were estimated according to the recommendations in the software manual. Values for the k and ω parameters were defined by setting a value for turbulence intensity and length scale. The intensity was estimated based on directions given in the ANSYS Fluent manual to be low at 1 % and the length scale at 0.1 mm. The software internally takes care of the turbulence quantities at the solid walls. There was no need for a systematic study on the sensitivity of the solutions to inflow turbulence boundary conditions as the turbulent viscosity decayed fastly after the infow. The only region where the turbulence increases significantly is where the impactor jet impinges to the substrate. The turbulence is locally generated within this shear layer; there is practically no convection of turbulence from the upstream side.

To ensure that the computation grid was dense enough, results were calculated using denser and denser grids and by choosing the grid after which the results did not change anymore. The number of control volumes in the grids varied between $5 \cdot 10^4$ to 10^5. The convergence of the results was confirmed by following the development of the residuals and the flow field variables during the iterative solution procedure. Calculation was terminated when the average values of velocity, pressure, and turbulent viscosity changed no longer at the surface of the collection plate.

When the ratio of the downstream to upstream pressure of the impactor nozzle is reduced to the order of 0.5, the flow is considered to be choked. Although a straight nozzle geometry was used in the studied LPI nozzles, the shape of the flow field may have resembled that of a Laval-nozzle. In the Laval-nozzle, the flow velocity accelerates beyond one Mach because of the divergent cone. When a transonic or supersonic flow impacts on a body or a wall, shockwaves may form, and their effect on impactor operation must be considered. The SST-$k-\omega$-model is capable of predicting the formation of shock waves at least roughly, as pointed out by Bartosiewicz et al. (2005). The minimum pressure ratio in the study was approximately 0.4, which means that the flow velocity after the nozzle could have been over one Mach, and that effects related to shock waves could have been possible.

Particle tracks

Particle trajectories were calculated after the flow field had been solved. Therefore, it is a one-way coupling between the flow field and particles. This should be a valid assumption, as the particle mass flow rate is negligible compared to gas flow rate through an LPI nozzle.

The collection efficiency of the impactor can be calculated from the particle track data when traces of different sized particles have been calculated. Particles entered the nozzle from the flow inlet and were followed until they were impacted to the collection plate or survived to the outlet. It was thought that each particle represents a particle stream from a certain surface area. If the particle impacted, the particle stream that it represents was collected from the flow. If particle passed the corresponding particle stream passed too. From the particle starting location and penetration data the stage collection efficiency E as a function of the aerodynamic size of the particle can be calculated:

$$E(d_p) = \frac{\sum_i v_{g,i} A_i L_i}{\sum_i v_{g,i} A_i}, \tag{3.4}$$

where A_i is the area of the nozzle represented by the i:th particle, v_i the particle velocity normal to the nozzle inlet cross section, L_i is zero if the i:th particle was collected or one if it survived through the stage. The trajectories were calculated in the time averaged flow field and no stochastic tracking model was used. Stochastic models were not used because there is some evidence that they might not be accurate with mildly turbulent flows. This can be seen from the article by Leduc et al. (2006) who tried to model the cutpoints of the ELPI impactor using the stochastic tracking options of the Fluent 6 software but failed.

Impaction velocity simulation

To vary particle impaction velocity in the impactor, one can for instance (as predicted by Equation (2.2)), change the jet velocity by changing the nozzle area. This method was utilized in **Paper 3**, where the nozzle area is varied by changing the slit length with an adjustable cover. Firstly, the flow fields corresponding to different slith lengths were simulated. The second step is to simulate the impaction velocities and collection efficiencies as a function of slit length for different particle sizes. Figure 3.3 shows an example of the simulated collection efficiency and particle impaction velocities (normal component of velocity) in the variable nozzle area impactor. For the slit length values roughly above 5 mm the impaction velocity is almost linearly dependent on L. The flow becomes choked when the slit opening is less than 5 mm, and the impaction velocity rises steeply towards decreasing L-values.

3.2.2 Inversion

The inversion of ELPI current distribution to a number size distribution has been investigated by Lemmetty et al. (2005). In their inversion, Equation (2.8) is discretized into a matrix form, and the size distribution $f(d_p)$ is solved with a numerical method appropriate for the ill-posed problem (see, e.g. Hansen (1998)).

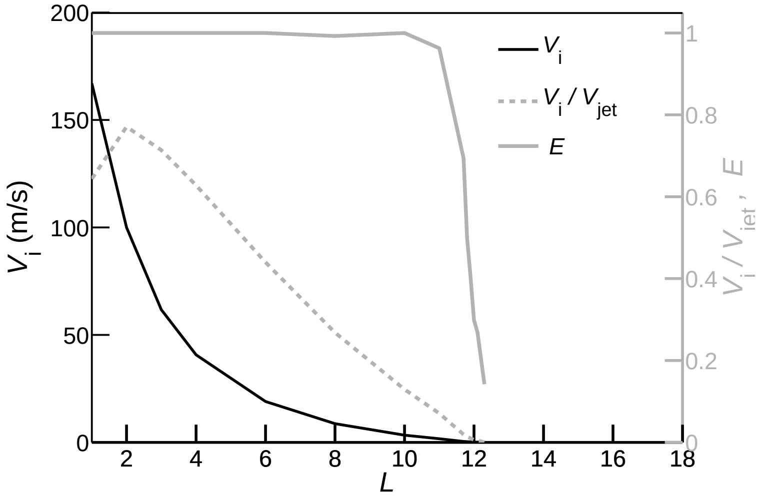

Figure 3.3: An example of obtained particle impaction velocities in the variable nozzle area impactor for 777 nm particles (aerodynamic diameter). On the horizontal axis is the slit length (L) that is directly proportional to the nozzle area. E is the collection efficiency, V_{i} the impaction velocity and $V_{\mathrm{i}}/V_{\mathrm{jet}}$ is the impaction velocity normalized by the average jet velocity. The flow rate is 1.18 l min^{-1} and the inlet pressure 250 mbar.

The ELPI inversion problem in a discretized form is:

$$\mathbf{I} = \mathbf{K}\mathbf{f} + \epsilon, \tag{3.5}$$

where $\mathbf{K}$ is the kernel matrix, $\mathbf{f}$ the size distribution vector, and ϵ the current measurement error vector. This is a linear problem and in principle could be solved numerically finding the pseudoinverse of kernel matrix. However, this leads to an unstable and oscillating solution as there is no unambiguos solution to Equation (3.5). The simplest inversion that utilizes the shape of impactor kernel functions and smoothness of the size distribution is the Tikhonov regularization. In the Tikhonov regularization the smoothed solution is obtained by solving (Hansen, 1998):

$$\mathbf{f_{reg}} = \arg\min_{\mathbf{x}} \left\{ \|\mathbf{Kx} - \mathbf{I}\|^2 + \lambda \|\mathbf{Lx}\| \right\}, \tag{3.6}$$

where $\mathbf{f_{reg}}$ is the regulated solution, $\mathbf{x}$ the varied unknown size distribution, λ the regularization parameter, and $\mathbf{L}$ typically the second derivative of $\mathbf{f}$ in aerosol applications. The regulated solution is a compromise that fits to the measured currents in the least squares sense and full fills the smoothness criterion. The solution to the problem (3.6) can be written:

$$\mathbf{f_{reg}} = \left(\mathbf{K^T K} + \lambda \mathbf{L^T L}\right)^{-1} \mathbf{K^T I} \tag{3.7}$$

The inverse matrix in the equation has a unique solution, and thus, for example, Matlab's pseudoinverse can be used to compute it. The regularization parameter determines the smoothness of the solution. Different methods have been developed to find optimal λ value for the problem (Hansen, 1998). In this work a constant value was used instead of algorithmic adjustment, and it was found to perform reasonably well with HRLPI inversion.

Chapter 4

Results

4.1 Flow field and collection efficiency

In **Paper 1** the CFD model of an impactor was developed and validated by simulating the cut-curves of ELPI impactor. The limits of the simulation method were outlined and the model was then used to study the effect of collection plate distance on the collection efficiency curve steepness. Figure 4.1 shows the simulated velocity, pressure and temperature contours in the 30 nm cutpoint stage of ELPI+. In the left pane is the velocity. It shows that the maximum velocity in the axis of the jet is approximately 1.17 Mach. The area weighted average velocity at the jet outlet is approximately $280\,\mathrm{m\,s^{-1}}$, which corresponds to the average velocity calculated by assuming an adiabatic flow through the nozzle which is $285\,\mathrm{m\,s^{-1}}$. The jet decelerates and turns rapidly near the collection plate, much closer than one jet radius. This is an interesting observation compared to conventional impactor theory (see, for example Hinds (1998)). In the conventional theory, the flow is assumed to be incompressible and to perform the turn around the collection plate approximately within the one jet radius. Thus, it seems obvious that for high Reynolds number and compressible flow the conventional theory should be modified in order to get accurate results without experimental calibration of the critical Stokes number.

The middle pane of Figure 4.1 presents the static pressure contours. It shows that the pressure in the jet axis in the vicinity of the collection plate is very close to the upstream stagnation pressure before the nozzle. This reproduces the experimental observation presented by Flagan (1982) and Kauppinen et al. (1986). What the experimental results do not reveal, is that the static pressure varies significantly across the jet area near the collection plate. It was found in the simulations that the impaction of the particles did not start from the jet axis advancing toward the outer edge of the jet as the particle size was increased.

Instead the impaction first took place closer to the outer edge of the jet than in the axis. As the particle size was increased it advanced toward the jet axis and the outer edge. This impaction order is linked to the pressure profile and slip correction factor. Slip correction for nanoparticles is highly dependent on pressure, that was seen to vary within the the jet radius near the collection plate.

Simulated temperature contours are shown in the rigth pane of Figure 4.1. Adiabatic expansiong takes place in the nozzle and temperature is reduced far below free freezing point of water. In this case, the temperature drops at the nozzle outlet to −38 °C. For these conditions, it is possible that some particles can undergo a phase transformation.

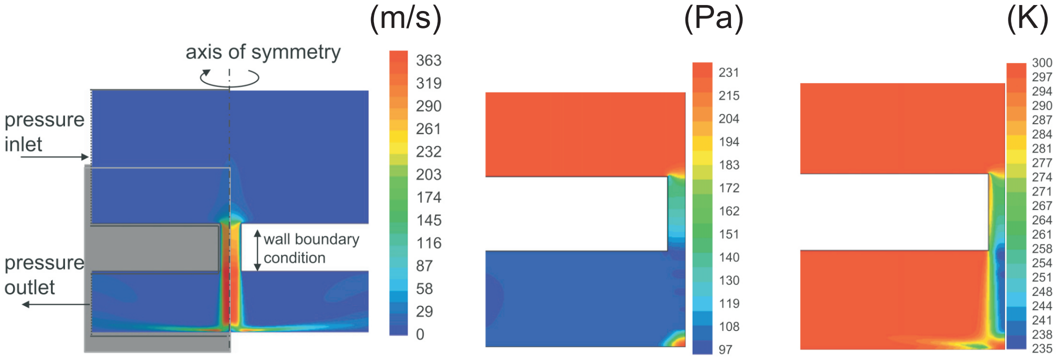

Figure 4.1: Velocity, pressure and temperature contours at the cross section of ELPI impactor nozzle (stage 1). (**Paper 3**)

Figure 4.2(a) presents simulated and measured collection efficiencies of ELPI impactor (Marjamäki et al., 2000). Simulated cutpoints are in-line with the experiments, but only a few of the simulated steepnesses match with the experiments. This was analysed in the **Paper 1**. Figure 4.2(b) shows the ratio of simulated and experimental steepnesses for ELPI stages and the turbulence level. When turbulence level increases the deviation between the simulated and measured steepnesses increases. The model does not include the stochastic effets of turbulence on particle tracks, and it seems that turbulence reduces the collection efficiency steepnesses in some of the ELPI impactor stages.

Figure 4.3(a) shows the simulated effect of jet-to-plate distance on LPI resolution, or collection efficiency curve steepness (ELPI stage 1). Larger value means higher steepness of collection efficiency curve. Resolution shows peak at $S/W = 2$. This is expained by Figures 4.3(b) and 4.3(c). Figure 4.3(b) presents the impaction parameter (I_{ip}) as a function of radial distance from the jet axis.

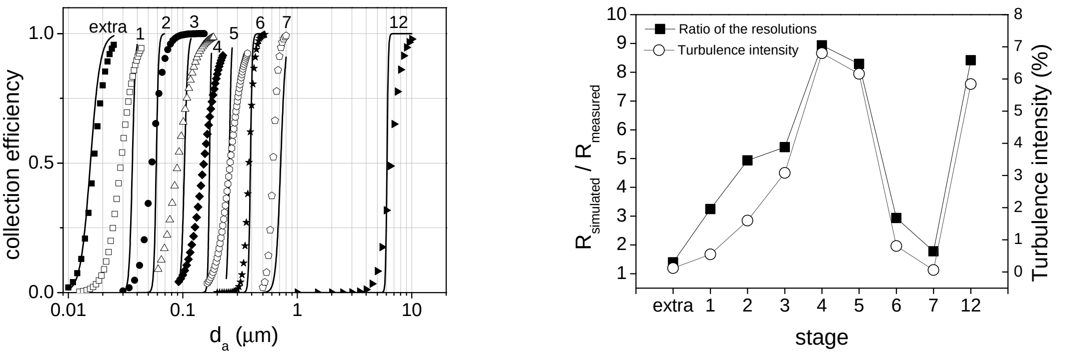

(a) collection efficiency

(b) turbulence effect

Figure 4.2: (a) Simulated and measured ELPI impactor collection efficiencies. (b) Effect of turbulence on simulation quality. (**Paper 1**)

I_{ip} is defined in a following way:

$$I_{\mathrm{ip}} = \frac{V_0}{P_{\mathrm{ip}} S_{\mathrm{ip}}} \tag{4.1}$$

Here V_0 is the velocity of the particle before the flow turns, P_{ip} is the pressure approximately 20 µm above the collection plate, and S_{ip} is the distance from the collection plate when the axial flow velocity has dropped to zero. For low-pressure impaction, the impaction parameter is in principle a simplified Stokes number. A high I_{ip} value means conditions more favourable for impaction. The most uniform impaction conditions seem to occur at $S/W = 2$, which is quantitatively shown in Figure 4.3(c) with impaction parameter distributions for three jet-to-plate distances. At $S/W = 2$, most of the particle flux undergoes similar impaction conditions with the resolution then at its maximum.

If the size distribution is known a priori to have a specific shape, a single impactor stage with some type collection efficiency detection can be used to estimate the average particle size. If the impactor's collection effciency increases in a wide range of particle size, instead of rising sharply, the range of the instrument's operation is maximized. Such an impactor stage was designed for an instrument called the DENSMO (Juuti et al., 2015), which measures the effective density of particles by determining their average mobility and aerodynamic size. Decay of resolution with an increasing jet-to-plate distance was exploited in the design of the DENSMO LPI stage, and low-gradient collection efficiency was realized by increasing the S/W-ratio to 10 and by using a porous collection substrate. In the DENSMO, the LPI stage is connected in series to a filter stage, and the collection efficiency of the impactor stage is determined by electrical detection of particles from the impactor and the filter stages. The DENSMO was developed in BUONAPART-E, an EU project conceived to monitor nanoparticle production facilities.

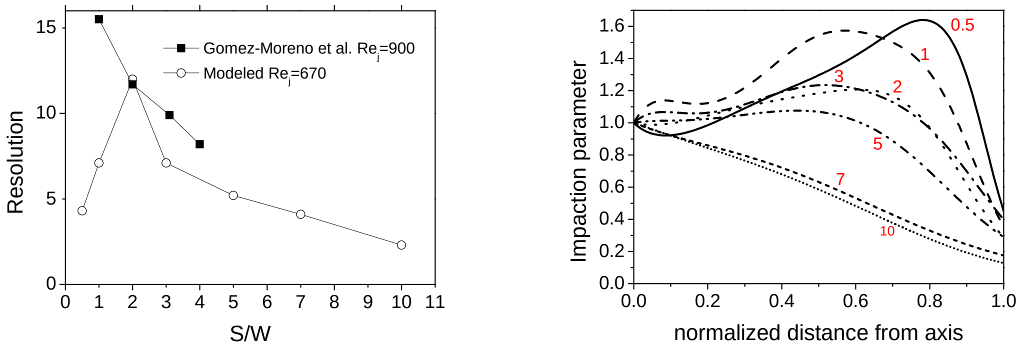
(a) resolution vs. jet-to-plate

(b) impaction conditions

(c) impaction parameter

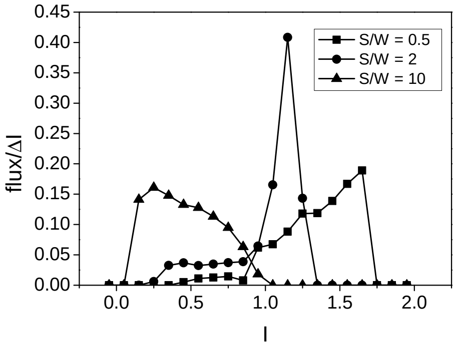

Figure 4.3: Simulated effect of different parameters on LPI operation (adapted from **Paper 1**). (a) Jet-to-plate distance (b) Impaction conditions in the nozzle cross section (c) Impaction parameter distribution.

4.2 Effect of nozzle throat length and geometry on resolution

The effect of the nozzle geometry on the steepness of the LPI stage collection efficiency curve was studied in **Paper 2** experimentally and with the CFD model developed in **Paper 1**. Changes in the nozzle velocity profile were linked to changes in the steepness of the collection efficiency curve and particle impaction velocities. Figure 4.4(a) presents simulated axial velocity profiles at the nozzle exit plane for the slit nozzle LPI stage. The velocity profiles are plotted across the nozzle with the nozzle's center at the origin. The profile shows that the flow profile is very close to plug flow when the length of the nozzle throat is small compared to the width. This means that if particles follow the flow velocity in the nozzle, they gain nearly uniform velocities before the flow decelerates. Therefore, a uniform velocity profile leads to uniform impaction conditions in the jet and thus increases the resolution. An increased resolution with a short throat nozzle is shown in Figure 4.4(b). Both experimental and simulated collection efficiencies behave similarly in terms of nozzle throat length, although measured curves are a little steeper compared to simulated curves. The reason for this deviation is not clear so far. Figure 4.4(c) shows normal impaction velocity profiles for different particle sizes for the short throat, slit nozzle impactor ($T = 0.1\,\mathrm{mm}$). The velocities are rather uniform except close to nozzle walls, where the flow velocity is zero. This result shows that a steep collection efficiency curve impactor provides also uniform impaction velocities. **Paper 3** exploited this result and exploited a short throat slit impactor to study the critical velocity of the rebound. Table 4.1 shows simulated and measured collection efficiency curve steepnesses for different nozzle lengths and geometries. According to experiments, a short throat nozzle offers higher resolution than a longer one and a slit nozzle better than a round one. A short throat slit nozzle has the highest resolution as the velocity profile is uniform after a short nozzle and compared to a round nozzle a smaller portion of particles pass through the edges of the jet. At the edges the impaction conditions are non-uniform because of boundary layer development.

An underdeveloped jet velocity profile was speculated already by Marple et al. (1974); Marple (1970) to have an enhancing effect on the steepness of the collection efficiency curve. Marple studied the underdeveloped jet effect in terms of the jet Reynolds number. Increasing Re leaves less time for a boundary layer to develop in the nozzle, and the velocity profile is uniform at the nozzle exit plane. This study shows that an effect similar to that achieved by increasing Re can also be effected by reducing the length of the nozzle throat. This result also revises the conventional design recommendation of the impactor, that a nozzle throat long compared to its width should be used to ensure particle acceleration in the jet.

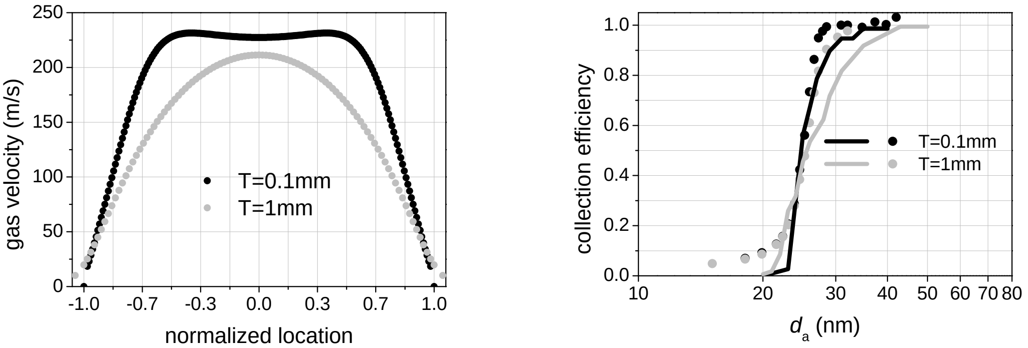

(a) jet velocity profile (b) collection efficiency

(c) impaction velocity profile

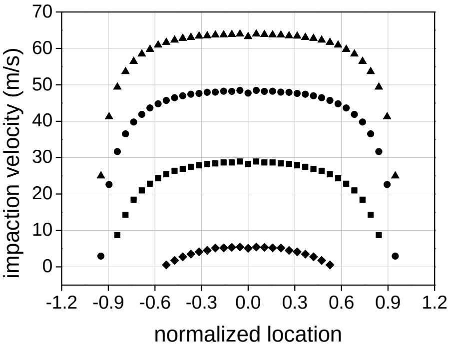

Figure 4.4: Effect of nozzle throat length (T) on impactor nozzle velocity profile and collection efficiency (a and b). Dots represent measurements and lines simulation results in the (b). Impaction velocity profiles for different size particles in the slit type nozzle ($T = 0.1\,\mathrm{mm}$) are presented in (c). (adapted from **Paper 2**)

4.3 Determination of the critical velocity of rebound

The lack of knowledge on the fundamental bounce properties of ultrafine particles limits the reliability of impactor measurement and particle bounce based research methods, as discussed in the introduction. One of the fundamental properties is the critical velocity of rebound that has been investigated in the micrometer size range in several publications. A good review on these is by Wall et al. (1990). In the sub-micron size range only nano size NaCl and spherical Ag particle critical velocities have been investigated (Rennecke and Weber, 2013). Thus, there is a

		Resolution	(dp_{80}/dp_{20})	
Nozzle	T (mm)	Simulated	Measured	Difference (%)
Round	1	1.39	1.28	8.6
Round	0.1	1.14	1.16	-1.7
Slit	1	1.33	1.19	11.7
Slit	0.1	1.17	1.15	1.7

Table 4.1: Simulated and measured resolutions of the stages. Resolution is defined as ratio the ratio of the particle sizes corresponding to 80% and 20% collection efficiencies.

gap in the interesting size range of 100 nm – 1000 nm.

The properties of the slit type impactor presented in **Paper 2** make it an ideal tool to study nanoparticle properties in collisions with a surface. In these studies, precise control of particle impaction velocity is of vital importance because it determines the impaction energy of a particle. **Paper 3** introduces the variable nozzle area impactor (VNAI) that was used to determine the critical velocity of the rebound for spherical silver particles.

4.3.1 Variable nozzle area impactor

The construction of a variable nozzle area impactor is shown in Figure 4.5. It consists of a nozzle plate, an adjustable cover, and an impaction substrate. The nozzle plate contains a rectangular slit with a width of 0.3 mm and a maximum length of 30 mm. The adjustable cover can be manually slid on top of the nozzle to decrease the slit length down to 3 mm and thus to vary the nozzle area. The impactor stage was made vacuum tight by using O-ring sealings up- and downstream. The opening where the adjustable cover connects to the impactor was machined as tight as possible and further sealed with mould silicon. The nozzle throat in the impactor (also the thickness of the nozzle plate) was 0.1 mm long, and the jet-to-plate distance was 0.1 mm. The impaction substrate was machined aluminium. Measurements were made with both plain and greased (Apiezon vacuum grease) substrates. The grease was to inhibit particle bounce and serve as a reference measurement.

The design of the VNAI impactor is based on a finding in **Paper 2** that a slit type and short throat impactor nozzle generates uniform impaction velocities. It is used in the linear region, that is, when the jet velocity changes linearly with the slit length. The precondition for linear region is that the pressure drop over the nozzle is small.

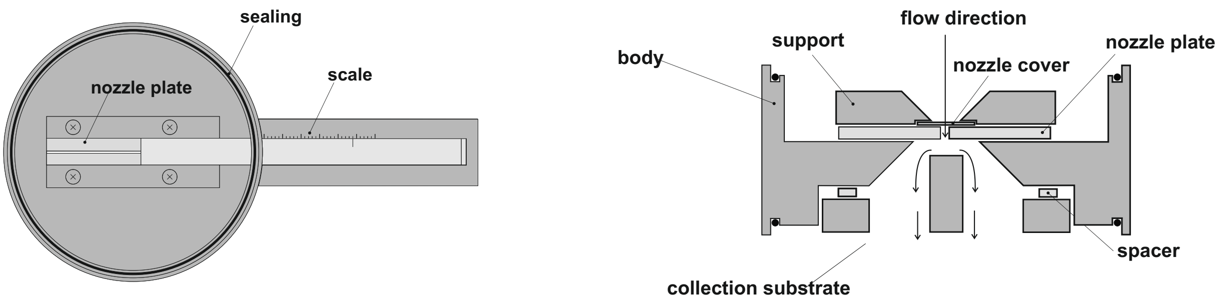
(a) Top

(b) Side

Figure 4.5: Schematic of variable nozzle area impactor.

4.3.2 Detecting the bounce

Figure 4.6 shows two examples of particle collection efficiency curves measured by using a plain and a greased surface in the variable nozzle area impactor. In each case, the measurement procedure started with the slit fully open at 30 mm, and the length of the slit was then gradually shortened by one millimetre intervals down to 3 mm. With long slits, corresponding to slow particle velocities, no particle impaction occurs on the surface. When the slit decreases in length, the particle velocity increases, and particles start to impact. With a greased surface, the collection efficiency reaches 100 % with a sufficiently short slit.

With a plain surface, collection efficiency follows the curve obtained with a greased surface until at short slits it begins to decrease due to particle rebound from the surface. The slit length corresponding to the point where the collection efficiency curves diverge is the critical slit length L_{crit}, which is used to calculate the critical velocity of the rebound. **Paper 3** explains in detail the method to determine the exact critical slit value from noisy data.

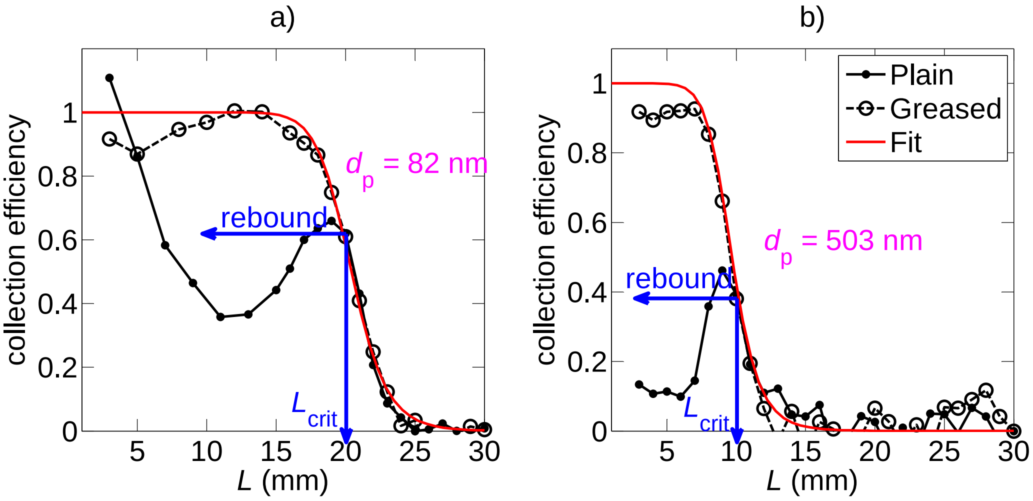

Figure 4.6: The collection efficiency of (a) 82 nm (pressure 156 mbar, flow rate 1.18 lpm) and (b) 503 nm (960 mbar, 1.0 lpm) silver particles as a function of the slit length for a greased and a plane impaction surface (adapted from **Paper 3**). Electrical and optical detection was used for the 82 nm and the 503 nm particles, respectively.

4.3.3 Critical impaction velocities

Once the critical slit length has been measured, the critical impaction velocity is determined by CFD simulation. This is described in detail in **Paper 3**. Figure 4.7 shows the critical velocity of a rebound obtained for spherical silver particles in this thesis and in other studies. The green hatching shows the uncertainty of measurement. Results here and in previous studies show that particle and surface materials greatly affect the critical velocity of the rebound. However, large measurement uncertainties may be involved, for example, in the results of Wall et al. (1990) owing to the fact that if their ammonium fluorescein results were extrapolated down to 20 nm, the critical velocity would be approximately 2000 $\mathrm{m\,s^{-1}}$. However, this is not the case because particles with a crystal structure are known to bounce in a low pressure impactor (for example, Kuuluvainen et al. (2013)), where the impaction velocity at its maximum can be the velocity of sound in air.

The results of Rennecke and Weber (2013) for sodium chloride and silver nanoparticles are 2 – 10 times smaller than those in this study. The difference could be explained by the different particle–surface material pairs they used.

The dependency on the particle size or the exponent value in Equation (2.3) was -1.6, which agrees with most other studies of large particles (over 1 µm). The results of Rennecke and Weber (2013) show a particle size dependency of -3.0, which is quite different. The particle substrate material pair they used was silver–Mica, which may introduce some deviation between the studies. They reported that because their critical velocity values of less than 0.5 $\mathrm{m\,s^{-1}}$ were below the resolution limit of the method they used, a large uncertainty was introduced by the fitting process.

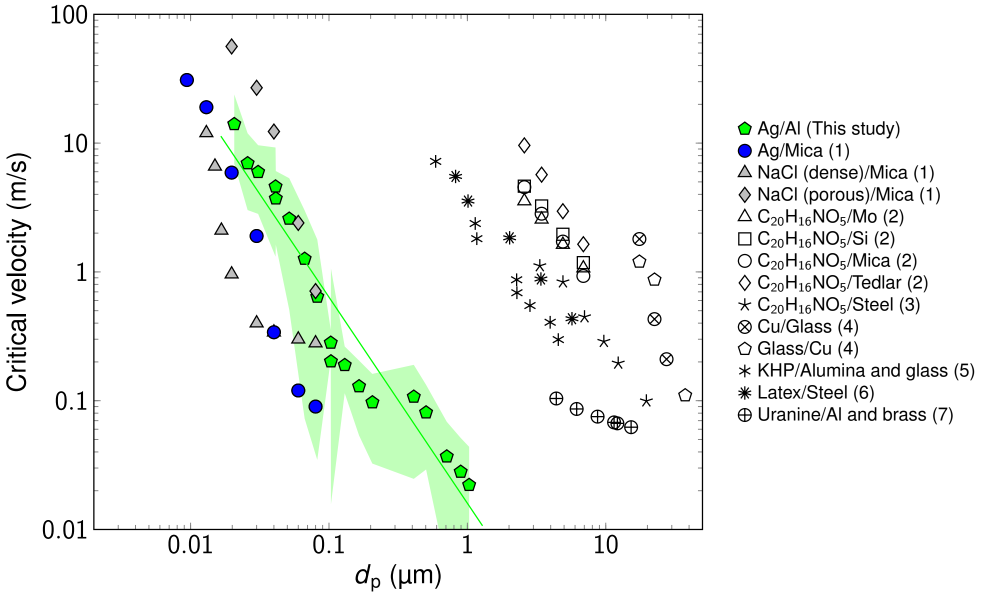

Figure 4.7: The results of this work compared to previous studies (adapted from **Paper 3**) by (1) Rennecke and Weber (2013), (2) Wall et al. (1990), (3) Wang and John (1988), (4) Rogers and Reed (1984), (5) D'Ottavio and Goren (1982), (6) Cheng and Yeh (1979) and (7) Esmen et al. (1978). The legend shows the material of the particle/surface. For spherical particles, the mobility diameter equals the physical particle size. Hatching (green) shows the measurement uncertainty calculated by adding ± 1 mm to measured critical slit values.

4.4 High-resolution low-pressure cascade impactor

An HRLPI cascade impactor was introduced, calibrated, and performance tested in **Paper 4**. This thesis examines theoretically the optimal number of stages and collection efficiency curve shape of a cascade impactor. The essential features of the HRLPI are short throated slit type nozzles (**Paper 2**) and an electrical detection method (Keskinen et al., 1992). Short throated nozzles provide sharp cut-curves, which allow narrow measurement channels without significant overlapping of the kernels. The HRLPI operation pressure is comparably low, only 40 mbar. Because it operates in a high slip correction factor regime, low jet velocities are enough to classify nanoparticles. Consequently, high particle impaction velocities are avoided, and the impactor's particle bounce probability is minimal.

4.4.1 Design of the instrument

Inlet and charger

A separate pressure reduction inlet was used in the HRLPI to reduce atmospheric pressure to the upstream pressure of the highest cutpoint stage. The inlet was constructed from a set of critical orifices and a minor bypass flow after them. An adjustable bypass was needed to fine-tune the upstream pressure, for example, when the ambient pressure changed. A few different inlet configurations were tested experimentally to achieve a high penetration throughout the complete measurement size range.

A small, self-made unipolar corona charger was used with the HRLPI because small size increases the charging efficiency of the smallest detectable particles (<10 nm). The corona current was kept constant (1 µA) by adjusting the charger voltage (2 – 3 kV).

Impactor

The optimal number of stages in a nanoparticle cascade impactor is a balance between practical flow design, particle losses, and particle size resolution. In terms of flow design, the pressure drop over the impaction stages cannot be too large to maintain a reasonable pumping capacity. Reducing the total flow rate reduces the need for pumping capacity, but at the cost of instrument sensitivity. The chosen values of 1.1 L min^{-1} and 8 mbar for HRLPI outlet pressure were considered practical because a pump similar to that in the ELPI was adequate.

Sub-cut particle collection increases exponentially with the stage number. For example, if the penetration through an impactor stage for some particle size is 0.9, the penetration drops to 1/10 when the number of stages is increased from 10 to 30. Therefore, 30 stages would be the definite maximum in a nanoparticle cascade impactor. A possible way to avoid the losses problem would be to use several cascade impactors with different cutpoints in parallel, but considering the benefits that it offers would deserve a study of its own and is beyond the scope of this thesis.

More difficult questions to answer are the optimal number of measurement channels per particle size decade and the optimal steepness of the collection efficiency curve. To answer them, different type inversions of size distribution must be considered. In inversion, all possible information on instrument response and measurement target is used to find out the original size distribution.

The simplest conversion from a current- to number-size distribution is the cutpoint concept. A real instrument must be compared with an ideal cascade impactor. By ideal we mean a cascade impactor with step function shape collection efficiencies. This case was studied by Marjamäki (2003), who showed by instrument simulation that decreasing the steepness of collection efficiency curves increases the measurement error.

The effect of the steepness of the collection efficiency curve on inversion is analyzed in Figure 4.8. Figure 4.8 (a) shows the input size distribution and results of a simulated Tikhonovian inversion for two different collection efficiency steepnesses. From the input size distribution, currents of a 10-stage electrical cascade impactor were simulated using Equation (2.8). Then noise was added to the simulated current distributions (5 % relative noise and 1 fA absolute noise per channel). Inversion was performed for the noise including current distributions (50 distributions for both steepnesses), and Figure 4.8 (a) shows the average of the inverted size distributions. It shows that if the input distribution remains constant, and if the size distribution is measured 50 times and time-averaged, no significant benefit is achieved using steep cut-curve LPI stages. However, it is a different case if we look at the quality of a single measurement inversion with noise. Figure 4.8 (b) shows the standard deviation of noise as a function of particle size in inverted size distributions. The noise level is double with low steepness collection efficiency curves ($s = 4$) compared to steep cut-curves ($s = 10$). This means that in transient measurement, the quality of impactor kernels improves the quality of inversion. Interestingly, the dips in the noise curves correspond to the cutpoints of the stages. The inversion near the cutpoints is more stable because the number of feasible solutions to the inversion problem is most limited at these particle sizes.

Figure 4.9 (a) shows three input size distributions and Figure 4.9 (b) the mean squared error of the inversion as a function of number of stages. The size range remains the same, but it is divided more densely with an increasing number of stages. Also in this case, noise was added to input currents to avoid an inversion crime, that is, using simulated currents directly in inversion. The error in the inversion is minimal around 10 – 13 stages for three size distributions. The exact

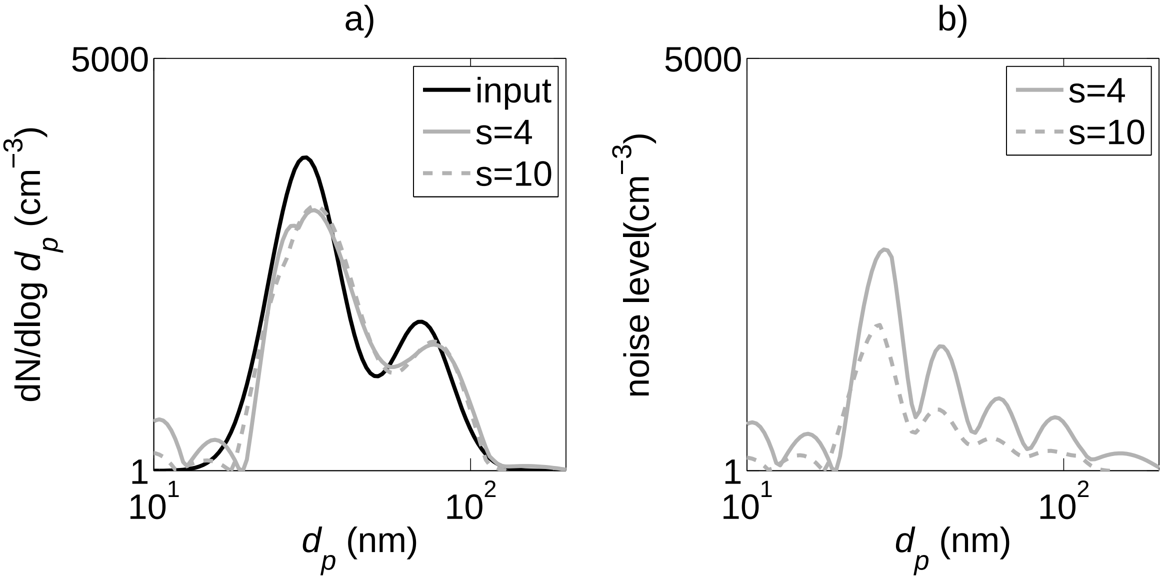

Figure 4.8: a) Results of the Tikhonovian inversion with different collection efficiency curve steepnesses (greater s means steeper cut-curve). b) standard deviation of noise in the inversion for over 50 inverted size distributions.

location of the optimal stage number depends at least on the amount of signal. The total current is the lowest in the case of the dashed line size distribution, which also has the lowest optimal number of stages.

One fundamental issue with impactor measurements is the bounce of particles from the collection substrates. This problem can be minimized by keeping the particle impaction velocity as low as possible. Another way to inhibit bounce is to limit the range of the particle size collected at each stage. Because the HRLPI has narrow measurement channels and relatively low jet velocities, both these criteria are optimized. Figure 4.10 shows the CFD simulated maximum impaction velocity of particles in HRLPI and ELPI impactors and the critical velocity of the rebound for spherical silver particles with plain (**Paper 3**) and greased collection substrates. In the HRLPI, the particle impaction velocity is below the critical velocity even without grease coating. With silver particles, the ELPI uses nearly sonic jet velocities at low cutpoint stages and verges on a bounce even with greased collection substrates. Critical velocity depends on the particle substrate material pair and can be lower for other morphologies and particle materials.

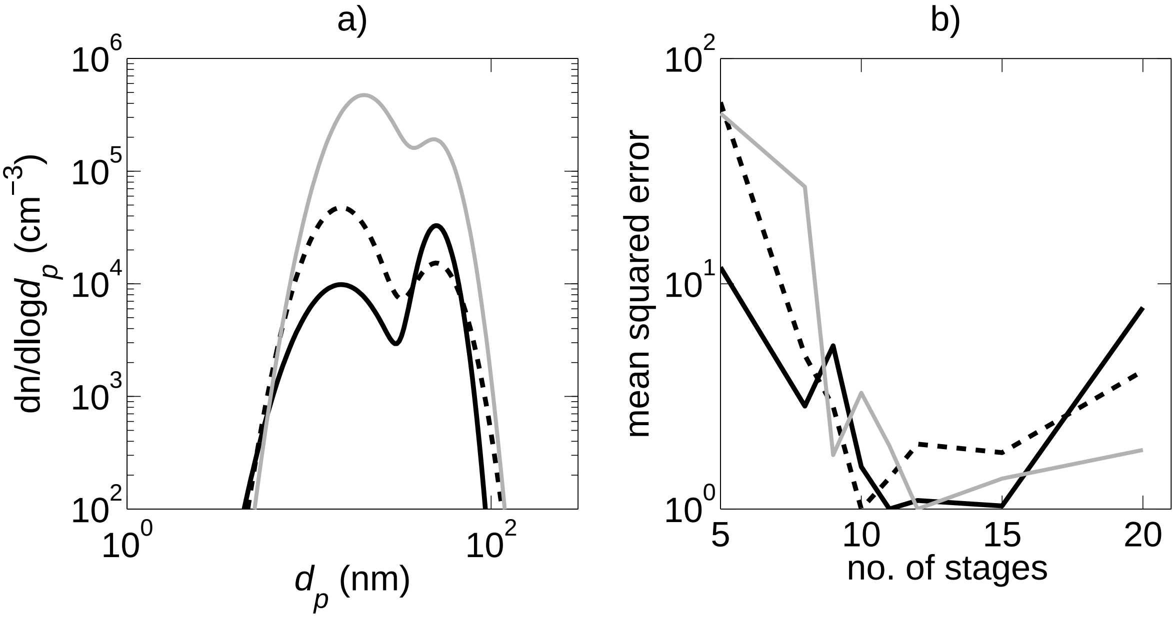

Figure 4.9: The simulated quality of the inversion for three size distributions with different number of stages. a) input size distributions and b) mean squared error.

Table 4.2 lists the critical parameters of the HRLPI impactor. Figure 4.11 shows schematically the components of the HRLPI: the charger, inlet, impactor, and connection to ELPI electrometers. Unlike most conventional impactors, the HRLPI has separate nozzle plates.

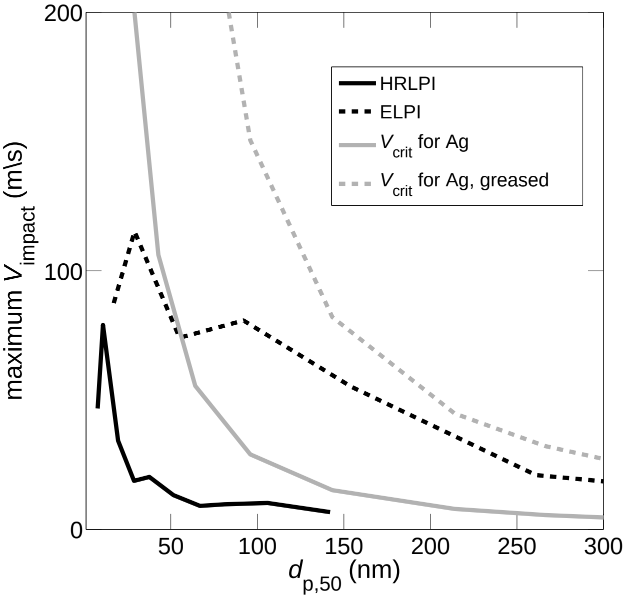

Figure 4.10: Maximum impaction velocity of particles as function of cutpoint of the impactor stage in HRLPI and ELPI and the critical velocity of rebound (V_{crit}) for spherical Ag particles.

stage	L (mm)	W (mm)	T (mm)	S (mm)	T/W	S/W	P_d (mbar)	V_j (m/s)
1	26	0.4	0.1	0.7	0.25	1.75	7.98	238
2	22	0.3	0.1	0.5	0.33	1.66	12.93	216
3	20	0.3	0.1	0.5	0.33	1.66	19.51	152
4	20	0.3	0.1	0.5	0.33	1.66	24.32	119
5	20	0.3	0.1	0.5	0.33	1.66	27.94	111
6	22	0.3	0.1	0.5	0.33	1.66	31.61	87
7	24	0.3	0.1	0.5	0.33	1.66	34.12	78
8	27	0.3	0.1	0.5	0.33	1.66	36.28	62
9	20	0.4	0.1	0.7	0.25	1.75	37.74	60
10	23	0.4	0.1	0.7	0.25	1.75	39.17	45

Table 4.2: Dimensions of the HRLPI stages. L is the length of the slit, W the width of the slit, T the length of the nozzle throat, S the jet-to-plate distance, P_d the downstream pressure of the stage, and V_j the adiabatic jet velocity calculated from measured stage pressures. The inlet pressure of stage 10 is 39.5 mbar.

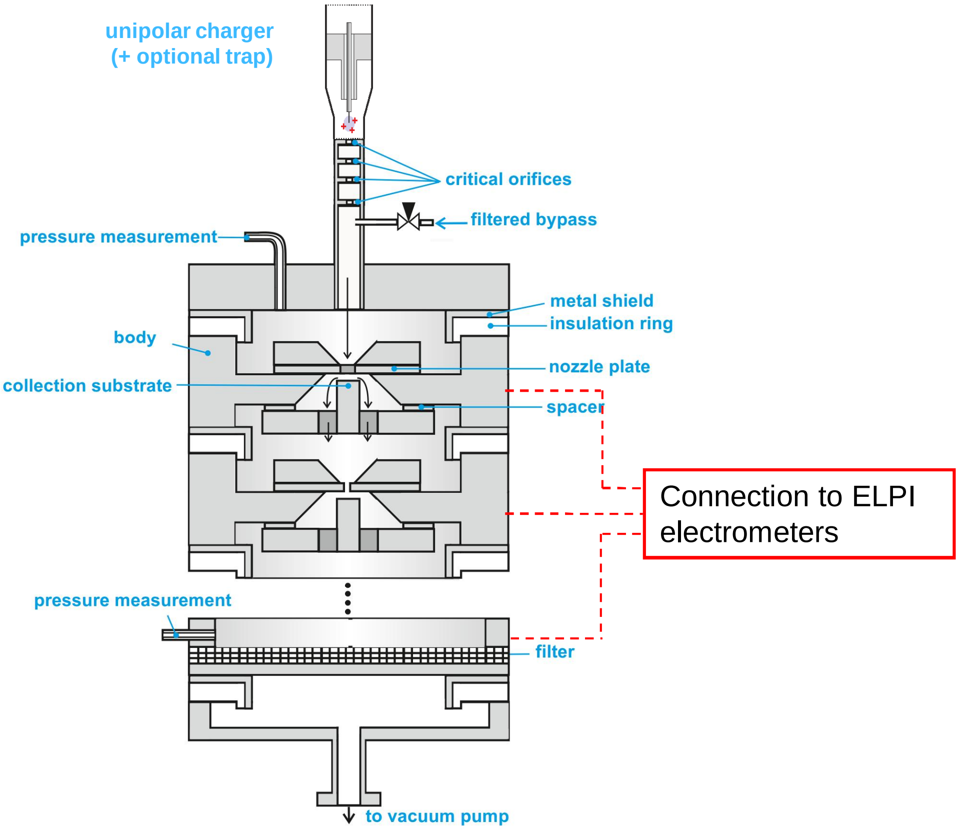

Figure 4.11: Schematic of HRLPI components (adapted from **Paper 4**).

4.4.2 Calibration results

Figure 4.12 a) shows the calibration results of the corona charger. The result is the *Pn*-curve of the charger (penetration multiplied by the average number of charges per particle). Results obtained with different particle materials and calibration methods are consistent with each other. The slope of the logarithm of the *Pn*-curve changes at around 10 nm because the charging efficiency decreases and the losses of charged particles increase. Therefore, two different parameterizations were fitted to the measurement results. The fittings are shown in Equation 4.2.

$$E_{ch} = Pn(d_p) = \begin{cases} 2.811 \cdot 10^5 \cdot d_p^{2.937}, d_p < 0.0092\mu m \\ 111.2 \cdot d_p^{1.267}, d_p > 0.0092\mu m \end{cases} \tag{4.2}$$

Figure 4.12 b) shows the results of the calibration of the inlet and the HRLPI impactor. Crosses represent measured collection efficiencies, plus signs the diffusion loss corrected collection of stage 1, open dots the collection efficiency of the inlet, and lines the fittings to measurements. Numbers indicate different stages. Fitted parameters are the cutpoints, steepnesses, and the effective tube length (Equations (2.6) and (2.7)). Table 4.3 shows the results of the fitting. The volumetric flow rate (Q) is $1.2\,\mathrm{l\,min^{-1}}$ for all cases.

All the stages except the first have similar steepnesses, and they correspond with the slit type impactor collection efficiency curves introduced in **Paper 2**. The tails of the stages are caused by diffusion and losses of image charge. The lower steepness in the stage 1 collection efficiency may have been caused by uncertainty in diffusion loss correction; that is, uncertainty in fitting the losses curve. Figure 4.12 (c) shows the kernels of the HRLPI. The penetration of the inlet reduces mainly the height of the outermost stage kernels. The first and the seventh channel have the narrowest measurement size ranges, which further reduce the heights of their kernels.

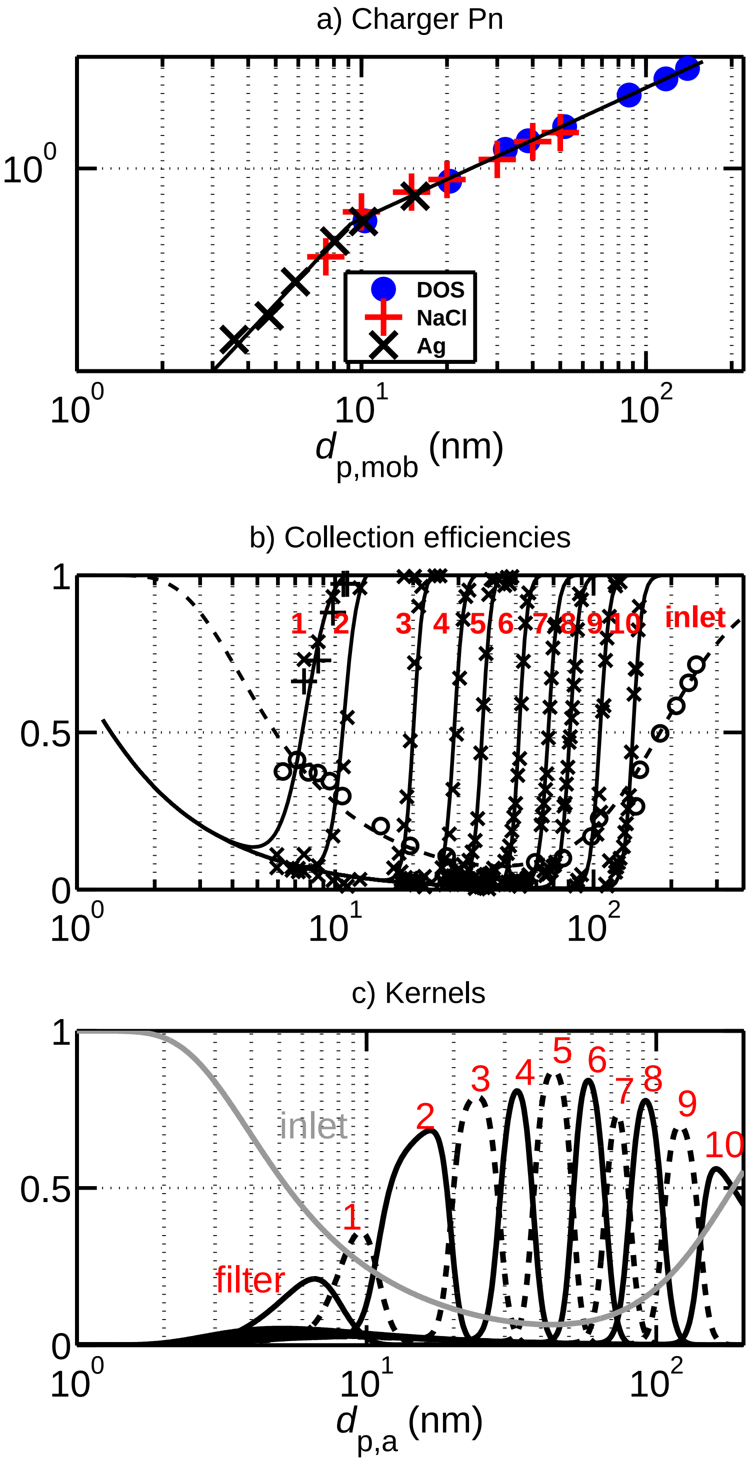

Figure 4.12: Calibration results of charger and HRLPI impactor with inlet (**Paper 4**).

stage	$d_{p,50}$ (nm)	s	L(m)
1	7.7	5	0.01
2	10.8	8.1	0.01
3	19.5	12.2	0.01
4	28.7	11.5	0.01
5	37.6	12.7	0.01
6	51.5	13.5	0.01
7	66.8	11.9	0.01
8	81	12.1	0.01
9	105.9	12	0.01
10	142	12.6	0.01
inlet	183	-	-

Table 4.3: Values of fitted parameters for each stage and the inlet.

4.4.3 Test measurements

Figure 4.13 (a) shows the measurement results of DOS particle size distributions generated with an ECG. The aerodynamic size distributions measured with the impactors were transformed to mobility size distributions by assuming the bulk density of DOS ($0.92\,\mathrm{g\,cm^{-3}}$). The HRLPI, EEPS, and SMPSs can still resolve the mode location of the size distributions. The EEPS and SMPSs also measure the left side of the distribution in more detail than the HRLPI.

Figure 4.13 shows externally mixed DOS and NaCl aerosol particle size distributions measured with different instruments. DOS particles were generated with the ECG and NaCl particles by evaporating NaCl in a tube furnace and then rapidly diluting the vapour to almost room temperature. NaCl aerosol was first classified with a DMA, after which it was mixed with polydisperse DOS aerosol.

In the bimodal case, the HRLPI performed well. The concentration of the narrow NaCl mode measured with the HRLPI was lower than that of the SMPS because aerodynamic size distributions were calculated assuming unit density for particles. If the correct effective density had been used in the NaCl mode, Pn-values would have been smaller, which would have brought HRLPI concentrations to the same level as in SMPS distributions. However, when the effective densities of the particles are not known, size distributions measured with the impactor are usually calculated assuming unit density. Steep cut-curves and a great number of measurement channels significantly improved the resolving power of the HRLPI in size distribution measurements over the EELPI and the ELPI+. The distance between the modes was slightly smaller in distributions measured with the SMPSs and EEPS than that measured with the HRLPI. This was an expected result, as the effective density of NaCl particles in this size range was larger than $1\,\mathrm{g\,cm^{-3}}$, and as, correspondingly, their aerodynamic sizes were larger than the mobility size. The EEPS resolves only one mode, which could be explained, for example, by the high smoothness assumption in the inversion of the size distribution.

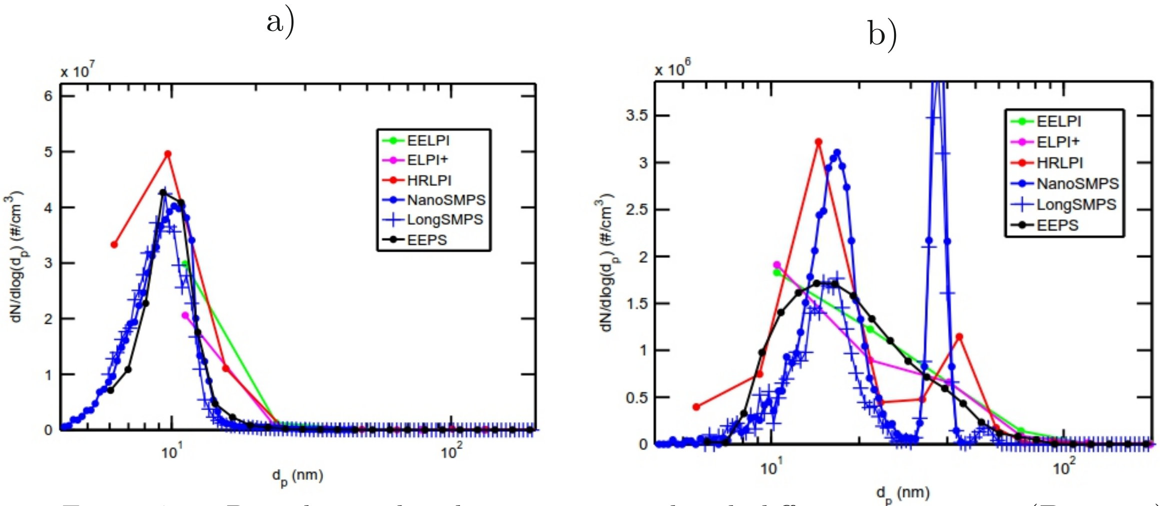

Figure 4.13: Particle size distributions measured with different instruments (**Paper 4**): (a) DOS aerosol, GMD 17 nm (b) bimodal, externally mixed DOS and NaCl aerosols.

Chapter 5

Summary

This thesis focused on low pressure impactors using numerical and experimental methods. The main themes were to validate a numerical modeling approach for a low pressure impactor and to study the effect of flow field characteristics on the shape of the collection efficiency curve. The results were then applied to practise. Two new impactors were devised: a variable nozzle area impactor (VNAI) and a high-resolution low-pressure cascade impactor (HRLPI). The VNAI was used to determine the critical velocity of the rebound for silver particles, and the HRLPI was calibrated and performance-tested with laboratory measurements.

The suitability of CFD modeling for low pressure impactors was studied by simulating the collection efficiencies of the well characterized ELPI impactor. At a low turbulence level, CFD simulation provided information on the details of low pressure impactor operation.

The effect of the collection plate distance on resolution was studied with a low turbulence level LPI. A maximum was discovered in the resolution when the ratio of the jet-to-plate distance to jet diameter was two, and that resolution remained reasonable in a range 0.5 to 5. Weakening of the resolution with too low or high collection plate distances was related to increasing variations in the impaction conditions in the jet cross section. The steepness of the collection efficiency curve at slit and round nozzle impactor stages with two different throat lengths was studied by experiment and numerical simulation. A shorter nozzle produced a better resolution at both slit nozzle and round nozzle LPI stages. At comparable cutpoint stages, the resolution of the short throat slit nozzle was higher than that of many other well-known LPIs. In terms of its width, the short nozzle throat leaves the jet exit plane velocity profile under-developed, resembling a plug flow. This creates uniform impaction conditions across the jet, except at its very outer edges. Impaction velocities of particles of 25 nm to 40 nm were also simulated. The steep cut-curve impactor also generates uniform impaction velocities for monodisperse particles.

Uniform impaction conditions are beneficial in applications where it is important to control the impaction energy of particles, such as in studying particle bounce and charge transfer in nanoparticle impactions. Based on the results of the slit nozzle impactor, a VNAI impactor was designed and built to study the critical velocity of rebound and charge transfer. The VNAI consisted of a slit type impactor, whose slit length could be varied from 3 to 30 mm. Particle impaction velocities could then be varied by changing the slit length. Using VNAI dimensions and a slit value corresponding to the onset of bounce, particle impaction velocities were simulated with the CFD model. Critical velocities were determined for silver particles in a size range of 20 nm – 1 µm. Results showed that the critical velocity of the rebound decreases from $14\,\mathrm{m\,s^{-1}}$ to $0.022\,\mathrm{m\,s^{-1}}$ as the particle size increases by 20 nm – 1000 nm. An exponential decay was observed, and a proportionality to the power of -1.60 of particle size was maintained throughout the wide size range. This is in line with several earlier experimental studies on above micron sized particles (Wall et al., 1990). However, a difference in critical velocities of several orders of magnitude exists between different particle–surface material pairs. This may be only a material-pair-dependent difference, yet it remains unclear how different measurement methods can cause such large differences.

The developed steep, cut-curve impactor stage inspired also exploration of the limits of cascade impactor measurement. Theoretical simulations of instrument response showed that in many applications the optimal number of stages per size decade is roughly 10. Cascade impactor measurement combined with electrical detection of particles enables real-time measurements of aerodynamic size distribution. Response simulations revealed that steep cut-curves could improve the robustness of the inversion in real-time measurement. To test the practical optimal design of a cascade impactor, a new high-resolution low-pressure cascade impactor (HRLPI) was built, characterized, and performance-tested. It was fitted in an ELPI housing to enable electrical measurement. Calibrations showed that the lowest cutpoint was 7.7 nm and the highest 142 nm. The inlet pressure had to be reduced to 40 mbar to squeeze stage cutpoints below 150 nm. A low operation pressure and densely packed cutpoints provided the advantage of low particle impaction velocities in the HRLPI to curb particle bounce. Calibration measurements showed that HRLPI cut-curve steepnesses are similar to those of a single slit impactor stage. Steep cut-curves minimize cross sensitivity between HRLPI stages and ensure that even the simplest data deconvolution, the cutpoint concept, works fine with the HRLPI. The HRLPI was compared with several commercially available instruments. It and the NanoSMPS showed similar size distributions for monomodal dioctylsebacate (DOS) particles whose GMD was 10 nm. For bimodal size distribution, where the DOS mode was located at around 15nm and NaCl at around 30 nm, only the SMPSs and the HRLPI could resolve the shape of these distributions. This can be regarded as a significant improvement in size resolution over ELPI or Berner impactors.

5.1 Conclusions and outlook

Impactors constitute a rather mature field in aerosol science. Nevertheless, as shown in this thesis, new information is still possible to obtain on low pressure impactor operation allowing further development of impactors. This research showed that a sharp collection efficiency curve can be achieved by keeping the impactor jet velocity profile under-developed in the nozzle and in the free jet after the nozzle. This can be realized by using a short nozzle throat and a short jet-to-plate distance. Furthermore, numerical simulations showed that monodisperse particles have uniform impaction velocities at a sharp cut-curve stage.

Sharp cut-curve stages were successfully used in two new impactors: a variable nozzle area impactor (VNAI) and a high-resolution, low-pressure cascade impactor (HRLPI). The VNAI was used to study the critical velocity of the rebound for spherical silver particles in a wide particle size range. In terms of method accuracy, results supported a previous study on silver nanoparticles, but for micron size particles, the results were lower by several orders of magnitude. The large deviation could be explained by differences in material pairs, but also the effect of different research methods on results should be tested. The same material pairs as in previous studies could be tested with the setup used in this thesis. The HRLPI was calibrated and performance-tested, and it doubled the size resolution in the sub-100 nm size range compared to previous cascade impactors. To realize the full potential of the HRLPI, an advanced inversion method should be tested on it. Sensitivity to particle bounce could also be characterized, as it should be minimal according to the design of the impactor.

For any advances in future impactor technology, two major challenges are waiting to be taken on: an efficient method to charge nanoparticles and a way to inhibit particle rebound. Hopefully, the results of this thesis will prove useful in solving the problem of particle bounce and any emerging aspects about nanoparticles.

Bibliography

Andersen, A. A. New sampler for the collection, sizing, and enumeration of viable airborne particles. *Journal of Bacteriology*, 75(5):471–484, 1985.

Bartosiewicz, Y., Aidoun, Z., Desevaux, P., and Y., M. Numerical and experimental investigations on supersonic ejectors. *International Journal of Heat and Fluid Flow*, 26:56–70, 2005.

Berner, A. Praktische Erfahrungen mit einem 20-Stufen-Impactor. *Staub-Reinhalt. Luft.*, 32:315, 1972.

Biswas, P. and Flagan, R. C. High-velocity inertial impactors. *Environ. Sci. Technol.*, 18:611 – 616, 1984.

Brockmann, J. E. *Aerosol Measurement; Principles Tecniques and Applications.* John Wiley & Sons, Inc., 2001. Chapter 8: Sampling and Transport of Aerosols.

Chen, B. T., Cheng, Y. S., and Yeh, H. C. Performance of a tsi aerodynamic particle sizer. *Aerosol Science and Technology*, 4(1):89–97, 1985.

Chen, D.-R., Pui, D., Hummes, D., Fissan, H., Quant, F., and Sem, G. Design and evaluation of a nanometer aerosol differential mobility analyzer (nano-dma). *Journal of Aerosol Science*, 29(56):497 – 509, 1998.

Cheng, Y.-S. and Yeh, H.-C. Particle bounce in cascade impactors. *Environmental Science and Technology*, 13(11):1392–1396, 1979.

Cooper, D. and Guttrich, G. A study of the cut diameter concept for interpreting particle sizing data. *Atmospheric Environment*, 15(9):1699–1707, 1981.

Dahneke, B. The capture of aerosol particles by surfaces. *Journal of Colloid and Interface Science*, 37(2):342 – 353, 1971.

de la Mora, J. F., Rao, N., and McMurry, P. Inertial impaction of fine particles at moderate reynolds numbers and in the transonic regime with a thin-plate orifice nozzle. *Journal of Aerosol Science*, 21(7):889 – 909, 1990.

D'Ottavio, T. and Goren, S. L. Aerosol capture in granular beds in the impaction dominated regime. *Aerosol Science and Technology*, 2(2):91–108, 1982.

Ehara, K., Hagwood, C., and Coakley, K. J. Novel method to classify aerosol particles according to their mass-to-charge ratioaerosol particle mass analyser. *Journal of Aerosol Science*, 27(2):217 – 234, 1996.

Esmen, N. A., Ziegler, P., and Whitfield, R. The adhesion of particles upon impaction. *Journal of Aerosol Science*, 9(6):547–556, 1978.

Flagan, R. C. Compressible flow inertial impactors. *Journal of Colloid and Interface Science*, 87:291–299, 1982.

Friedlander, S. Polymer-like behavior of inorganic nanoparticle chain aggregates. *J. Nanopart. Res.*, 1:9–15, 1999.

Froeschke, S., Kohler, S., Weber, A. P., and Kasper, G. Impact fragmentation of nanoparticle agglomerates. *Journal of Aerosol Science*, 34(3):275–287, 2003.

Fuchs, N. A. Aerosol impactors. In Shaw, D. T., editor, *Fundamentals of aerosol science*, pages 1–83. John Wiley & sons, Inc., New York, 1978.

Gómez-Moreno, F., Rosell-Llompart, J., and Mora, J. F. d. l. Turbulence transition in impactor jets and its effects on impactor resolution. *J. Aerosol Sci.*, 33:459–476, 2002.

Hansen, P. C. *Rank-deficient and discrete ill-posed problems: numerical aspects of linear inversion*, volume 4. Siam, 1998.

Hari, S., Hassan, Y. A., and McFarland, A. R. Aerodynamic focusing effect in a reactangular slit real impactor at different reynolds numbers. *Particle & Particle Systems Characterization*, 23:457–467, 2006.

Harra, J., Mäkitalo, J., Siikanen, R., Virkki, M., Genty, G., Kobayashi, T., Kauranen, M., and Mäkelä, M., J. Size-controlled aerosol synthesis of silver nanoparticles for plasmonic materials. *Journal of Nanoparticle Research*, 14(6):870, 2012.

Hering, S. V. Calibration of the QCM impactor for stratospheric sampling. *Aerosol Science and Technology*, 7:257 – 274, 1987.

Hillamo, R. E. and Kauppinen, E. I. On the performance of the berner low pressure impactor. *Aerosol Science and Technology*, 14:33 – 47, 1991.

Hinds, W. C. *Aerosol Technology.* John Wiley & Sons, Inc., 1998.

Huang, C.-H., Tsai, C.-J., and Shih, T.-S. Particle collection efficiency of an inertial impactor with porous metal substrates. *Journal of Aerosol Science*, 32 (9):1035 – 1044, 2001.

Hutter, E. and Fendler, J. Exploitation of localized surface plasmon resonance. *Advanced Materials*, 16(19):1685–1706, 2004.

Ihalainen, M., Lind, T., Arffman, A., Torvela, T., and Jokiniemi, J. Break-up and bounce of tio2 agglomerates by impaction. *Aerosol Science and Technology*, 48 (1):31–41, 2014.

Järvinen, A., Aitomaa, M., Rostedt, A., Keskinen, J., and Yli-Ojanper, J. Calibration of the new electrical low pressure impactor (ELPI+). *Journal of Aerosol Science*, 69(0):150 – 159, 2014.

Johnson, T., Caldow, R., Pöcher, A., Mirme, A., and Kittelson, D. A new electrical mobility particle size spectrometer for engine exhaust particle measurements. *SAE Technical Paper Series*, 2004. 2004-01-1341.

Jurcik, B. and Wang, H. On the shape of impactor efficiency curves. *J. Aerosol Sci.*, 26:1139–1147, 1995.

Juuti, P., Arffman, A., Rostedt, A., Harra, J., Mäkela, J., and Keskinen, J. Real-time effective density monitor (DENSMO) for aerosol nanoparticle production. *Aerosol Science and Technology*, 2015. Submitted.

Kauppinen, E., Hillamo, R., Ruuskanen, J., Hakkarainen, T., and Rouhiainen, P. Theoretical and experimental study of particle collection characteristics of high-velocity multijet cascade impactors. *J. Aerosol Sci.*, 17:506–510, 1986.

Keskinen, J., Pietarinen, K., and Lehtimäki, M. Electrical low pressure impactor. *J. Aerosol Sci.*, 23:353–360, 1992.

Keskinen, J., Marjamäki, M., Virtanen, A., Mäkelä, T., and Hillamo, R. Electrical calibration method for cascade impactors. *Journal of Aerosol Science*, 30:111–116, 1999.

Kittelson, D. B. Engines and nanoparticles: A review. *J. Aerosol Sci.*, 29(5/6), 1998.

Knutson, E. and Whitby, K. Aerosol classification by electric mobility: apparatus, theory, and applications. *Journal of Aerosol Science*, 6(6):443–451, 1975.

Kruis, F. E., Fissan, H., and Peled, A. Synthesis of nanoparticles in the gas phase for electronic, optical and magnetic applicationsa review. *Journal of Aerosol Science*, 29(56):511 – 535, 1998.

Kulmala, M., Pirjola, L., and Mäkelä, J. Stable sulphate clusters as a source of new atmospheric particles. *Nature*, 404(6773):66–69, 2000.

Kuuluvainen, H., Arffman, A., Saukko, E., Virtanen, A., and Keskinen, J. A new method for characterizing the bounce and charge transfer properties of nanoparticles. *Journal of Aerosol Science*, 55(0):104 – 115, 2013.

Leduc, S., Fredriksson, C., and Hermansson, R. Particle-tracking option in fluent validated by simulation of a low-pressure impactor. *Advanced Powder Technology*, 17:99–111, 2006.

Lemmetty, M., Marjamäki, M., and Keskinen, J. The ELPI response and data reduction II: Properties of kernels and data inversion. *Aerosol Science and Technology*, 39(7):583–595, 2005.

Levin, M., Gudmundsson, A., Pagels, J. H., Fierz, M., Mlhave, K., Lndahl, J., Jensen, K. A., and Koponen, I. K. Limitations in the use of unipolar charging for electrical mobility sizing instruments: A study of the fast mobility particle sizer. *Aerosol Science and Technology*, 49(8):556–565, 2015.

Liu, B. and Lee, K. W. An aerosol generator of high stability. *American Industrial Hygiene Association Journal*, 36(12):861–865, 1975.

Marjamäki, M., Lemmetty, M., and Keskinen, J. ELPI response and data reduction I: Response functions. *Aerosol Science and Technology*, 39:575–582, 2005.

Marjamäki, M. *Electrical Low Pressure Impactor: Modifications and Particle Collection Characteristics*. PhD thesis, Tampere University of Technology, 2003.

Marjamäki, M. and Keskinen, J. Effect of impaction plate roughness and porosity on collection efficiency. *Journal of Aerosol Science*, 35(3):301 – 308, 2004a.

Marjamäki, M. and Keskinen, J. Estimation of the cutpoint of an impactor with porous substrates. *Journal of Aerosol Science*, 35(5):657 – 663, 2004b.

Marjamäki, M., Keskinen, J., Chen, D.-R., and Pui, D. Y. Performance evaluation of the electrical low-pressure impactor(ELPI). *Journal of Aerosol Science*, 31 (2):249 – 261, 2000.

Marple, V., Liu, B., and Whitby, K. On the flow fields of inertial impactors. *ASME Journal of Fluids Engineering*, 96:394, 1974.

Marple, V. *A fundamental study of inertial impactors.* PhD thesis, University of Minnesota, 1970.

Marple, V. A. and Liu, B. Y. H. Characteristics of laminar jet impactors. *Environ. Sci. Technol.*, 8:648 – 654, 1974.

Marple, V. A. and Olson, B. A. *Sampling and Measurement Using Inertial, Gravitational, Centrifugal, and Thermal Techniques*, pages 129–151. John Wiley & Sons, Inc., 2011. ISBN 9781118001684.

Marple, V. A., Rubow, K. L., and Behm, S. M. A micro-orifice uniform deposit impactor (MOUDI): Description, calibration, and use. *Aerosol Science and Technology*, 14(4):434–446, 1991.

Marquard, A., Meyer, J., and Kasper, G. Characterization of unipolar electrical aerosol chargers – Part I: A review of charger performance criteria. *Journal of Aerosol Science*, 37(9):1052 – 1068, 2006.

Menter, F. R. Two-equation eddy-viscosity turbulence models for engineering applications. *AIAA*, 32:1598–1605, 1994.

Mercer, T. T. and Chow, H. Y. Impaction from reactangular jets. *Journal of Colloid and Interface Science*, 27:75–83, 1968.

Mirme, A. *Electric Aerosol Spectrometry.* PhD thesis, University of Tartu, 1994.

Moisio, M., Marjamäki, M., Virtanen, A., and Keskinen, J. Correction algorithm for fine particle losses in cascade impactor. *Journal of Aerosol Science*, 30, Supplement 1(0):S773 – S774, 1999. Proceedings of the 1999 European Aerosol Conference.

Rao, A. K. and Whitby, K. T. Nonideal collection characteristics of single stage and cascade impactors. *American Industrial Hygiene Association Journal*, 38 (4):174–179, 1977.

Reavell, K., Hands, T., and Collings, N. A fast response particulate spectrometer for combustion aerosols. *SAE Technical Paper*, 2002. 2002-01-2714.

Rennecke, S. and Weber, A. The critical velocity for nanoparticle rebound measured in a low pressure impactor. *Journal of Aerosol Science*, 58(0):135 – 147, 2013.

Rennecken, S. and Weber, A. A novel model for the determination of nanoparticle impact velocity in low pressure impactors. *Journal of Aerosol Science*, 55:89–103, 2013.

Rogers, L. N. and Reed, J. The adhesion of particles undergoing an elastic-plastic impact with a surface. *Journal of Physics D: Applied Physics*, 17(4):677–689, 1984.

Scheibel, H. G. and Porstendörfer, J. Generation of monodisperse Ag- and NaCl-aerosols with particle diameters between 2 and 300 nm. *Journal of Aerosol Science*, 14(2):113–126, 1983.

Seipenbusch, M., Toneva, P., Peukert, W., and Weber, A. P. Impact fragmentation of metal nanoparticle agglomerates. *Particle and Particle Systems Characterization*, 24(3):193–200, 2007.

Seipenbusch, M., Rothenbacher, S., Kirchhoff, M., Schmid, H.-J., Kasper, G., and Weber, A. Interparticle forces in silica nanoparticle agglomerates. *Journal of Nanoparticle Research*, 12(6):2037–2044, 2010.

Stefancová, L., Schwarz, J., Mäkelä, T., Hillamo, R., and Smolík, J. Comprehensive characterization of original 10-stage and 7-stage modified berner type impactors. *Aerosol Science and Technology*, 45(1):88–100, 2011.

Stern, S. C., Zeller, H. W., and Schekman, A. I. Collection efficiency of jet impactors at reduced pressures. *Industrial & Engineering Chemistry Fundamentals*, 1(4):273–277, 1962.

Tammet, H., Mirme, A., and Tamm, E. Electrical aerosol spectrometer of tartu university. *Atmospheric Research*, 62(34):315 – 324, 2002.

Tavakoli, F. and Olfert, J. An instrument for the classification of aerosols by particle relaxation time: Theoretical models of the aerodynamic aerosol classifier. *Aerosol Science & Technology*, 47:916 – 926, 2013.

Vanderpool, R., Lundgren, D., and Kerch, P. Design and calibration of an in-stack low-pressure impactor. *Aerosol Science and Technology*, 12:215–224, 1990.

Vinchurkar, S., Longest, P. W., and Peart, J. CFD simulations of the andersen cascade impactor: Model development and effects of aerosol charge. *J. Aerosol Sci.*, 40:807–822, 2009.

Virtanen, A., Joutsensaari, J., Koop, T., Kannosto, J., Yli-Pirilä, P., Leskinen, J., Mäkelä, J., Holopainen, J., Pöschl, U., Kulmala, M., Worsnop, D., and Laaksonen, A. An amorphous solid state of biogenic secondary organic aerosol particles. *Nature*, 467:824–827, 2010.

Wall, S., John, W., Wang, H.-C., and Goren, S. L. Measurements of kinetic energy loss for particles impacting surfaces. *Aerosol Science and Technology*, 12 (4):926–946, 1990.

Wang, H.-C. and John, W. Dynamic adhesion of particles impacting a cylinder. In *Particles on Surfaces 1: Detection, Adhesion, and Removal*, pages 211–224. Plenum Press, New York, 1988.

Yli-Ojanperä, J., Mäkelä, J. M., Marjamäki, M., Rostedt, A., and Keskinen, J. Towards traceable particle number concentration standard: Single charged aerosol reference (SCAR). *Journal of Aerosol Science*, 41(8):719 – 728, 2010.

Paper 1

Arffman, A., Marjamäki, M. and Keskinen, J., Simulation of low pressure impactor collection efficiency curves, *Journal of Aerosol Science*, 42, 329-340, 2011.

Journal of Aerosol Science 42 (2011) 329–340

Contents lists available at ScienceDirect

Journal of Aerosol Science

journal homepage: www.elsevier.com/locate/jaerosci

Simulation of low pressure impactor collection efficiency curves

A. Arffman *, M. Marjamäki, J. Keskinen

Tampere University of Technology, Department of Physics, Aerosol Physics Laboratory, P.O. Box 692, FI-33101 Tampere, Finland

ARTICLE INFO

Article history:
Received 26 February 2010
Received in revised form
10 February 2011
Accepted 10 February 2011
Available online 19 February 2011

Keywords:
Cascade impactor
CFD
ELPI
QCM
Collection efficiency
Particle cutoff

ABSTRACT

The collection efficiency of the low pressure impactors has been studied using numerical simulations. Flow field was modeled by solving the equations describing the time-average flow field (RANS) with a commercial CFD solver. Particle tracks were calculated separately using Lagrangian methods. Simulation results were verified against published experimental results. Effect of turbulent velocity fluctuations on the impactor resolution was investigated by comparing the ratio of the simulated to experimental impactor resolutions as a function of the turbulence level of the jet. It was found that the turbulence is the dominant mechanism reducing the resolution when the local Reynolds number is over 1800. Effect of jet-to-plate distance on the resolution of the low pressure impactor was studied in the case of low turbulence level. Highest resolution was achieved when the ratio of jet diameter to jet to plate distance (S/W) is 2. When the ratio is lower or higher, resolution is reduced because there is an increase in nonuniformity of the impaction conditions across the jet.

1. Introduction

Impactors have been used since the end of the 19th century in aerosol science to classify particles according to their size. One widely used method is to use impactor stages in a cascade configuration to measure the size distribution of the particles. In cascade impactors, several impactor stages with varying cutpoints are placed in series. To achieve lower cutpoints, low pressure impactors have been introduced. In cascade low pressure impactors the pressure is reduced either by having a separate pressure reducing stage (e.g. Hering, Flagan, & Friedlander, 1978, 1979) or by gradually reducing the pressures by using high jet velocities (e.g. Berner, 1972; Vanderpool, Lundgren, & Kerch, 1990).

Several theoretical and numerical studies have been conducted to evaluate the effects of design and flow conditions on the operation of the impactor. The foundation was laid by Marple (e.g. Marple & Liu, 1974; Marple, Liu, & Whitby, 1974; Rader & Marple, 1985). Jurcik and Wang (1995) studied the effect of geometry on the shape of the collection efficiency curves. Swanson, Muzzio, Annapragada, and Adjei (1996) modeled a low flow rate single orifice cascade impactor. Asgharian, Zhang, and Fang (1997) made theoretical calculations of the collection efficiency of spherical particles and fibers in an impactor. Vinchurkar, Longest, and Peart (2009) modeled the Andersen impactor and studied the effect of particle charge on the collection efficiency. These studies have assumed constant fluid properties. Much less work has been done on the compressible and partially turbulent flow range where many of the practical low pressure impactors work. Leduc, Fredriksson, and Hermansson (2006) used particle tracking in Fluent software to calculate the collection efficiencies of a low pressure impactor. In their study they found that the method was valid only for low velocities and

---

* Corresponding author.
E-mail addresses: anssi.arffman@tut.fi (A. Arffman), marko.marjamaki@tut.fi (M. Marjamäki), jorma.keskinen@tut.fi (J. Keskinen).

0021-8502/$ - see front matter © 2011 Elsevier Ltd. All rights reserved.
doi:10.1016/j.jaerosci.2011.02.006

Reynolds numbers. No successful computational study has been published on the factors defining the shape of the collection efficiency curve of the widely used high jet velocity, low pressure impactor. In this study we will present a modeling method that can accurately predict the cutpoints of the low pressure impactor and within the certain limits also the shape of the collection efficiency curve.

The calculation of the Stokes and Reynolds numbers is not trivial in the case of compressible flow, reduced pressure cascade impactors, since the stagnation conditions vary from stage to stage. Usually the pressure on the impaction plate is assumed to be equal to the stagnation pressure before the jet (Biswas & Flagan, 1984; Flagan, 1982). The flow inside the impactor is assumed to be adiabatic and jet velocities are calculated assuming adiabatic conditions (Hering, 1987; Hillamo & Kauppinen, 1991). A semi-empirical method is conventionally used to scale the impactor cutpoint by changing the pressure conditions or jet velocities once the critical Stokes number of the stage has been defined experimentally. This method requires measurements and does not provide information on the shape of the collection efficiency curve. For example, an important parameter characterizing collection efficiency curve is its steepness and conditions in the flow field that define it. Successful modeling effort can bring new beneficial information, for example when trying to understand the factors affecting the resolution of the impactor.

The objective of this study is to introduce and validate a CFD simulation approach that correctly describes the cutpoints and within certain limits the shape of the collection efficiency curve of the low pressure impactor. Validation of the simulation is based on comparisons of numerically predicted cutpoint diameters of the ELPI and the QCM impactors with the existing experimental data. Simulation is based on the time-averaged flow fields which excludes the direct effects of the turbulent velocity fluctuations on particle tracks. Therefore, the range of flow conditions, where the time-averaged approach works was verified. This was achieved by comparing experimental and simulated collection efficiencies with the modeling parameter that describes the intensity of turbulence in the impactor jet. The model was then applied to predict the flow fields and cut curves of the impactor stage and to characterize the flow field dynamics inside the low pressure impactor. The model is used to characterize the effect of the collection plate distance and the flow field properties on the resolution of the impactor.

2. ELPI and QCM impactors

In this study, the low pressure stages of the ELPI (Keskinen, Pietarinen, & Lehtimäki, 1992) and the QCM (Hering, 1987) cascade impactors were simulated and used for validating the technique. ELPI (Electrical Low Pressure Impactor) is a 13-stage cascade impactor which measures electrically the number concentration of the particles in the sample air. The impactor stages of the ELPI use multiple jets and low pressures. The stages operate in the pressure range of 40–1000 mbar and in the jet velocity range of 3–340 m/s. Besides the commercially available stages of the ELPI, an extra stage (Yli-Ojanperä, Kannosto, Marjamäki, & Keskinen, 2010) with a cutpoint of 17 nm is also simulated. The extra stage is installed as the last stage of the cascade. Specifications of the ELPI impactor stages (Marjamäki, 2003) are collected in Table 1.

QCM (Quartz Crystal Microbalance) is a 10-stage cascade impactor (Hering, 1987) that uses piezo-electric quartz crystal collection plates to measure the mass concentration of the particles in the sample air. The QCM uses from one to four jets in each stage. The stages having the smallest cutpoints work in the reduced pressure conditions. Pressure is reduced using a pressure drop valve. The low pressure stages operate in the pressure range of 50–120 mbar. The details of the QCM impactor stages are collected in Table 2.

Table 1
Details of the ELPI impactor unit. $d_{p,50}$ is the cutpoint of the stage, W is the nozzle diameter, Re_j is the jet Reynolds number and S is jet-to-plate spacing. Stage pressure is the static pressure downstream of the impaction plate. Details of the stages 1–12 can be found in Marjamäki (2003) and for the extra stage in Yli-Ojanperä et al. (2010).

Stage	$d_{p,50}$ (μm)	Nozzles	W (mm)	S/W	Re_j	Pressure (kPa)	Pressure ratio
Extra	0.015	174	0.3	3		3.9	0.39
1	0.029	69	0.3	3	1250	10.0	0.445
2	0.055	58	0.25	3.6	1490	22.47	0.597
3	0.092	21	0.3	3	3490	37.64	0.563
4	0.154	19	0.3	3	2970	66.82	0.769
5	0.261	27	0.3	3	1770	86.94	0.918
6	0.38	50	0.3	3	900	94.70	0.977
7	0.61	48	0.4	3	700	96.96	0.992
8	0.95	20	0.7	3	950	97.76	0.995
9	1.6	17	1	2.5	780	98.26	0.998
10	2.4	14	1.4	2.1	680	98.41	0.999
11	4.0	3	3.2	2.0	1380	98.48	1.000
12	6.7	1	6.3	1.9	2110	98.51	1.000

Table 2
Details of the QCM impactor unit. $d_{p,50}$ is the cutpoint of the stage, W is the nozzle diameter, Re_j is the jet Reynolds number and S is jet-to-plate spacing. Stage pressure is the static pressure downstream of the impaction plate. More information can be found in Hering (1987).

Stage	$d_{p,50}$ (μm)	Nozzles	W (mm)	S/W	Re_j	Pressure (kPa)	Pressure ratio
4	–	1	3.38	0.5	108	11.73	1
5	2.1	1	2.14	0.5	170	11.73	1
6	0.93	1	1.47	0.5	248	11.66	0.994
7	0.25	7	1.06	0.5	344	11.46	0.9828
8	0.15	8	0.8	0.5	455	10.26	0.895
9	0.065	9	0.5	0.5	364	7.86	0.766
10	–	10	0.31	0.5	294	5.06	0.644

3. Modeling method

3.1. Solving the flow field

The flow field inside the impactor nozzles was simulated by using an axisymmetric form of the Favre averaged (density weighted time averaging) Navier–Stokes (N–S) equations and numerically solved by employing the CFD package of Fluent 6. The Favre averaged versions of the N–S equations have to be used when the flow is compressible like it is in the case of a low pressure impactor. Time averaging of the original N–S equations produces extra correlation terms in the original equations and a so-called turbulence model is needed to close the equation system. The turbulence model used in this study was the SST$-k-\omega$-model (Menter, 1994). It consists of two convection–diffusion type partial differential equations for the turbulence parameters k and ω. The k parameter is the turbulence kinetic energy which describes the intensity of the turbulent velocity fluctuations and ω is the specific dissipation rate of the turbulence kinetic energy. These turbulence transfer equations are coupled through turbulent viscosity to the N–S equations, and all equations are solved simultaneously. The SST$-k-\omega$-model was chosen because it has been reported to predict flow separation correctly in the presence of the adverse pressure gradient and it is not very sensitive to the inflow boundary values of turbulence quantities (Menter, 1994). The flow field was solved numerically all the way down to the viscosity affected laminar sublayer at the solid surfaces by using Fluent's advanced wall treatment. The advanced wall treatment employs the Wolfhstein's single equation model when the dimensionless wall Reynolds number Re_y is less than 200. The axisymmetric form of the flow equations limits the investigation to a single nozzle from each stage and the effects related to multiple jets in the same stage cannot be directly seen in the modeling results.

The inflow and outflow boundary conditions were the upstream and downstream stagnation pressures and the no-slip condition was applied for the flow velocities at the solid walls. Inflow boundary conditions for the turbulence quantities were estimated according to the recommendations of Fluent's manual. Values for the k and ω parameters were defined by setting the value for turbulence intensity and the length scale. Estimation for the intensity was 1% and for the length scale 0.1 mm. Values at the solid walls for the turbulence quantities were internally taken care by Fluent.

Boundary conditions and geometry with velocity contours are presented in Fig. 1(a). The computational geometries and the grids were created using the Fluent pre-processor Gambit. The grids were made most dense in the area that is crucial for the impaction phenomena. The dimensionless wall coordinate y^+ was kept in the order of magnitude 1 at every wall, as demanded by the advanced wall treatment. To make sure that the grid was dense enough the results were calculated using denser grids and choosing the grid after which the results did not change anymore. The number of control volumes used for the different geometries are presented in Table 3.

The convergence of the results was confirmed by following the development of the residuals and the flow field variables during the iterative solution procedure. Calculation was stopped when the average values of the velocity, pressure, turbulence kinetic energy and turbulent viscosity did not change anymore at vicinity of the impactor collection plate.

When the ratio of downstream to upstream pressure of the impactor nozzle is reduced to the order of 0.5, the flow is choked. Although a straight nozzle geometry is used, it is possible that the shape of the flow field resembles a Laval-nozzle type flow. If the pressure ratio is further reduced, the flow can accelerate to supersonic velocities. When the supersonic flow impacts on a body or a wall, shockwaves can be formed, and their effect on the operation of the impactor has to be considered. Effects of the possible shock waves in this study are included via the SST$-$k$-\omega$-model. It is capable of predicting the formation of the shock waves at least roughly as pointed out by Bartosiewicz, Aidoun, Desevaux, and Mercadier (2005). The minimum pressure ratio in the study is approximately 0.4. This means that the flow velocity after the nozzle is between the sonic and the transonic flow regime and the effects related to shock waves are possible.

3.2. Solving the particle trajectories and the impactor collection efficiency

Particle trajectories were calculated after the flow field had been solved. This means that there was a one-way coupling from the flow to the particles but not vice versa. The flow field solution data was exported from Fluent to the Matlab environment. A simple adaptive Euler method was implemented as a Matlab script and used for integrating the particle

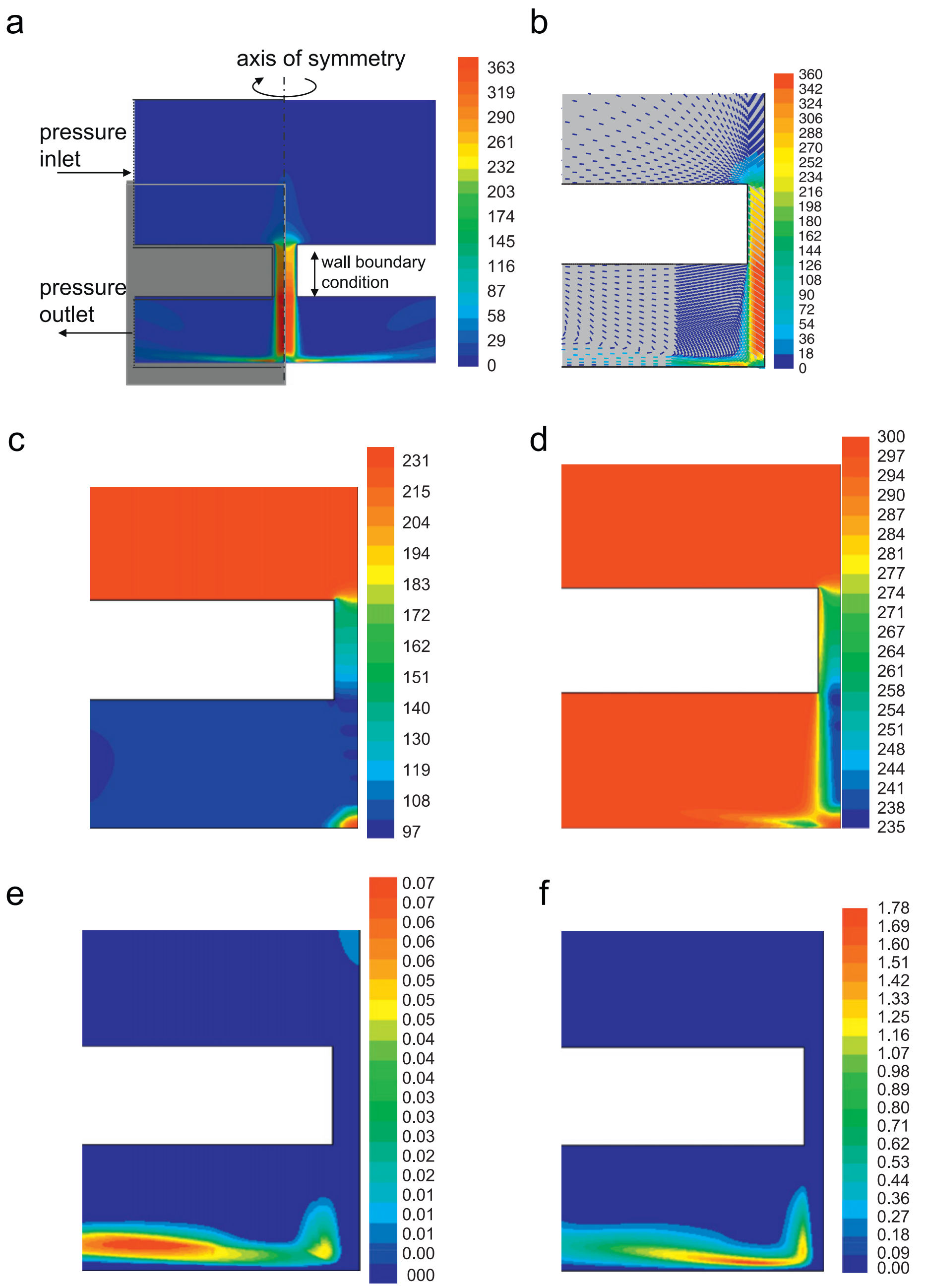

Fig. 1. Contours of scalars and velocity vectors from the first stage of the ELPI. (a) shows the cross-section of the jet velocity contours. Only the shaded area is magnified in the other figures. (a) Magnitude of the velocity (m/s). (b) Velocity vectors (m/s). (c) Static pressure (hPa). (d) Static temperature (K). (e) Ratio of turbulent to laminar viscosity. (f) Turbulence intensity (normalized with the maximum local of the jet velocity) (%).

trajectories in the flow fields. The method is as follows:

$$V_x(x_1)=V_x(x_0)+\frac{18\eta(V_{f,x}(x_0)-V_x(x_0))}{d_p^2C_c\rho_p}\cdot dt$$

$$V_y(y_1)=V_y(y_0)+\frac{18\eta(V_{f,y}(y_0)-V_y(y_0))}{d_p^2C_c\rho_p}\cdot dt$$

$$x_1=V_x(x_0)\cdot dt$$

$$y_1=V_y(y_0)\cdot dt \tag{1}$$

where $V_{f,x}$,$V_{f,y}$ are the local flow velocity components, V_x, V_y the particle velocity components, ρ_p the particle's density, η the local fluid viscosity and C_c the local Cunningham slip correction factor. Particle location in the beginning is (x_0, y_0). The new location (x_1, y_1) after a short time dt can now be calculated using the two former equations and the velocity using the first two equations. After this, the starting location and the velocities are updated and the next time-step can be done.

Table 3
The number of control volumes used in the computed cases. *S*/*W*-ratio refers to different jet-to-plate simulation cases. *S* is jet-to-plate distance and *W* is the diameter of the nozzle orifice.

Case	Stage	No. of control volumes
ELPI	Extra	260,000
ELPI	1	260,000
ELPI	2	190,000
ELPI	3	440,000
ELPI	4	260,000
ELPI	5	403,000
ELPI	6	260,000
ELPI	7	115,000
ELPI	12	339,000
QCM	6	204,000
QCM	8	157,000
QCM	9	157,000
$S/W=\frac{1}{2}$		200,000
S/W=1		200,000
S/W=2		230,000
S/W=5		125,000
S/W=7		212,000
S/W=10		185,000

This will be repeated until the particle gets collected or exits the stage. Integration of the particle track through the high velocity impactor stage is a stiff problem. This is why the time-step size has to be adapted in order to solve the problem accurately and to keep the calculation time reasonable. The adaption was done by calculating two choices for the step-size and by choosing the smaller one. The limitations were that the particle was not allowed to travel or its velocity to change more than certain predetermined value during one time-step.

The collection efficiency of the impactor can be calculated from the particle track data when traces of different sized particles have been calculated. Approximately 20 particle tracks per particle size were calculated. The particles entered the nozzle from the nozzle inlet and were followed until they were impacted to the collection plate or survived to the outlet. It was thought that each particle represents a particle flux from a narrow ring shaped area centered at the starting location of the particle. If the particle impacted, the flux that it represents was collected from the flow and if it passed the stage, the flux of particles represented by the particle passed the impactor stage uncollected. From the particle starting location and penetration data the stage collection efficiency ψ as a function of the aerodynamic size of the particle can be calculated:

$$\psi(d_p)=\frac{\sum_i v_i A_i L_i}{\sum_i v_i A_i} \tag{2}$$

where A_i is the area of the nozzle represented by the ith particle, v_i the particle velocity normal to the nozzle inlet cross-section, L_i is zero if the ith particle was collected or one if it survived through the stage. The trajectories were calculated in the time averaged flow field and no stochastic tracking model was used. Stochastic models were not used because there is some evidence that they might not be accurate with high velocity flows. This can be seen from the article by Leduc et al. (2006) who tried to model the cutpoints of the ELPI impactor using the stochastic tracking options of the Fluent software but failed.

Aerodynamic focusing can cause particle enrichment in the axial region of the impactor jet as shown by Jurcik and Wang (1995). The results of Jurcik and Wang hold for low velocity atmospheric pressure impactors. At the nozzle inlet the flow field has a radial component that can cause aerodynamic focusing. However, in the case of LPI the effect is very small because only a small portion of the particle flux arrives in the nozzle from a direction normal to the axis. In addition, the particle Stokes number is typically very small: for a 30 nm particle entering the lowest impactor stage of ELPI it is approximately 0.04. Therefore, the particles were introduced evenly distributed at the nozzle inlet.

4. Results

4.1. Details of the flow fields

Fig. 1 presents contour plots and velocity vectors of the ELPI stage no. 1. From Fig. 1(a) it can be found that the maximum velocity in the axis of the jet is approximately 1.17 Mach. The area weighted average velocity at the jet outlet is approximately 280 m/s, which corresponds to the average velocity calculated by assuming an adiabatic flow through the nozzle which is of 285 m/s. Fig. 1(b) presents the velocity vectors. It shows that the jet decelerates and turns very rapidly near the collection plate, much closer than one jet radius.

Fig. 1(c) presents the static pressure contours. It shows that the pressure in the jet axis in the vicinity of the collection plate is very close to the upstream stagnation pressure before the nozzle. This corresponds to the experimental result presented by Flagan (1982) and Kauppinen, Hillamo, Ruuskanen, Hakkarainen, and Rouhiainen (1986). What the experimental results do not reveal, is that the static pressure varies significantly across the jet area near the collection plate. Static pressure is at the axis the upstream stagnation pressure and at the edge of the jet it has decreased to the value that corresponds the downstream pressure of the stage. Pressure profiles are similar for all stages of the ELPI, but the profile has a significant effect only on the impaction conditions of the low pressure stages, because with these stages the slip correction factor depends on the pressure. It was found in the simulations that the impaction of the particles did not start from the jet axis advancing toward the outer edge of the jet as the particle size was increased. Instead the impaction first took place closer to the outer edge of the jet than in the axis. As the particle size was increased it advanced toward the jet axis and the outer edge. This can be explained by the change in the slip correction factor. The slip correction factor is inversely proportional to the pressure for particles smaller than a few hundred nanometers in diameter. This observed phenomenon combined with the velocity profile of the jet is further discussed in Section 4.3.2

The modeling results of the temperature profile are presented in Fig. 1(d). It is interesting that the temperature drop can be significant and is reduced far below free freezing point of water. In this case, the temperature drops at the nozzle outlet to 235 K ($-38\,^{\circ}$C). For these conditions, it is possible that some particles can undergo a phase transformation.

In the turbulent flow modeling methods based on the time averaged versions of the N–S equations, the effects of the turbulence on the flow field are modeled via the turbulent viscosity μ_T. The time averaged equations have a similar form as the steady state N–S equations except that the molecular viscosity μ_L is replaced by the effective viscosity μ_{eff}, which is defined as $\mu_{eff}=\mu_L+\mu_T$. The idea behind this is that the turbulence enhances the momentum transfer in the flow field, and causes extra stresses to the fluid elements besides the molecular stresses. These extra stresses are modeled simply as an increased viscosity (μ_{eff}). It should be noticed that the turbulent viscosity is not constant but it changes with the location. Fig. 1(e) presents the contours of the turbulent viscosity ratio μ_T/μ_L. At the maximum it is only approximately 7%, meaning that turbulence has only a very slight effect on the time average flow field.

Another important aspect of the turbulence is the intensity of the velocity fluctuations. A modeling parameter that describes velocity fluctuations is the turbulence kinetic energy k. It can be shown, by assuming isotropic turbulence, that the root mean square of the velocity fluctuations can be related to the turbulence kinetic energy by the equation: $\overline{\nu'}=\sqrt{\frac{2}{3}k}$. The strength of the velocity fluctuations $\overline{\nu'}$ is usually described by the turbulence intensity which is defined as $T=\sqrt{\frac{2}{3}k/V_{ref}^2}$, where ν_{ref} is the important freestream velocity scale. The contours of the turbulent intensity for the first stage are presented in Fig. 1(f). The reference velocity used in the normalization is the maximum flow velocity in the jet. It shows that the maximum intensity value of approximately 1.7% is reached after the jet has started to spread in the radial direction above the collection plate. This indicates a low turbulence level and the absolute strength of the velocity fluctuations is in the order of 6 m/s.

4.2. *Collection efficiencies of the ELPI and the QCM impactors*

The simulated and experimentally determined collection efficiencies for the ELPI are presented in Fig. 2(a). The cutpoints, i.e. particle sizes corresponding to the 50% collection efficiency were interpolated from the simulated data. The cutpoints are collected in Table 4. The simulated collection efficiencies and fits for the QCM stages are shown in Fig. 2(b). In addition to the simulated cutpoints, experimentally determined cutpoints and differences between these two are presented in Table 4.

It can be seen that the simulated cutpoints are in a good agreement with the experimental results. The average difference between the simulated and experimental cutpoints is 11% and the maximum difference is 25%. This agreement is significantly better than in the previous study of ELPI impactor by Leduc et al. (2006). They simulated the collection efficiencies of ELPI using $k-\varepsilon$-turbulence model in combination with the standard particle tracking package of Fluent 6.2. With the first stage of ELPI the relative difference in the cutpoint was approximately 550% and for the stages 1–5 it was in the range of 100–600%. Accuracy of the simulations is also comparable to the study by Vinchurkar et al. (2009). They simulated the collection efficiencies of the Andersen cascade impactor with Fluent software. The Andersen impactor works in the atmospheric pressure and uses low jet velocities. This is in the flow range where the standard particle tracing and flow field solving features of Fluent should provide very good accuracy. The differences between simulations and experiments in their study were in the range of 0–10%.

The steepness of the simulated collection efficiency curves of the ELPI does not correspond to the experimental results. All of the experimental curves are less steep than the simulated curves. This is one of the central topics of this paper and will be discussed extensively in the next section.

4.3. *Factors affecting impactor resolution*

4.3.1. *Effect of turbulence*

Impactor resolution can be described by the steepness of the collection efficiency curve. The definition for the resolution parameter used in this study is

$$R=\frac{Stk_{0.5}}{Stk_{0.8}-Stk_{0.2}} \tag{3}$$

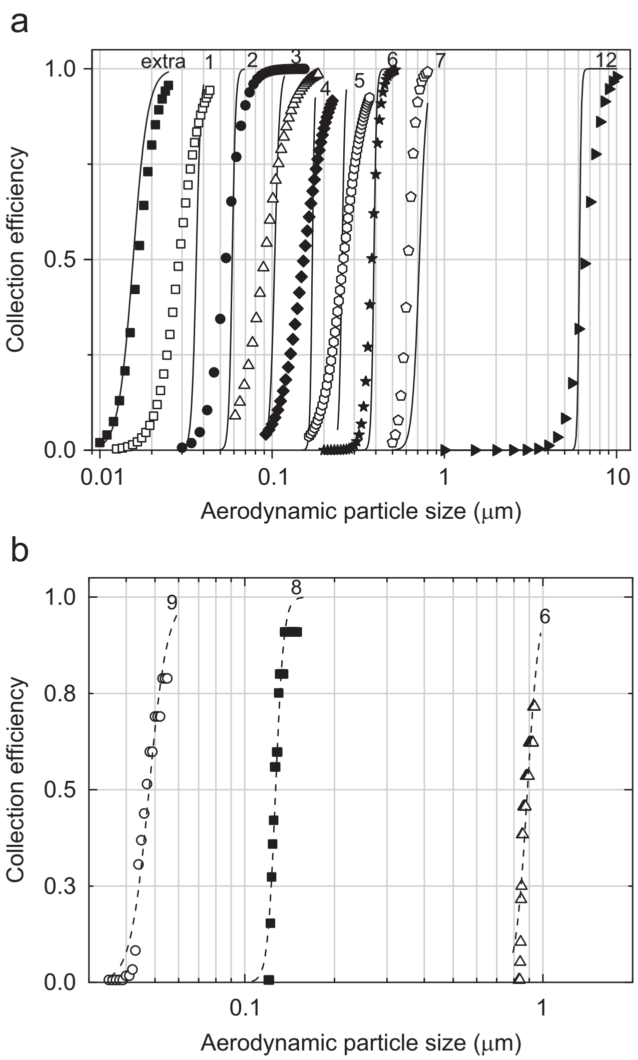

Fig. 2. Simulated and experimental collection efficiencies of the ELPI and the QCM impactors. In (a, ELPI) dots are the experimental results, and the solid lines are the simulation results. In (b, QCM) both the dots and the curves are the simulated collection efficiencies. Numbers in the figures correspond to the impactor stages.

Table 4
Simulated and experimental cutpoints of the ELPI and QCM impactors.

Stage	Experimental $d_{p,50}$ (nm)	Simulated $d_{p,50}$ (nm)	Diff. (%)
ELPI			
Extra	16,7	15	−10
1	29	36	25
2	54	59	8
3	90	103	14
4	152	171	13
5	260	255	−2
6	380	390	3
7	620	716	−13
12	6500	6080	7
QCM			
6	46	47,7	4
8	150	127	−15
9	930	888	−15

where *Stk*'s refer to the Stokes numbers corresponding to the collection efficiencies of 20%, 50% and 80%. Stokes number in the equation is calculated following the convention as follows:

$$Stk=\frac{\rho_p C_c V_j d_p^2}{9\mu W} \tag{4}$$

Here ρ_p is the particle density, C_c the slip correction factor, V_j the jet velocity, d_p the particle diameter, μ dynamic viscosity and W the jet diameter. The effects of the turbulence level and the jet-to-plate distance on the impactor resolution were investigated using the numerical results in combination with the experimental results. The effect of the turbulent velocity fluctuations (turbulent dispersion) cannot be directly seen from the simulated collection efficiencies, because the particle tracking was calculated using the time averaged flow field. What can be seen from the modeled flow fields, is the intensity of the velocity fluctuations. Besides the turbulence intensity, also other conditions in the flow field are different in the different ELPI stages. Figs. 3(a)–(c) present these dependencies. It can be seen that there is no direct connection between the number of nozzles, pressure or Mach number of the stage and the ratio between the modeled and experimental resolutions. Fig. 3(d) presents the ratio between the simulated and experimental resolutions and the average of turbulence intensity as a function of ELPI stage number. A clear correlation can be seen, the higher the turbulence level of the jet, the larger is the ratio between resolutions.

Fig. 4 shows the relation between the turbulence intensity and differently defined Reynolds numbers of the jet. It can be seen that the conventional jet Reynolds number does not correlate very well with the turbulence intensity calculated from the simulation results. The locally defined Reynolds number takes into account the spreading of the jet and the velocity in the core of the jet. The locally defined Reynolds number has a better correlation with the turbulence intensity. It can be deduced that the modeling method based on the time-average equations gives reliable results and can be used in the modeling of the operation of the low pressure impactor when the turbulence intensity of the jet is less than 1% or the locally defined Reynolds number of the jet is less than 1800. Another point that can be made from Fig. 3, is that when the turbulence level of the jet is increased, the impaction conditions in the time-average flow field tend to become more uniform and produce a steeper collection efficiency curve. In the experimental results this increase is not seen, because at the same time the turbulence level increases and deteriorates the resolution significantly.

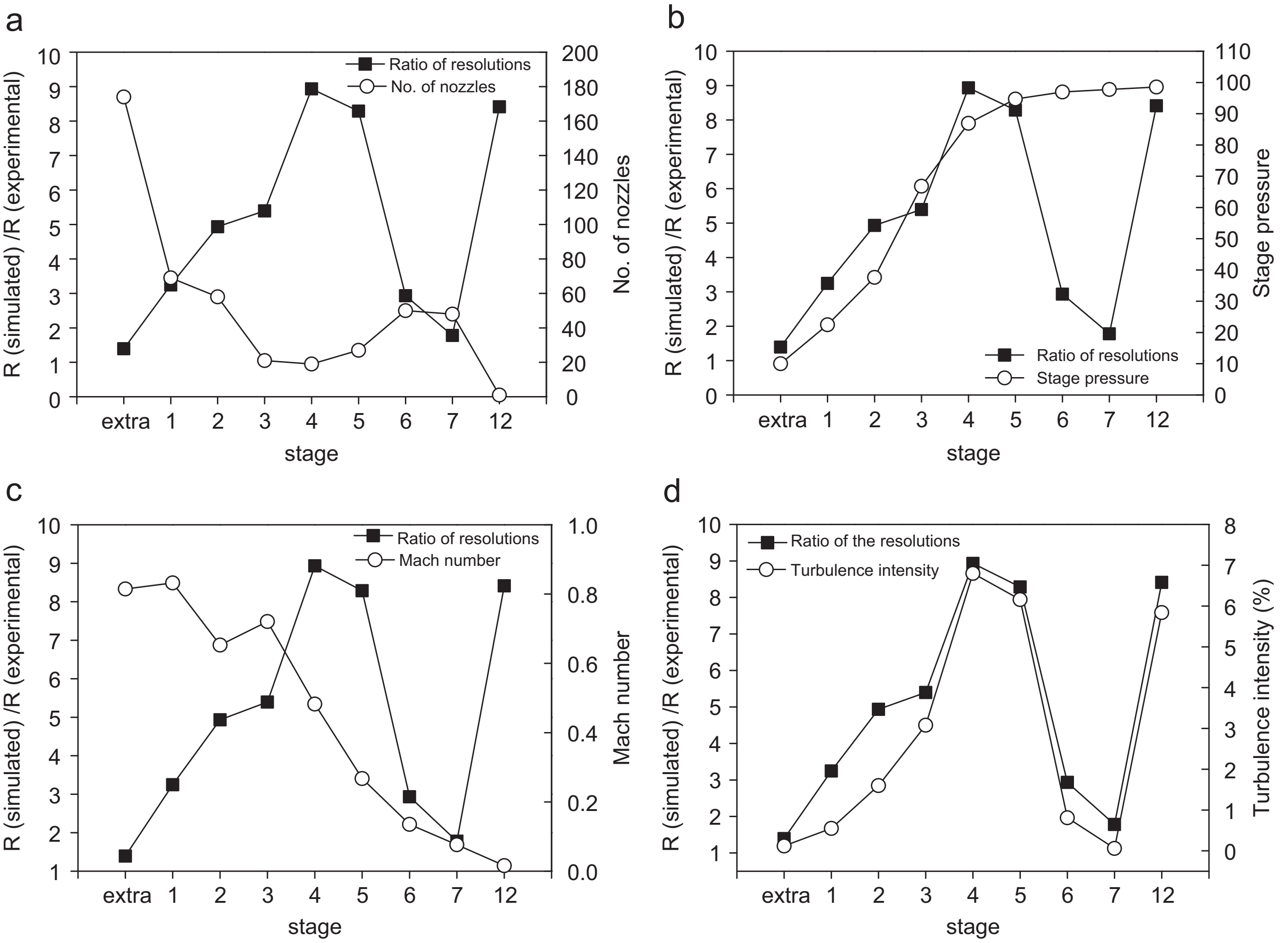

Fig. 3. Ratio between simulated and experimental resolutions of ELPI impactor plotted together with the different stage dependent parameters. (a) No. of nozzles. (b) Stage pressure. (c) Mach number based on the adiabatically calculated jet velocity. (d) Turbulence intensity value is a flux weighted average from the location where the jet has reached its maximum velocity.

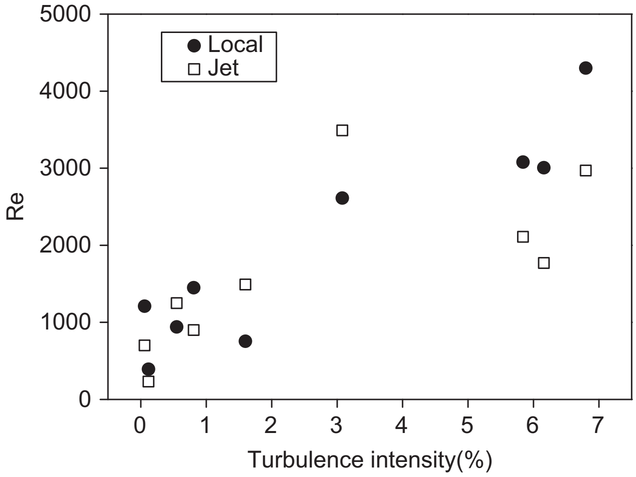

Fig. 4. The Reynolds number based on the local flow conditions and the Reynolds number based on jet diameter as a function of average turbulence intensity of the jet. The Local *Re* is defined using the density, velocity, viscosity on the jet axis before flow is turned by the collection plate, and the width of the jet is the diameter of the circle that encloses 90% of the total mass flow rate of the jet.

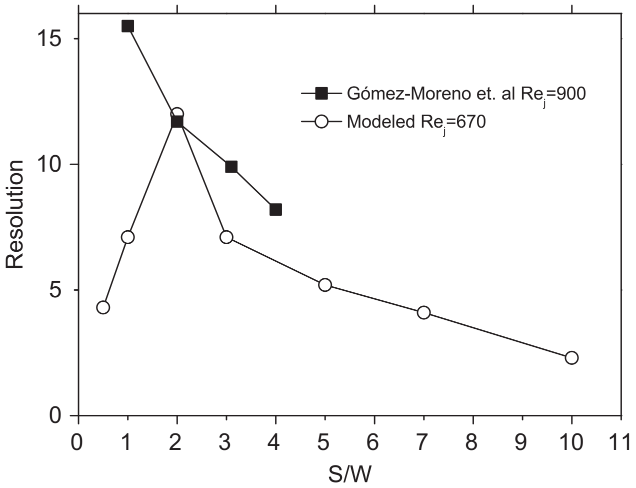

Fig. 5. The modeled resolution parameter as a function of impactor's *S*/*W*-ratio (diameter/jet-to-plate) and comparable experimental results by Gómez-Moreno et al. (2002). In the modeled case jet diameter, throat length and pressures were same as in the ELPI's first stage.

4.3.2. Effect of collection plate distance

If the turbulence level in the impactor jet is high, the results presented in the previous section suggest that the modeled resolution does not correspond to the real resolution because of the high turbulent dispersion. If the turbulence level is low, changes in the modeled and experimental resolution should correlate when the jet-to-plate distance is varied. In this study the collection efficiencies for seven different jet-to-plate distances were modeled. The jet diameter, throat length and pressures were the same as in the first stage of the ELPI. Fig. 5 shows the behavior of the modeled resolution parameter as a function of *S*/*W*-ratio of the impactor. The modeled resolution shows a clear peak at *S*/*W*=2. Although the resolution gets lower as the *S*/*W* increases, the modeled resolution in the range *S*/*W*=0.5…5 is quite good corresponding well to the generally accepted impactor design criteria. For comparison purposes, the experimental results by Gómez-Moreno, Rosell-Llompart, and Mora (2002) for a focused, single jet impactor are plotted in the same figure. Their results have a similar trend for larger *S*/*W* values: higher the *S*/*W* the lower the resolution. However, their results do not show any peak for the resolution. This could be mostly attributed to aerodynamical focusing they used. Strong aerodynamical focusing causes an increase in the resolution for all *S*/*W* ratios in the experimental curve. This means that if the focusing was removed from the experimental results, resolution could drop below the simulated curve. Focusing can also affect the peaking of the curve and it is possible that if more experimental points could be added of lower end of the curve, perhaps the peaking of the resolution could be seen.

A parameter that can be used to describe the impaction conditions locally in the impactor jet is the particle stopping distance (S_p) divided by the distance particle has to travel for the impaction to occur (S_i). For the particle sizes relevant to the low pressure stages of this study, the crucial parameters affecting the stopping distance are the velocity before the flow turns and the slip correction factor. The local impaction conditions in the jet cross-section can be characterized by the impaction parameter (I) which is proportional to the ratio S_p/S_i:

$$\frac{S_p}{S_i} \propto I = \frac{V_0}{PS_i} \tag{5}$$

Here V_0 is the velocity of the particle before the flow turns (based on the simulations values for the V_0 are taken from the axial velocity profile from a location where the jet has reached its maximum velocity), P is the pressure approximately 20 μm above the collection plate (particles lose their axial velocity under the drag force that is calculated in this pressure) and S_i is the distance from the collection plate when the axial flow velocity has decreased to zero. V_0 and P profiles were extracted from the simulation results with Fluent postprocessing tools. S_i profile was interpolated from the simulation results as the distance where the axial flow velocity decreases below 1 m/s. Zero velocity cannot be chosen as the limit, because theoretically this point is infinitely close to the collection plate at the stagnation point. The larger the value of the impaction parameter, the more easily impaction occurs. Fig. 6 presents the normalized value of the impaction parameter as a function of a distance from the axis of the jet for different S/W-ratios. The impaction parameter has been normalized against the value of the impaction parameter at the center of the jet. It can be seen that there are large variations in the impaction conditions if the jet-to-plate distance is very small or very large. Thus, particles smaller than the cut diameter get collected at locations with a high I (impaction parameter) value, whereas particles larger than the cut diameter do not get collected at locations with a low I value. This decreases the steepness of the collection curve of the impactor stage. Fig. 6 also supports the observation that with increasing particle size the impaction of particles does not necessarily start from the center of the jet but instead from boundary areas. This occurs with S/W-ratios less than 3 when the impaction parameter has a higher value at the outer edge of the jet than at the center.

Based on the impaction parameter data in Fig. 6 and the axial velocity profile in the jet, the distribution of the impaction parameter I can be calculated. The distribution describes the portion of the total particle flux that belongs to a certain impaction parameter interval ($\Delta f/\Delta I$). Fig. 7 presents the impaction parameter distributions for different S/W-ratios.

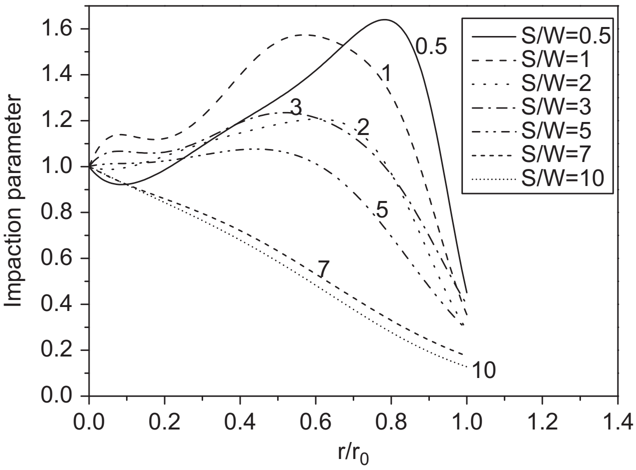

Fig. 6. Impaction parameter as a function of a radial position from the jet axis. Impaction parameter has been normalized with its value at the center of the jet. The normalization factor r_0 is the nozzle's diameter.

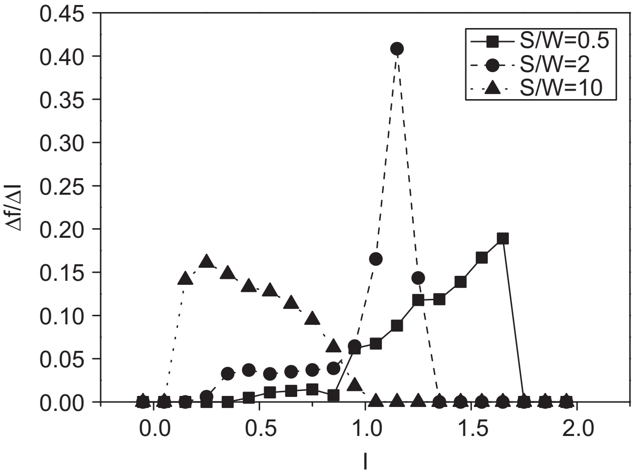

Fig. 7. Distribution of the impaction parameter for different collection plate distances.

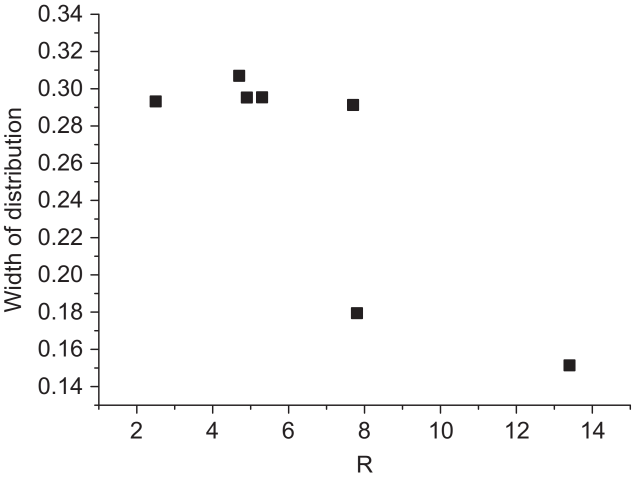

Fig. 8. Width of the modeled impaction parameter distribution as a function of the modeled resolution parameter. The width is the impaction parameter interval where the value of the cumulative distribution changes from 30% to 70%.

An ideal impactor stage would have a peak only in one class providing thoroughly homogenous impaction conditions in the jet area. In this case, the particles would be classified exactly in two different size fractions. But as the figure shows, a real impactor has a wider impaction parameter distribution. The narrower the distribution is, the better the resolution of the impactor(steepness of the collection efficiency curve) is. With small collection plate distances, the impaction parameter increases in the edges of the jet. For large collection plate distances the behavior is opposite, the impaction parameter has the lowest value in the edge of the jet. This also indicates, that when the particle size is increased and the collection plate distance is small, impaction occurs first at the edges of the jet. If the collection plate distance is large, impaction begins in an opposite way proceeding from the center to the edges. Even though the number of data points is limited, the same can be seen in Fig. 8. Highest resolutions correspond to the narrowest impaction parameter distributions.

5. Conclusions

The aim of this study was to introduce and validate a CFD simulation approach that correctly describes the operation of a low pressure impactor, and to apply it to study the parameters that affect the collection efficiency of the low pressure impactor. A commercial CFD code was used to solve the flow field inside the impactor nozzle. Particle tracks were calculated and the collection efficiency of the impactor was calculated from the particle tracks. The model was validated against the experimental results of the ELPI and the QCM impactor stages. It was able to predict the cutpoints of the studied impactors within 11% on average. From the modeled pressure fields it was seen that the pressure at the center of the impaction plate corresponds to the upstream stagnation pressure of the impactor. This result also corresponds to the experimental results reported in the literature.

The model was used to study the effects of turbulence and collection plate distance on the impactor resolution. It was found that if the local Reynolds number in the jet exceeds approximately 1800 or the turbulence intensity is over 2%, equations based on the time-averaged N–S equations cannot be used in modeling the operation of the low pressure impactor. The effect of turbulent dispersion has to be taken into account because it starts to be the dominant phenomenon that defines the resolution beyond this limit. The effect of the collection plate distance on the resolution was investigated using a case where the local Reynolds number is approximately 1500. It was found that there is a maximum in the resolution when the ratio of the jet-to-plate distance to the jet diameter (S/W) is 2. The resolution remains reasonably good when the S/W-ratio is between 0.5 and 5. The factor that lowers the resolution with too low or too high collection plate distances was found to be related to the increasing variations in the impaction conditions at the jet area. The uniformity of the impaction conditions was studied by investigating the variations in the impaction parameter $V_0/(S_iP)$, defined as the local velocity in the jet divided by the product of the pressure above the collection plate and distance from the collection plate where the velocity component of flow normal to collection plate has decreased to 0. The width of the impaction parameter distribution is correlated with the modeled resolution of the impactor.

In the future, the time-averaged modeling approach can be used as a tool to study for example particle losses and bounce inside the low pressure impactor. The model can also be potentially used to improve impactor performance and resolution and to develop new impactors. The resolution could be optimized, for example, by shaping the collection plate so that it produces even impaction conditions across the jet area.

References

Asgharian, B., Zhang, L., & Fang, C. (1997). Theoretical calculations of the collection efficiency of spherical particles and fibers in an impactor. *Journal of Aerosol Science*, *28*, 277–287.

Bartosiewicz, Y., Aidoun, Z., Desevaux, P., & Mercadier, Y. (2005). Numerical and experimental investigations on supersonic ejectors. *International Journal of Heat and Fluid Flow*, *26*, 56–70.

Berner, A. (1972). Praktische erfahrungen mit einem 20-stufen-impactor. *Staub Reinhaltung Der Luft*, *32*, 315.

Biswas, P., & Flagan, R. C. (1984). High-velocity inertial impactors. *Environmental Science & Technology*, *18*, 611–616.

Flagan, R. C. (1982). Compressible flow inertial impactors. *Journal of Colloid and Interface Science*, *87*, 291–299.

Gómez-Moreno, F., Rosell-Llompart, J., & Mora, J. F. d. l. (2002). Turbulence transition in impactor jets and its effects on impactor resolution. *Journal of Aerosol Science*, *33*, 459–476.

Hering, S. V. (1987). Calibration of the QCM impactor for stratospheric sampling. *Aerosol Science and Technology*, *7*, 257–274.

Hering, S. V., Flagan, R. C., & Friedlander, S. K. (1978). Design and evaluation of new low-pressure impactor. 1. *Environmental Science & Technology*, *12*, 667–673.

Hering, S. V., Friedlander, S. K., Collins, J. J., & Richards, L. W. (1979). Design and evaluation of new low-pressure impactor. 2. *Environmental Science & Technology*, *13*, 184–188.

Hillamo, R. E., & Kauppinen, E. I. (1991). On the performance of the berner low pressure impactor. *Aerosol Science and Technology*, *14*, 33–47.

Jurcik, B., & Wang, H. (1995). On the shape of impactor efficiency curves. *Journal of Aerosol Science*, *26*, 1139–1147.

Kauppinen, E., Hillamo, R., Ruuskanen, J., Hakkarainen, T., & Rouhiainen, P. (1986). Theoretical and experimental study of particle collection characteristics of high-velocity multijet cascade impactors. *Journal of Aerosol Science*, *17*, 506–510.

Keskinen, J., Pietarinen, K., & Lehtimäki, M. (1992). Electrical low pressure impactor. *Journal of Aerosol Science*, *23*, 353–360.

Leduc, S., Fredriksson, C., & Hermansson, R. (2006). Particle-tracking option in fluent validated by simulation of a low-pressure impactor. *Advanced Powder Technology*, *17*, 99–111.

Marjamäki, M. (2003). *Electrical low pressure impactor: Modifications and particle collection characteristics*. Ph.D. thesis, Tampere University of Technology.

Marple, V., Liu, B., & Whitby, K. (1974). On the flow fields of inertial impactors. *ASME Journal of Fluids Engineering*, *96*, 394.

Marple, V. A., & Liu, B. Y. H. (1974). Characteristics of laminar jet impactors. *Environmental Science & Technology*, *8*, 648–654.

Menter, F. R. (1994). Two-equation eddy-viscosity turbulence models for engineering applications. *AIAA Journal*, *32*, 1598–1605.

Rader, D., & Marple, V. (1985). Effects of ultra-Stokesian drag and particle interception on impaction characteristics. *Journal of Aerosol Science*, *4*, 141–156.

Swanson, P., Muzzio, F., Annapragada, A., & Adjei, A. (1996). Numerical analysis of motion and deposition of particles in cascade impactors. *International Journal of Pharmaceutics*, *142*, 33–51.

Vanderpool, R., Lundgren, D., & Kerch, P. (1990). Design and calibration of an in-stack low-pressure impactor. *Aerosol Science and Technology*, *12*, 215–224.

Vinchurkar, S., Longest, P. W., & Peart, J. (2009). Cfd simulations of the andersen cascade impactor: model development and effects of aerosol charge. *Journal of Aerosol Science*, *40*, 807–822.

Yli-Ojanperä, J., Kannosto, J., Marjamäki, M., & Keskinen, J. (2010). Improving the nanoparticle resolution of the ELPI. *Aerosol and Air Quality Research*, *10*, 360–366.

Paper 2

Arffman, A. and Yli-Ojanperä, J. and Keskinen, J., The influence of nozzle throat length on the resolution of a low pressure impactor – An experimental and numerical study, *Journal of Aerosol Science*, 53, 76–84, 2012.

Journal of Aerosol Science 53 (2012) 76–84

Contents lists available at SciVerse ScienceDirect

Journal of Aerosol Science

journal homepage: www.elsevier.com/locate/jaerosci

The influence of nozzle throat length on the resolution of a low pressure impactor—An experimental and numerical study

A. Arffman*, J. Yli-Ojanperä, J. Keskinen

Tampere University of Technology, Department of Physics, Aerosol Physics Laboratory, P.O. Box 692, FI-33101 Tampere, Finland

ARTICLE INFO

Article history:
Received 29 February 2012
Received in revised form
4 June 2012
Accepted 5 June 2012
Available online 13 June 2012

Keywords:
Low Pressure Impactor
Collection efficiency
Resolution
Impaction velocity
Cutpoint
Numerical simulation

ABSTRACT

This study investigates the effect of the nozzle throat length on the resolution of the low pressure impactor (LPI). Two basic nozzle geometries, rectangular slit and round nozzle with 25 nm cutpoint were investigated both experimentally and by numerical simulation. A new impactor stage with variable nozzle throat length and jet-to-plate distance was designed, built and tested. The impactor was calibrated at four different configurations with monodisperse dioctyl sebacate (DOS) aerosol. A very good agreement between the simulated and the experimental resolutions and cutpoints were found. The main conclusions are that (a) the length of the nozzle is a crucial parameter affecting the resolution and (b) it is possible to achieve a better resolution with a rectangular slit type impactor than with a round nozzle type LPI. The best observed resolution was achieved with the slit type LPI with a nozzle throat length to width ratio of only 0.33. Compared to similar cutpoint impactor stages of commercially available LPIs, the resolution of the new stage is by far the highest.

1. Introduction

Impactors have been used since the end of the 19th century in aerosol science to classify particles according to their size. One widely used method is to use impactor stages in a cascade configuration to measure the size distribution of the particles. In cascade impactors, several impactor stages with varying cut points are placed in series. To achieve lower cutpoints, low pressure impactors (LPI) have been introduced. In cascade low pressure impactors the pressure is reduced either by having a separate pressure reducing stage (e.g. Hering et al., 1978, 1979) or by gradually reducing the pressures by using high jet velocities (e.g. Berner, 1972; Vanderpool et al., 1990). Besides the size classification of particles, LPIs have been employed in some less conventional applications such as studying the particle properties (Friedlander, 1999; Virtanen et al., 2010).

Resolution of the single impactor stage is defined as the steepness of the collection efficiency curve. Having a high resolution for a single impactor stage would allow the cutpoints of individual stages to be brought closer to each other without significant overlap in the kernel functions. This way more channels can be added to the same size range in the distribution measurement. In addition, this gives opportunity to control the impaction conditions of the particles more closely. For example, the impaction velocities of the particles inside an LPI stage will be more uniform. The resolution of an impactor stage is affected by many parameters such as geometry and flow conditions.

---

* Corresponding author.
E-mail addresses: anssi.arffman@tut.fi (A. Arffman), jaakko.yli-ojanpera@tut.fi (J. Yli-Ojanperä), jorma.keskinen@tut.fi (J. Keskinen).

0021-8502/$ - see front matter © 2012 Elsevier Ltd. All rights reserved.
http://dx.doi.org/10.1016/j.jaerosci.2012.06.002

The first numerical studies where the steepness of the collection efficiency has been studied are Marple & Liu (1974) and Marple et al. (1974). They investigated the effect of geometry and Reynolds number on the impactor resolution. Their studies showed that with decreasing Reynolds number the resolution may be deteriorated and shortening the throat length may have the opposite effect. However, Marple's studies have been made during 70's and therefore the size of the computation grids were quite limited. Jurcik & Wang (1995) studied the effect of nozzle entrance geometry on the resolution of the impactor. They found out that the straight nozzle geometry focuses particles towards the axis of round nozzle, and this may cause the "tail" of the collection efficiency curve. Like Marple et al. showed earlier, also Jurcik & Wang observed that the resolution decreases when the Reynolds number is decreased below 100. All these studies assumed constant fluid properties for the flow. Supersonic and hypersonic impactors have been studied by numerical methods in Abouali & Ahmadi (2005), Abouali et al. (2011) and Zare et al. (2007). Their results show that the resolution of these extremely large pressure ratio impactors (upstream/downstream pressure ratio is in the order of magnitude 100) seems to be lower than for example the lowest cutpoint stages of well known Berner LPI (Hillamo & Kauppinen, 1991). Result implies that the resolution of the supersonic impactor is about the same as for subsonic LPI.

Marple & Liu (1975) made analysis on how to reach the ideal impactor collection efficiency, i.e. impactor that has a step functional collection efficiency curve. The idea was that if the impactor flow field solution is dependent only on the normal distance from the collection plate and the velocity distribution of particles at the nozzle exit plane is uniform, the collection efficiency curve shape is ideal. Conclusion of the paper was that with small nozzle Reynolds numbers the collection efficiency curve steepness decreases because of boundary layer development at the nozzle walls. Developed boundary layer causes particles to have an uneven velocity profile at the nozzle exit plane. Their analysis was based on numerical simulation results of LPI by Marple & Liu (1974). De la Mora et al. (1990) investigated experimentally the operation of the transonic LPI at moderate Reynolds number. They chose the investigated nozzle geometry in order to prevent the deterioration of resolution by the possible boundary layer development. This was accomplished by using a wide nozzle compared to its length. The ratio of the nozzle length (T) to the diameter (W) was 0.15. The nozzle consisted of a converging section followed by a straight nozzle with a total length of 0.554 mm. Gómez-Moreno et al. (2002) studied the turbulent transition in the impactor jet. This was performed by observing the resolution of the LPI as a function of the Reynolds number. Results showed that when the jet-to-plate distance is two times greater than the diameter of the nozzle, the flow experiences the laminar to turbulent transition at Reynolds number in an order of 1000. When the transition occurs also the resolution is deteriorated significantly. Also Arffman et al. (2011) investigated the effect of turbulence on LPI resolution by numerical simulations. They found out that when the Reynolds number is less than 1500 the turbulence does not have strong deteriorating effect on the resolution of LPI. In the applied flow range the simulated and measured resolutions had a good correlation, and therefore the simulation approach they presented can be used in studying the resolution at low Reynolds numbers.

The focus of this study is on improving the resolution of a single LPI stage by experiments and numerical simulations. Idea on how to improve the resolution of LPI is inspired by the previous studies of Marple et al. (1974) and De la Mora et al. (1990) and also by the considerations of steady impaction conditions presented in the previous study of authors (Arffman et al., 2011). We investigate the effect of the ratio of nozzle throat length (T) to the width of the nozzle (W, the width or the diameter of the nozzle corresponding round and slit nozzles) on the collection efficiency curve steepness by numerically and experimentally. Also the resolutions produced by rectangular slit and round nozzle LPIs are compared. Simulations are made using methods presented in Arffman et al. (2011). Resolution is studied experimentally by building a new LPI stage with exchangeable nozzle length and shape. Collection efficiency of the stage is measured using monodisperse vacuum oil particles.

2. Simulations

Effect of different geometrical parameters on the shape of impactor collection efficiency curve were simulated using methods presented in the preceding paper by Arffman et al. (2011). Briefly, the flow field was first simulated using ANSYS Fluent 12.1 software, and the particle tracking and collection efficiency computation was carried out with a separate Matlab script. All simulations were made in two dimensions (axi- and planesymmetric equations) with compressible flow effects included. Meshes were rectangular and included roughly 50,000–100,00 computation cells. Boundary layer was created for the collection plate and the mesh was densed inside the nozzle and at outlet of the nozzle. Flow was modeled as a turbulent flow using the SST-$k-\omega$-turbulence transfer model and the advanced wall treatment of ANSYS Fluent. Although it did not have much practical effect in the simulations, because the Reynolds numbers were in order of few hundred, and the turbulent viscosity values were negligible compared the dynamic viscosity of the gas. Second order upstream discretization scheme was used in the discretizations of the flow equations. Boundary conditions were fixed pressures at the inlet and outlet boundaries of the domain. These are listed in the Table 1. Particles were released from the nozzle inlet plane and the aerodynamic focusing effect at the inflow was not included in the simulations. The focusing effect drives particles towards the axis of the nozzle and tends to steepen the collection efficiency curve. On the other hand, when the particles are packed in a confined space the Coulombic repulsion and the diffusion spread the particles radially, that inhibits the focusing effect.

It has been pointed out in previously (Arffman et al., 2011) that at least with the nozzle counts of ELPI impactor the effect of the nozzle count on the accuracy of simulation is very small. For example, the 17 nm cutpoint stage of ELPI has

Table 1
Critical dimensions and parameters of the simulated impactor stages. First column shows the type of the nozzle and T is the nozzle throat length, W the characteristic width, S the jet-to-plate distance, p_d the downstream stagnation pressure, and p_u the upstream stagnation pressure.

Nozzle type	T (mm)	W (mm)	S (mm)	T/W	S/W	p_d (mbar)	p_u (mbar)	Difference (mbar)
Round	0.1	0.6	1	0.166	1.66	29.8	39.2	9.4
Round	1	0.6	1	1.6	1.66	30	41	11
Slit	0.1	0.3	0.5	0.33	1.66	30.2	39.6	9.4
Slit	1	0.3	0.5	3.3	1.66	29.5	40	10.5

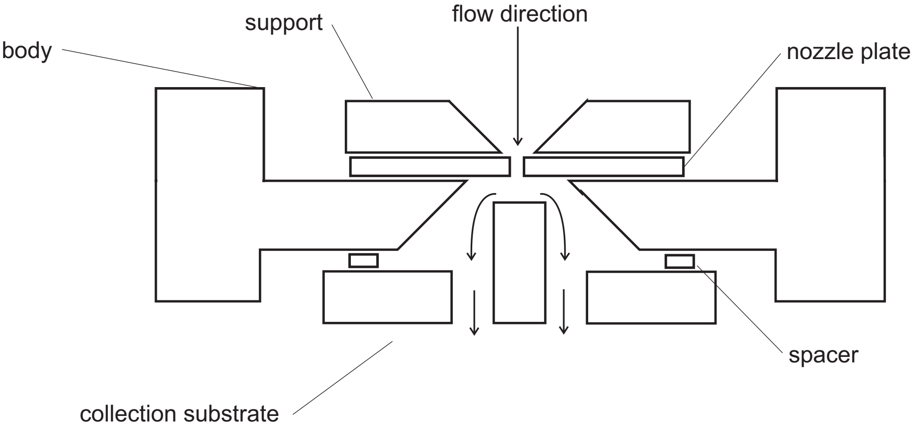

Fig. 1. Schematic figure of the stage cross section.

174 nozzles and the simulated collection efficiency is the most accurately predicted one of all. Slit nozzle impactors usually use only single nozzle since the flow rate can be adjusted by changing the length of the slit. Studied LPIs operated in the Reynolds number region ($Re_j < 500$ for all cases) where the simulation method should provide the resolution and cutpoints correctly as shown in the Arffman et al. (2011).

Initially, the collection efficiencies of a few LPI stages with different throat lengths, jet-to-plate distances and pressure ratios, were simulated. It appeared that the T/W -ratio could be an important parameter. Therefore, the simulations focused on studying how the T/W -ratio affect the resolution of the impactor. Two different throat lengths for both slit and round nozzle stages were simulated. The cases were chosen so that the effect would be clearly seen in the results. The slit nozzle was originally included in the study because it can be made very narrow in order to reach a low cutpoint. However, it was seen that it also offers other advantages compared to the round nozzle.

Table 1 shows the critical dimensions, their ratios and other stage parameters of the simulated cases. Length of the slits was 20 mm. Diameter of the round nozzle was larger than the slit width for two separate reasons: larger holes were easier for the machine in the relatively thick 1 mm steel plate, and because the critical Stokes number of the round nozzle is smaller than the critical Stokes number of the rectangular slit nozzle. The difference in the characteristic widths balances the situation so that the cutpoints of the round and slit nozzles are nearly the same (when upstream and downstream pressures are kept same). Jet-to-plate distance is doubled for the round nozzle in order to keep the S/W ratio constant. This way all four cases are kept as comparable as possible to each other in order to see the differences caused by different nozzle shape and throat length.

3. Experiments

Based on the simulation results a new impactor stage construction was designed that could fulfill the dimension requirements determined by simulations. A schematic figure of the stage is shown in Fig. 1. The stage was designed so that nozzles were machined on a separate plate. This is an unconventional way to do it as usually the nozzles are drilled to the upper part of the stage and the collection plate forms the lower part (e.g. ELPI and Andersen cascade impactors). This allowed us to change the nozzle dimensions by replacing the nozzle plate. Jet-to-plate distance (S) was also simple to vary by replacing the spacer between the collection plate and the body of the stage. Two screws were bolted through the nozzle supporting plate, body, and collection plate to keep all parts together. Calibration was performed using the electrical method presented by Keskinen et al. (1999). Because of the employed electrical method a possibility to measure the electric current separately from the collection plate and from the body of the stage was also prepared. This was enabled by embedding a thin insulating layer under spacer and replacing the metal screws by nylon version.

The new stage was made to fit in the body of Electrical Low Pressure Impactor unit (ELPI, Keskinen et al., 1992). This allowed the use of electrometers of ELPI to measure the electric currents from the impactor stage and from filter assembled after the stage. The calibration setup consisted of an evaporation–condensation type DOS particle generator to produce an initial particle size distribution. A Scanning Mobility Particle Sizer (SMPS, Wang & Flagan (1990)) was used for measuring the initial size distribution. After that, the DMA of the SMPS was coupled to select monodisperse particles from the initial aerosol. The initial size distributions had a GMD of approximately 25 nm and a GSD od approximately 1.4. The pressure before the stage was reduced from atmospheric pressure to 40 mbar using a critical orifice and a control valve. Upstream and downstream pressures were measured using MKS Instruments PDR-C-1C electrical pressure sensor, designed for measuring pressures below 100 mbar. The impactor collection plate surface was pure machined aluminium. No grease or other coating materials were used because DOS particles were not expected to bounce.

4. Results

Below, the simulated and experimental collection efficiencies for different nozzle throat lengths are shown first. After this the results will be explained in detail with arguments based on the nozzle flow fields. The effect of multiple charge correction as presented by Hillamo & Kauppinen (1991) was tested but the effect in this particle size range was negligible (this is shown later in the paper). Therefore, the experimental data are shown without this correction.

4.1. Resolutions

Figs. 2 and 3 show the collection efficiencies of the slit and the round nozzle impactors for different throat lengths. Experimental results are plotted with dots and the corresponding simulation result with similarly colored solid line. Difference between the measured and simulated cutpoints is 15% and in resolutions 12% in maximum. This is a satisfying accuracy since we estimated that the expected uncertainty in the measured cutpoints is about ±1 nm. In comparison, Leduc et al. (2006) simulated the cutpoints of ELPI impactor with Fluent 6.0 software. The difference between the simulated and the experimental cutpoints was in the range of 170%–550% for stages 1–3 (these are low pressure stages

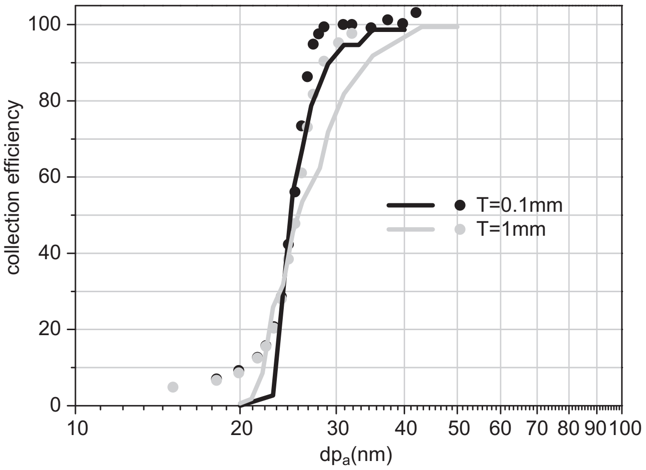

Fig. 2. Simulated (solid lines) and experimental (dots) collection efficiency of the slit impactor for different throat lengths.

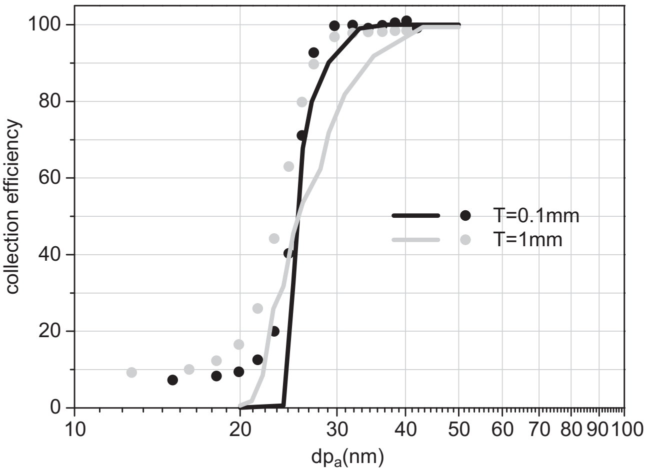

Fig. 3. Simulated (solid lines) and experimental (dots) collection efficiency of the round nozzle impactor for different throat lengths.

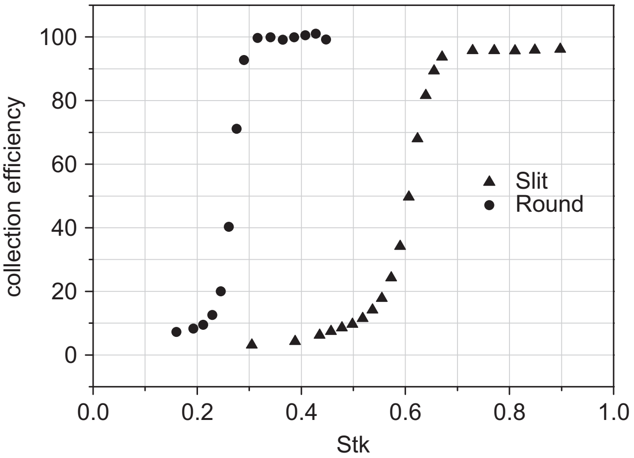

Fig. 4. Measured collection efficiencies of the slit and the round nozzle stages as a function of Stokes number with $T=0.1$ mm.

Table 2
Simulated and measured cutpoints and resolutions of the stages. Resolution is defined as ratio the ratio of the particle sizes corresponding to 80% and 20% collection efficiencies.

Nozzle type	T (mm)	Cutpoint simulated (nm)	Measured (nm)	Difference (%)	Resolution (dp_{80}/dp_{20}) simulated	Measured	Difference (%)
Round	1	26.6	23.2	14.6	1.39	1.28	8.6
Round	0.1	26.2	24.5	6.9	1.14	1.16	−1.7
Slit	1	28.3	25.1	12.7	1.33	1.19	11.7
Slit	0.1	25.6	25.1	1.9	1.17	1.15	1.7

with the cutpoints of 29 nm–92 nm). The simulated curves are little less steep, but the trend is same in the simulated and the experimental results. Shorter nozzle throat length produces better resolution. There is also difference between the resolutions of the slit and the round nozzle. The slit nozzle offers higher resolution and the efficiency drops to a lower level in the beginning of the curve. Fig. 4 shows the collection efficiency as a function of the Stokes number. The Stokes number corresponding 50% collection efficiency is 0.27 for round nozzle and 0.6 for the slit nozzle.

Table 2 shows the experimental and simulation values for the cutpoints and resolution parameter of the four stages. The resolution parameter is defined as the ratio of the particle sizes corresponding to 80% and 20% collection efficiencies. A smaller value means higher resolution. For both round and slit nozzles, the shorter 0.1 mm nozzles produce higher resolution. The short (0.1 mm) slit nozzle has the highest resolution. Table 3 shows that it is also highest when compared to the resolution of several commercially available LPI stages of approximately the same cutpoint diameter.

Fig. 5 shows the experimentally determined collection efficiency for the short (0.1 mm) slit nozzle stage by two different electrical current measurement setups. The open dot curve is obtained using the current measured from the whole stage. The black curve is obtained by using current measured only from the collection plate and triangles show the multiple charge corrected version of the same curve. The resolutions are practically the same, but when the current is measured from the collection plate the "tail" at the lower end of collection efficiency falls to a significantly lower level, approximately 2% at 10 nm. This demonstrates that particle collection by diffusion and by Coulombic (image charge) forces has a minor effect on the classification even when the particle size is only 10 nm. This applies for the studied slit nozzle stage, but the situation may be different with the round nozzle LPI. The internal wall losses, shown with crosses, were obtained by separately measuring the currents to the collection plate and the stage walls. The wall losses show that the particles smaller than the cutpoint diameter are mostly lost to the stage and nozzle walls and not to the collection plate. Fig. 5 also points out that the measurement is reproducible with an accuracy that is quite normal for the LPI measurements.

4.2. Flow field of the nozzles

The preceding experimental results showed that the length of nozzle throat is a critical parameter affecting the resolution. Fig. 6(a) and (b) presents the simulated axial velocity profiles at the nozzle exit plane for both the slit and round nozzle stages. The velocity profiles are plotted across the nozzle, with the center of the nozzle at the origin. The profiles show that the flow profile is very close to plug flow when the nozzle throat length is small compared to the width. This means that if particles follow the flow velocity in the nozzle, they have nearly uniform velocities before the flow decelerates. The uniform velocity profile therefore leads to uniform stopping distance conditions in the jet and thus increases the resolution.

Table 3
Resolutions operation parameters of different LPI stages. MOUDI (Marple et al., 1991), University of Washington Mark 10 (Vanderpool et al., 1990), Berner 25 (Štefancová et al., 2011), ELPI stage 1 (Keskinen et al., 1992), ELPI extra stage (Yli-Ojanperä et al., 2010), Hypersonic impactor ?, and slit type LPI presented in this article. Resolution is defined as ratio the ratio of the particle sizes corresponding to 80% and 20% collection efficiencies.

Impactor	Moudi	UW Mark 10	Berner 25/0.018	ELPI	ELPI	Slit	Hypersonic
Stage number	10	10	1	1	Extra	–	–
Cutpoint	56	46	25.2	29	17	24.7	9.9
Pressure ratio	0.53	0.81	0.42	0.44	0.43	0.75	0.0025
Resolution	1.77	1.55	1.21	1.44	1.44	1.15	1.27

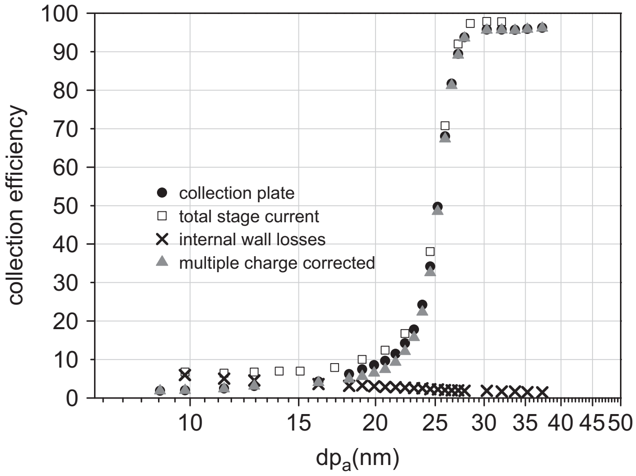

Fig. 5. Experimentally determined collection efficiencies of the slit impactor with two different current measurement setups and multiple charge corrected curve. Crosses show the internal wall losses, which include the stage upper parts and the nozzle walls.

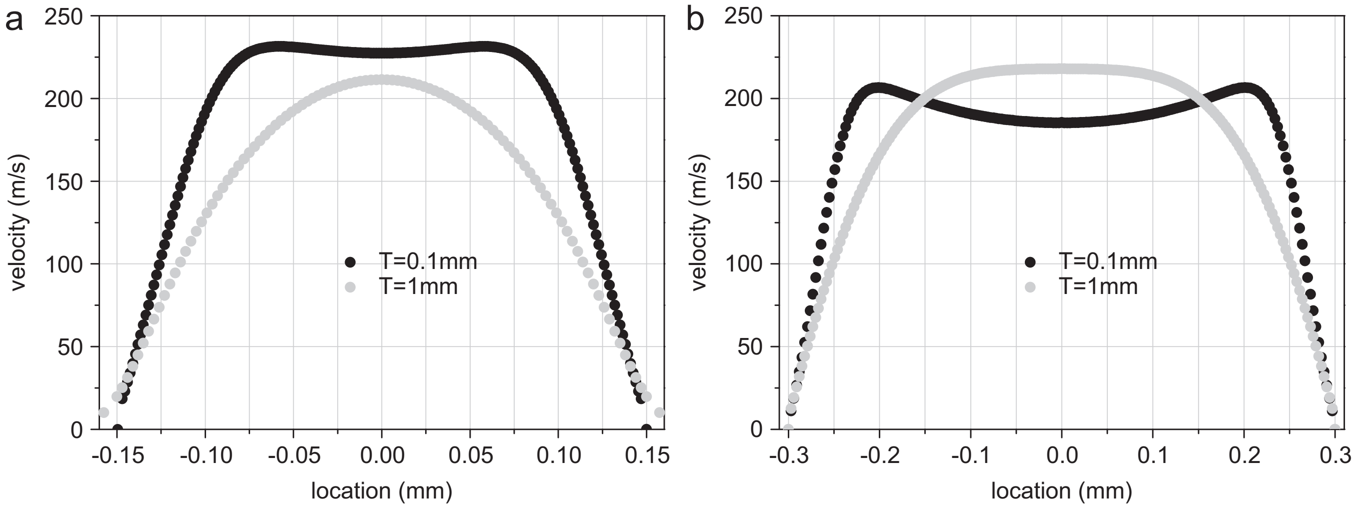

Fig. 6. Simulated velocity profiles at the nozzle exit plane across the jet. Center of the nozzle is located at the origin. Results for two throat lengths are shown. (a) Slit nozzle. (b) Round nozzle.

The velocity profile at the exit plane of a short round nozzle has a shape where the velocity has a maximum value near the edge of the jet. This is emphasized especially in the case of round jet (Fig. 6(b)). At first this may seem like a counter-intuitive result, but can be explained with the aid of pressure and velocity contours shown in Fig. 7(a) and (b). Fig. 7(a) presents the pressure contours in the cross section of the round nozzle, showing that the pressure decreases more rapidly at the edges of the nozzle than in the center. When the pressure decreases the velocity increases, as shown in Fig. 7(b).

The experimental collection efficiency results showed hat the slit nozzle offers better resolution than the round nozzle. Fig. 8 presents how the particle flux distributes across the jet in the cases of the slit and the round nozzle. In the slit nozzle, particles distribute rather uniformly across the jet, whereas in the round nozzle the largest portion of the particles pass through the edge areas. This combined with the jet exit plane velocity profiles means that in the slit a large portion of the particles flow through a uniform velocity area. In the round nozzle a large fraction of the particles pass through the edge

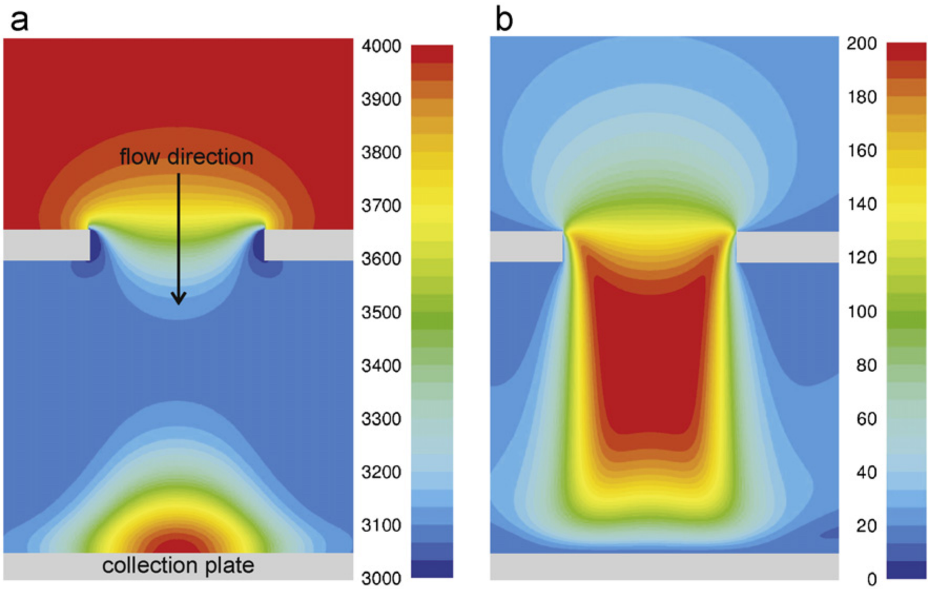

Fig. 7. Simulated pressure and velocity contours at the cross section of the round nozzle. (a) Static pressure (Pa). (b) Velocity (m/s).

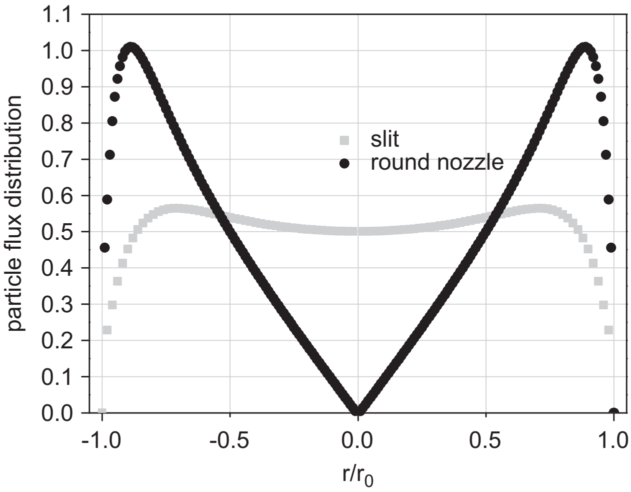

Fig. 8. Particle flux distribution across the nozzle of LPI (% of total flux/nozzle width interval). Curves correspond to slit and round nozzle. Horizontal axis is normalized by the half width of the nozzle and center of the nozzle is at the origin.

areas where the velocity changes steeply. Thus, the particles in the round nozzle have a less uniform stopping distance distribution and the change in the collection efficiency occurs on a wider particle size range than in the slit impactor.

Fig. 9 presents simulated impaction velocities for different sized particles in both the slit and the round nozzle stages. The nozzle length T is 0.1 mm. Note that some of the 25 nm dots are missing because they are not collected from all parts of the jet. It can be seen that the slit nozzle provides more uniform impaction velocities as anticipated by the jet exit plane velocity profiles. This suggests that the slit nozzle can be beneficial if the impaction energy of particles has to be carefully controlled.

5. Conclusions and discussion

The resolution (steepness of collection efficiency curve) of a single stage low pressure impactor was studied. Slit and round nozzle impactor stages with two different throat lengths were studied both experimentally and by simulations. Collection efficiencies of the stages were determined using monodisperse DOS particles and electrical calibration method. The operating pressure of the stages was 40 mbar and the cutpoint was 25 nm.

Two different current measurement setups were tested. In one of the setups stage current signal was measured from the collection plate and the body combination and in the other setup stage signal came from the collection plate only. It was found that the effect of diffusion losses and electrical losses on the collection efficiency steepness is very minor in the case of slit nozzle stage, even when the particle size is in the order of 10 nm.

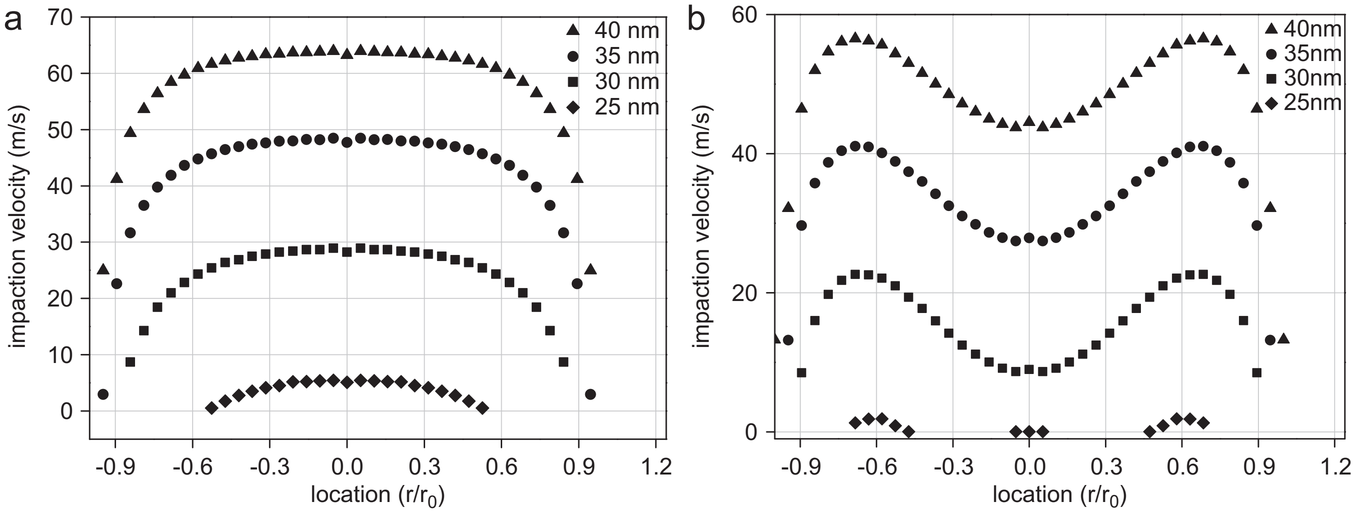

Fig. 9. Impaction velocities of different size particles in the short nozzles ($T=0.1$ mm). Horizontal axis is normalized by the half width of the nozzle. Nozzle center is at the origin. (a) Slit nozzle. (b) Round nozzle.

It was found that the shorter nozzle produced a better resolution for both the slit nozzle and the round nozzle LPI stages. The slit nozzle stage (throat length 0.1 mm, width of the slit 0.3 mm and jet-to-plate distance 0.5 mm) produced resolution that was higher than comparable cutpoint stages of many other well-known LPIs. From the simulated velocity flow fields it was possible to explain the differences in the resolution. A short nozzle throat compared to its width leaves the jet exit plane velocity profile under-developed, resembling a plug flow. This creates quite uniform impaction conditions across the jet, except at the very outer edges of the jet.

The slit nozzle stage produced better resolution than the round nozzle. This was found to be caused by the combination of jet exit plane velocity profile and the distribution of particle flux in the cross section of the jet. The exit plane velocity profile of the jet changes steeply at the outer edges because the flow velocity at the nozzle wall is zero. In the slit nozzle the particle flux distributes uniformly across the jet and in the round nozzle it concentrates at the edges of the jet. Therefore, the velocity distribution of particles after the round nozzle is nonuniform compared to the velocity distribution of particles after the slit nozzle. The nonuniformity in the particle velocities before the flow decelerates leads also to nonuniform stopping distances of particles across the jet and this in turn causes a decrease in resolution.

Because it was found that the short throat length offers uniform impaction conditions across the jet, impaction velocities of particles from 25 nm to 40 nm were also simulated. It was found that the uniform jet exit plane velocity distribution causes also uniform impaction velocities of same size particles. This can be very beneficial in applications where controlling the impaction energy of particles is important, such as studying the particle bounce and the charge transfer in the impaction of nanoparticles.

References

Abouali, O., & Ahmadi, G. (2005). A model for supersonic and hypersonic impactors for nanoparticles. *Journal of Nanoparticle Research*, *7*, 75–88.

Abouali, O., Saadabadi, S., & Emdad, H. (2011). Numerical investigation of the flow field and cut-off characteristics of supersonic/hypersonic impactors. *Journal of Aerosol Science*, *42*(2), 65–77.

Arffman, A., Marjamäki, M., & Keskinen, J. (2011). Simulation of low pressure impactor collection efficiency curves. *Journal of Aerosol Science*, *42*, 329–340.

Berner, A. (1972). Praktische erfahrungen mit einem 20-stufen-impactor. *Staub-Reinhalt. Luft*, *32*, 315.

de la Mora, J.F., Rao, N., & McMurry, P. (1990). Inertial impaction of fine particles at moderate reynolds numbers and in the transonic regime with a thin-plate orifice nozzle. *Journal of Aerosol Science*, *21*(7), 889–909.

Friedlander, S. (1999). Polymer-like behavior of inorganic nanoparticle chain aggregates. *Journal of Nanoparticle Research*, *1*, 9–15.

Gómez-Moreno, F., Rosell-Llompart, J., & Mora, J.F.d.l. (2002). Turbulence transition in impactor jets and its effects on impactor resolution. *Journal of Aerosol Science*, *33*, 459–476.

Hering, S.V., Flagan, R.C., & Friedlander, S.K. (1978). Design and evaluation of new low-pressure impactor. I. *Environmental Science & Technology*, *12*, 667–673.

Hering, S.V., Friedlander, S.K., Collins, J.J., & Richards, L.W. (1979). Design and evaluation of new low-pressure impactor. II. *Environmental Science & Technology*, *13*, 184–188.

Hillamo, R.E., & Kauppinen, E.I. (1991). On the performance of the berner low pressure impactor. *Aerosol Science and Technology*, *14*, 33–47.

Jurcik, B., & Wang, H. (1995). On the shape of impactor efficiency curves. *Journal of Aerosol Science*, *26*, 1139–1147.

Keskinen, J., Marjamäki, M., Virtanen, A., Mäkelä, T., & Hillamo, R. (1999). Electrical calibration method for cascade impactors. *Journal of Aerosol Science*, *30*, 111–116.

Keskinen, J., Pietarinen, K., & Lehtimäki, M. (1992). Electrical low pressure impactor. *Journal of Aerosol Science*, *23*, 353–360.

Leduc, S., Fredriksson, C., & Hermansson, R. (2006). Particle-tracking option in fluent validated by simulation of a low-pressure impactor. *Advanced Powder Technology*, *17*, 99–111.

Marple, V., Liu, B., & Whitby, K. (1974). On the flow fields of inertial impactors. *ASME Journal of Fluids Engineering*, *96*, 394.

Marple, V.A., & Liu, B.Y. (1975). On fluid flow and aerosol impaction in inertial impactors. *Journal of Colloid and Interface Science*, *53*(1), 31–34.

Marple, V.A., & Liu, B.Y.H. (1974). Characteristics of laminar jet impactors. *Environmental Science and Technology*, *8*, 648–654.

Marple, V.A., Rubow, K.L., & Behm, S.M. (1991). A microorifice uniform deposit impactor (moudi): Description, calibration, and use. *Aerosol Science and Technology*, *14*(4), 434–446.

Štefancová, L., Schwarz, J., Mäkelä, T., Hillamo, R., & Smolík, J. (2011). Comprehensive characterization of original 10-stage and 7-stage modified berner type impactors. *Aerosol Science and Technology*, *45*(1), 88–100.

Vanderpool, R., Lundgren, D., & Kerch, P. (1990). Design and calibration of an in-stack low-pressure impactor. *Aerosol Science and Technology*, *12*, 215–224.

Virtanen, A., Joutsensaari, J., Koop, T., Kannosto, J., Yli-Pirilä, P., Leskinen, J., Mäkelä, J., Holopainen, J., Pöschl, U., Kulmala, M., Worsnop, D., & Laaksonen, A. (2010). An amorphous solid state of biogenic secondary organic aerosol particles. *Nature*, *467*, 824–827.

Wang, S.C., & Flagan, R.C. (1990). Scanning electrical mobility spectrometer. *Aerosol Science and Technology*, *13*(2), 230–240.

Yli-Ojanperä, J., Kannosto, J., Marjamäki, M., & Keskinen, J. (2010). Improving the nanoparticle resolution of the elpi. *Aerosol and Air Quality Research*, *10*(4), 360–366.

Zare, A., Abouali, O., & Ahmadi, G. (2007). Computational investigation of airflow, shock wave and nano-particle separation in supersonic and hypersonic impactors. *Journal of Aerosol Science*, *38*(10), 1015–1030.

Paper 3

Arffman, A., Kuuluvainen H., Harra J., Vuorinen, O., Paxton, J., Yli-Ojanperä, J., Mäkela, J., Keskinen J., The critical velocity of rebound determined for sub-micron silver particles with a variable nozzle area impactor *Journal of Aerosol Science*, 86, 32–43, 2015.

Reprinted with permission from Elsevier.

Journal of Aerosol Science 86 (2015) 32–43

Contents lists available at ScienceDirect

Journal of Aerosol Science

journal homepage: www.elsevier.com/locate/jaerosci

The critical velocity of rebound determined for sub-micron silver particles with a variable nozzle area impactor

Anssi Arffman [1], Heino Kuuluvainen *,[1], Juha Harra, Ossi Vuorinen, Paxton Juuti, Jaakko Yli-Ojanperä, Jyrki M. Mäkelä, Jorma Keskinen

Aerosol Physics Laboratory, Department of Physics, Tampere University of Technology, Tampere, Finland

ARTICLE INFO

Article history:
Received 14 January 2015
Received in revised form
20 March 2015
Accepted 7 April 2015
Available online 15 April 2015

Keywords:
Silver nanoparticle
Rebound
Critical velocity
Low-pressure impactor

ABSTRACT

The critical velocity of rebound was determined for spherical silver aerosol particles in the size range of 20–1000 nm. A novel instrument, a variable nozzle area impactor, was especially designed for measuring the particle–surface interaction as a function of the particle impact velocity. The experimental results were combined with a numerical model in order to obtain the impact velocities. The experiments were carried out using a plain aluminum collection substrate in the impactor. Our results show that the critical velocity of rebound decreases from 14 to 0.022 m/s as the particle size increases from 20 to 1000 nm. Furthermore, the critical velocity was found to be proportional to the power of −1.6 of the particle size, instead of the theoretical inverse proportionality. This result is in line with the previous studies for micron-sized particles. In the nanoparticle size range, the obtained values are approximately 3–10 times greater than the recent literature values. This discrepancy can most likely be explained by the different surface materials. All in all, our results give valuable information about the particle–surface interactions in the sub-micron size range.

1. Introduction

Particle rebound from a surface is a fundamental phenomenon. Recently, it has been of interest in several fields of aerosol physics, including atmospheric aerosols and aerosol synthesis. For example, Virtanen et al. (2010) found an amorphous solid state of biogenic SOA (secondary organic aerosol) particles by investigating the bounce behavior of the particles. The further development has led to some experimental methods capable of measuring the bounce probability of the SOA particles as a function of the relative humidity in specific low-pressure impactor systems (Bateman et al., 2014; Saukko et al., 2012). Within the field of engineered nanoparticles, the research of the particle–surface interaction has been focused on the fragmentation and binding energy of agglomerates (Froeschke et al., 2003; Ihalainen et al., 2014; Seipenbusch et al., 2007, 2010). However, the lack of knowledge of the fundamental bounce properties of ultrafine particles limits the reliability of these methods.

When a particle impacts on a firm surface, it may either stick to it or be reflected. The process is mainly affected by three factors: the adhesion, the energy loss mechanisms in the particle and the initial velocity of the particle. With low initial

---

* Corresponding author.
E-mail address: heino.kuuluvainen@tut.fi (H. Kuuluvainen).
[1] A. Arffman and H. Kuuluvainen contributed equally to this work.

http://dx.doi.org/10.1016/j.jaerosci.2015.04.003
0021-8502/© 2015 Elsevier Ltd. All rights reserved.

velocities, the energy losses dominate and the particle is captured by the surface. When the initial velocity increases up to a critical velocity, the kinetic energy, even when reduced by the energy losses, is sufficient to overcome the adhesion energy and the particle rebounds. According to theoretical knowledge, the critical velocity is inversely proportional to the particle size (Dahneke, 1971; Wang & Kasper, 1991; Weir & McGavin, 2008). Experimentally, the values of the critical velocity have been determined for different materials of micron-sized particles and substrates (Wall et al., 1990), and for silver and sodium chloride nanoparticles on a mica substrate in the size range of 10–80 nm (Rennecke & Weber, 2013a). Both the datasets show similar particle size dependency compared to the theories, but the critical velocity values have a difference of several orders of magnitude if extrapolated into the same size range.

The experimental challenges in measuring the particle rebound of nanoparticles are often related to low-pressure conditions required for the impaction and to the detection of the particles in these conditions. The experimental method used by Rennecke & Weber (2013a) was based on scanning the impact velocity by means of the impaction pressure. By continuously measuring the electrical current downstream and the particle concentration upstream, the penetration of the impactor could be defined as a function of the impaction pressure. The advantage of the electrical detection of particles in low-pressure conditions is its accuracy and a good time resolution. Optical detection of particles has also been used in the bounce and fragmentation studies of nanoparticles (Ihalainen et al., 2014; Saukko et al., 2012). Its advantage is that the possible charge transfer is not affecting the detection. However, the optical detection cannot practically be used continuously in low-pressure conditions.

Measurement of the impact velocity of a single particle can be performed for micron-sized particles with a laser Doppler velocimetry (Wall et al., 1990). Because of limitations in the optical detection, the same method cannot generally be exploited for nanoparticles. Reuter-Hack et al. (2007) have applied the laser Doppler velocimetry method for agglomerates with mobility diameters below 500 nm, but for spherical particles that would not be possible. The lack of experimental methods has led to the utilization of numerical methods and computational fluid dynamics (CFD) simulations in defining the impact velocity for nanoparticles (Ihalainen et al., 2014; Kuuluvainen et al., 2013; Rennecke & Weber, 2013a; Virtanen et al., 2011). These studies are mainly based on the previous work of modeling the impactor flow field and collection efficiency curves (Arffman et al., 2011; Rennecke & Weber, 2013b). According to the study by Arffman et al. (2012), the impactor geometry significantly affects the size resolution of an impactor. The best results were obtained with a slit type low-pressure impactor having a minimized nozzle throat length. The advantage of this type of an impactor is a very small deviation in the impact velocity of a certain particle size. This is also a great advantage in defining the critical velocity for nanoparticles.

This study presents a new method for measuring the critical velocity of nanoparticles using a variable nozzle area impactor, and reports the results for spherical silver particles in the size range of 20–1000 nm. The method is based on an impactor design, where the deviation of the impact velocities in a single measurement for a certain particle size is minimized, and the pressure conditions controlled. The impactor consists of a narrow slit with a short nozzle throat length, and the nozzle area can be varied by changing the slit length. By decreasing the slit length, the impact velocity of a particle increases. Furthermore, the impact velocities are calculated for different particle sizes and different slit lengths with numerical methods.

2. Theoretical background

The theory of aerosol particle rebound from a firm surface was first introduced by Dahneke (1971). The theory includes the effect of the adhesion, the energy loss mechanisms in a particle and the particle initial velocity. Assuming a spherical particle and an infinite firm surface, the adhesion energy between the particle and the surface can be written as

$$E_{\mathrm{adh}} = \frac{A_{\mathrm{H}} d_{\mathrm{p}}}{12 z_0}, \tag{1}$$

where d_{p} is the particle diameter, A_{H} is the Hamaker constant and z_0 is the separation distance, usually assumed to be 0.4 nm. The Hamaker constant arises from the van der Waals interaction of molecules and is dependent on both particle and surface materials.

The amount of energy loss in the collision is mainly dependent on the mode of deformation in the particle. Fully elastic deformation completely restores the kinetic energy of the particle, and the velocity after the rebound equals the initial velocity. Practically, this sort of collisions only takes place among molecules and atoms. Considering the collisions of aerosol particles and firm surfaces, plastic deformation is always present to some extent. Plastic and elastic behavior of aerosol particles during rebound was extensively studied first by Rogers & Reed (1984). Thereafter, Wang & Kasper (1991) and Weir & McGavin (2008) developed the theoretical approach for the elastic and plastic behavior, respectively.

Depending on the energy losses and adhesion energy, the particle may either rebound or stick to the surface. For the initial velocity, there is a certain capture limit v_{crit}, i.e. the critical velocity of rebound. The relation between the initial velocity of the particle, perpendicular to the surface, and the rebound velocity of the particle is called the coefficient of restitution C_{R}. Combining Eq. (1) and the definition of the coefficient of restitution, the critical velocity of rebound can be written as

$$v_{\mathrm{crit}} = \alpha d_{\mathrm{p}}^{\beta}, \tag{2}$$

where the material coefficient

$$\alpha=\left(\frac{A_H\left(1-C_R^2\right)}{\pi z_0\rho_p C_R^2}\right)^{1/2}, \tag{3}$$

is dependent on the coefficient of restitution, the Hamaker constant and the particle density ρ_p. According to the theory of Dahneke (1971), the critical velocity is inversely proportional to the particle diameter, so the exponent β is set to be -1. The same proportionality is also found in the more recent models based on both the elastic (Wang & Kasper, 1991) and plastic (Weir & McGavin, 2008) deformation of particles. The difference between the elastic and plastic models is that the material coefficient α obtains significantly higher values in the latter case.

Majority of the previous experimental studies regarding the critical velocity have found a dependence on the particle size similar to Eq. (2). However, in contrast to the theoretical models, the exponent values (β) may significantly differ from -1. As reviewed by Wall et al. (1990), the exponents were usually between -1.2 and -1.8 including the results of four different studies for micron-sized particles (Cheng & Yeh, 1979; D'Ottavio et al., 1982; Wall et al., 1990; Wang & John, 1988). Only the results of Esmen et al. (1978) showed a smaller exponent value (-0.39) and the highest values were measured for harder materials such as copper and glass (Rogers & Reed, 1984). Also the results of Rennecke & Weber (2013a) for silver nanoparticles obey Eq. (3) and are proportional to the power of -3.0 of the particle size, resulting a relatively steep slope. With respect to the theoretical knowledge, the steeper slopes obtained from the measurements are explained with a transition from elastic to plastic deformation. The transition would require some of the factors in Eq. (3) to be particle size dependent. That might be the Hamaker constant or the coefficient of restitution (Tsai et al., 1990).

3. Experimental method

3.1. Variable nozzle area impactor

An illustration representing the key features of the variable nozzle area impactor is shown in Fig. 1. The impactor consists of a nozzle plate, an adjustable cover and an impaction substrate. The nozzle plate contains a rectangular slit with a width of 0.3 mm and a maximum length of 30 mm. The adjustable cover can be slid manually on top of the nozzle in order to decrease the slit length down to 3 mm, and, thus, vary the nozzle area. The impactor stage was made vacuum tight by using O-ring sealings up- and downstream. The opening where the adjustable cover is connected to the impactor was machined as tight as possible, and further sealed with mould silicon. The nozzle throat length in the impactor (also the thickness of the nozzle plate) is 0.1 mm and the jet-to-plate distance is 0.5 mm. The impaction substrate material used in this study was machined aluminum. Measurements were carried out using both plain and greased (Apiezon vacuum grease) substrates. The function of the grease was to prevent particle bounce, and, thus, serve as a reference measurement.

3.2. Setup for 20–200 nm particles

A schematic presentation of the experimental setup is shown in Fig. 2. Spherical and monodisperse silver nanoparticles, in the size range of 20–200 nm, were generated via evaporation–condensation method followed by sintering and size

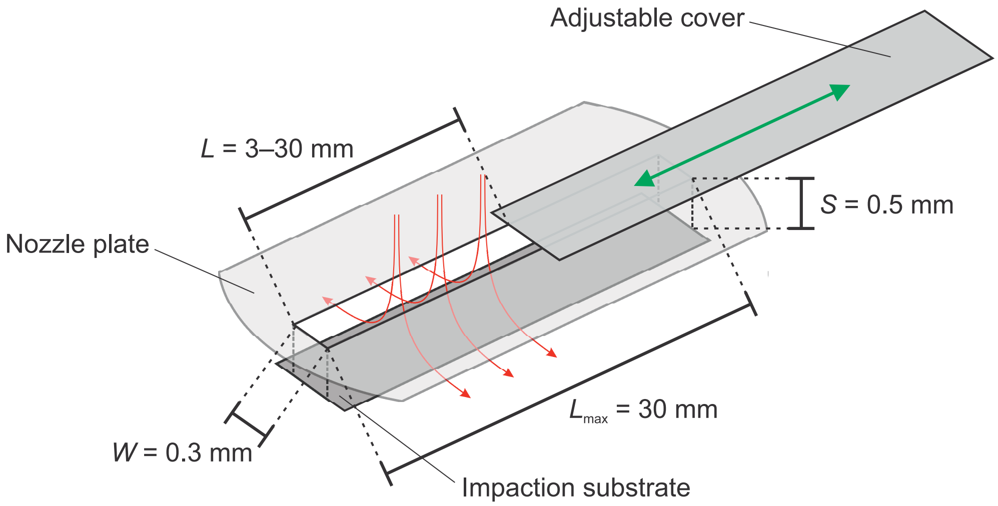

Fig. 1. An illustration of the variable nozzle area impactor. W is the slit width, S is the jet-to-plate distance, L_{max} is the maximum slit length and L is the slit length. By changing the slit length with the adjustable cover (green arrow), the area of the nozzle ($L \times W$) can be varied. The red arrows represent the flow lines through the nozzle. Note that the figure is out of scale. (For interpretation of the references to color in this figure caption, the reader is referred to the web version of this paper.)

selection (Harra et al., 2012; Scheibel & Porstendörfer, 1983). Silver was evaporated from a small amount of bulk material situated at the center of a tube furnace at temperatures of 1200–1500 °C, depending on the desired particle size. The metal vapor was first carried out of the furnace (3 lpm) and then diluted with nitrogen gas (3 lpm). The silver particles, formed by condensation after cooling, were passed through a coagulation chamber before the sintering step. In order to sinter relatively large particles (~100 nm), two successive furnaces were employed. Depending on the particle size, the flow rate through the furnaces was 0.3–1 lpm. The function of the latter furnace (400 °C) was to smooth the particle surfaces from bumps caused by the partial evaporation and subsequent formation of smaller particles near the bulk melting point (Schmidt-Ott, 1988; Zihlmann et al., 2014) in the first sintering furnace (600–800 °C). After sintering, a monodisperse particle mobility size distribution was realized with a Vienna-type differential mobility analyzer (DMA). Because of the nitrogen gas used in the sheath flow and as a carrier gas in the previous steps, the final sample was extremely dry (RH < 1%).

After the DMA, a bridge dilution system followed by a simple corona charger were used to control the particle number concentration entering the impactor. For the corona charger, the particle charging efficiency has been previously determined by Arffman et al. (2014). The charger was used for particle sizes larger than 40 nm, and the dilution was adjusted so that the total measured current was approximately 20 fA. This ensured that the impactor plate would not overly load from the collected particles and, thus, interfere with the particle rebound from the surface. The maximum particle area fraction on the impactor plate during the measurements was estimated to be approximately 5%. A vacuum pump was used to attain the required low-pressure conditions (106–256 mbar) in the variable nozzle area impactor. Pressures were measured before and after the impactor. Furthermore, a critical orifice inlet assured a constant volumetric flow rate (1.18 lpm). The particles were measured using electrical detection. The impactor substrate and a filter downstream were connected to electrometers. Particle samples were collected on a carbon film using a sampler based on electrical field deposition and analyzed with a transmission electron microscope (TEM, Jeol JEM-2010).

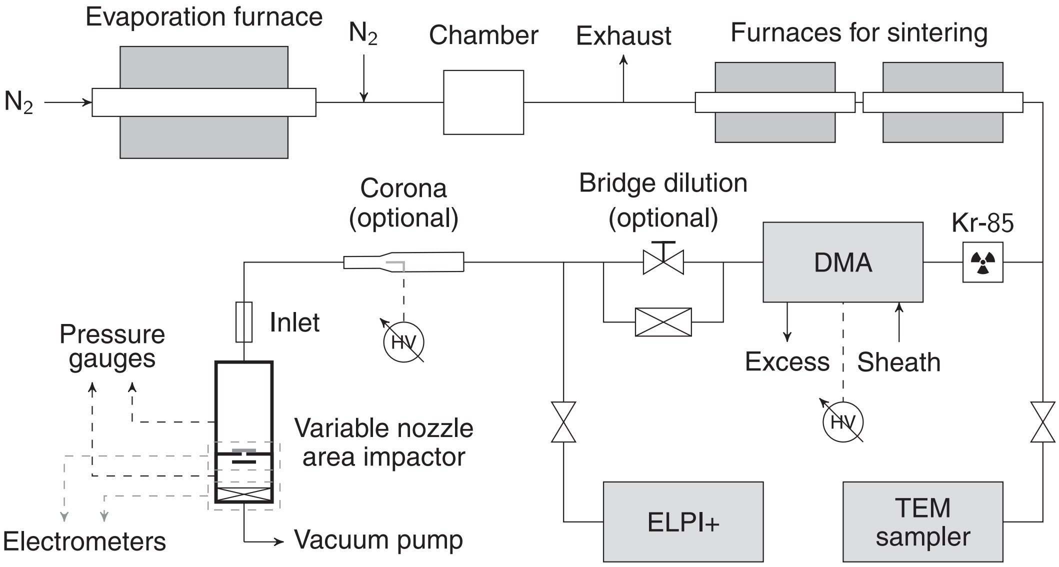

Fig. 2. A schematic of the generation and measurement setup of 20–200 nm silver particles.

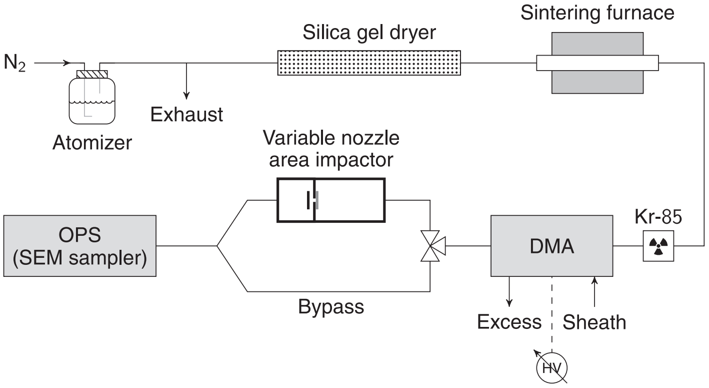

Fig. 3. A schematic of the generation and measurement setup of 400–1000 nm silver particles. For collecting particle samples, the OPS was replaced by the SEM sampler.

3.3. Setup for 400–1000 nm particles

Figure 3 shows the generation and measurement setup for silver particles in the size range of 400–1000 nm. Commercial silver powder (Inframat Advanced Materials, purity 99.95%, average size 0.7–1.5 μm, near-spherical) was dispersed in water and sprayed with an atomizer aerosol generator (Topas ATM 220). Due to a relatively small size of the generated droplets (Harra et al., 2013), we were unable to utilize the largest (>1 μm) particles in the powder. In order to prevent sedimentation, the dispersion was ultrasonificated and stirred with a magnetic mixer before and during the spraying process, respectively. When leaving the atomizer, the aerosol was dried with a silica gel dryer (RH $<$ 10%) and sintered in a furnace (600 °C). Particle size selection was carried out with a Vienna-type DMA which was followed by the variable nozzle area impactor. Here, the impactor pressure and the flow rate were 960 mbar and 1.0 lpm, respectively. Because the measurements of the nearly micron-sized particles were conducted in atmospheric pressures, and the particle concentration was low, in the order of 10 cm^{-3}, an optical particle sizer (OPS, TSI 3330) was used as a particle number counter instead of electrical detection. This also meant that the critical orifice inlet and the filter before and after the impactor, respectively, were not used. Reference particle concentration was measured by bypassing the impactor. Particle samples were collected on a holey carbon film using a flow-through sampler and analyzed by a scanning electron microscope (SEM, Zeiss ULTRA PLUS).

4. Numerical simulations

CFD simulations were used to determine the impaction velocities. The description of the employed methods can be found in a previous study (Arffman et al., 2011), and only a brief description of the methods is given here. First, we simulated the flow fields in the impactor with Ansys Fluent, Release 14.1 software. Simulations were carried out in 2D, and the boundary conditions were the mass flow rate and the static pressure at the outlet. Flows were assumed to be laminar as the Reynolds' numbers were in the order of 500 at the maximum. The grid was made very dense near the collection plate and the wall distances were in the range of 0.5–1 μm above the collection plate. Changing the nozzle area (i.e. the slit length) was taken into account in the simulations by changing the mass flow rate per depth of the slit length. Particle tracking simulations were carried out using Ansys Fluent complemented with a user defined function to calculate the particle drag in the slip regime. The particles were released a few centimeters upstream of the nozzle and tracked until they impacted to the collection plate or reached the flow outlet. Figure 4(a) shows the simulated normal component of the impaction velocities for the particle size of 500 nm with different slit lengths. The normalized distance from the center of the nozzle is on the horizontal axis, and the impaction velocity is on the vertical axis. Figure 4(a) shows that the impaction conditions and the impaction velocities can be well controlled in the slit type impactor.

From the particle track data, also the collection efficiencies can be determined. Figure 4(b) shows this for the operation pressures of the study. The markers represent the simulated cutpoints and the solid lines are linear fits. By measuring the cutpoint as a function of the slit length for monodisperse particles, it is possible to determine the effective density of the particles. This is accomplished by comparing the measured cutpoint to the simulated aerodynamic cutpoint. This can be defined from Fig. 4(b), as the cutpoint is now defined as a function of the slit length. Finally, the following equation can be used to calculate the effective density (Kelly & McMurry, 1992):

$$\rho_{\mathrm{eff}}=\frac{C_{\mathrm{a}}d_{\mathrm{a}}^{2}}{C_{\mathrm{m}}d_{\mathrm{m}}^{2}}\rho_{0}, \tag{4}$$

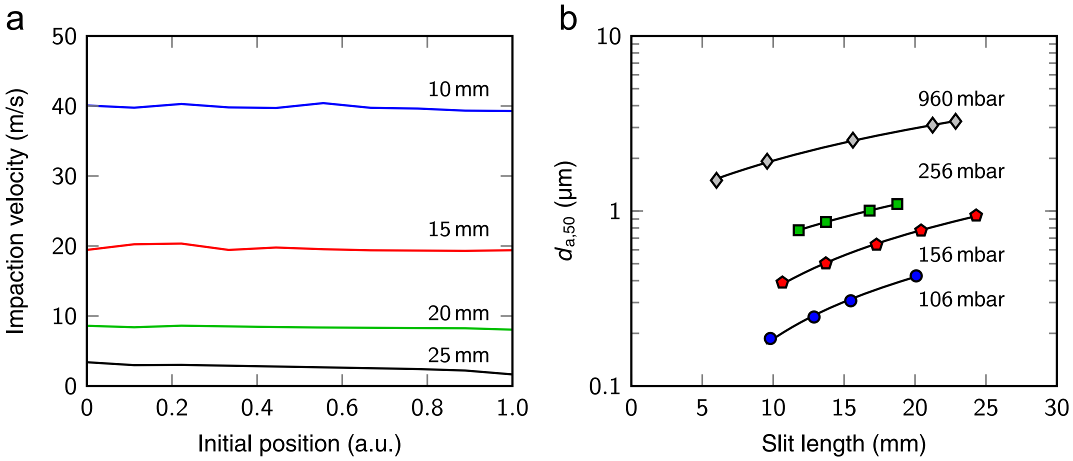

Fig. 4. (a) The normal component of the impaction velocity of 500 nm (aerodynamic diameter) particles as a function of the initial position (normalized distance from the center of the nozzle) of the particles for different slit lengths. The pressure is 106 mbar and the flow rate is 1.18 lpm. (b) The simulated cutpoint diameters as a function of the slit length for different operation pressures. The flow rate is 1.18 lpm for pressures 106–256 mbar and 1.0 lpm for 960 mbar.

where d_a and d_m are the aerodynamic and the mobility diameters, respectively, C_a and C_m are the corresponding slip correction factors and ρ_0 is the unit density.

In this study, the simulated and measured cutpoints are matched by using the effective density as a fitting parameter. The parameter is only an estimate of the effective density, because it includes non-idealities such as the width of the DMA output and uncertainties in the measured flow rates and pressures. However, if the effective density is known a priori (e.g. bulk density) or measured with a reference method, it also provides a way to validate the model. Figure 5(a) schematically shows the fitting procedure of the simulated and measured collection efficiencies for a certain particle size. Also two different methods for defining the essential parameters are illustrated. The slit length where the bounce is initiated is referred as the critical slit value and abbreviated with L_{crit}. The slit length corresponding to a collection efficiency of 50% is referred as L_{50}. In the fitting procedure, the L_{50} values of the simulated and measured collection efficiencies are superimposed by changing the effective density of the particles. As the schematic example in Fig. 5(a) shows, the simulated collection efficiency curves are steeper than the measured ones as a consequence of the non-idealities in the measurement.

There are two different methods for defining the critical slit length principally shown in Fig. 5(a). In the first method (1), the critical slit length $L_{crit,1}$ is obtained straightforwardly from the measured curve corresponding to the onset of rebound. The problem with this method is that it may result in too low impaction velocities or even non-impacting particles with the collection efficiencies below 50% arising from the steepness of the simulated curve. The solution is the second method (2) in which we take the critical collection efficiency $\eta_{crit,2}$ corresponding to the onset of the rebound and obtain the critical slit length $L'_{crit,2}$ from the simulated curve. However, this method is sensitive only in a region where the collection efficiency is linearly dependent on the impact velocity. Similar observation on the dependence of normalized impaction velocity on collection efficiency in the low pressure impactor was presented also by Rennecke & Weber (2013a). Figure 5(b) illustrates this dependency for a simulated dataset. In other words, the critical collection efficiency is no more unambiguous for high impact velocities. Based on the pros and cons of these two methods, we use the first method (1) when the onset of rebound is seen with the collection efficiencies above 50% and the second method for the collection efficiencies below 50%. The fitting procedure assures that two methods agree at L_{50}.

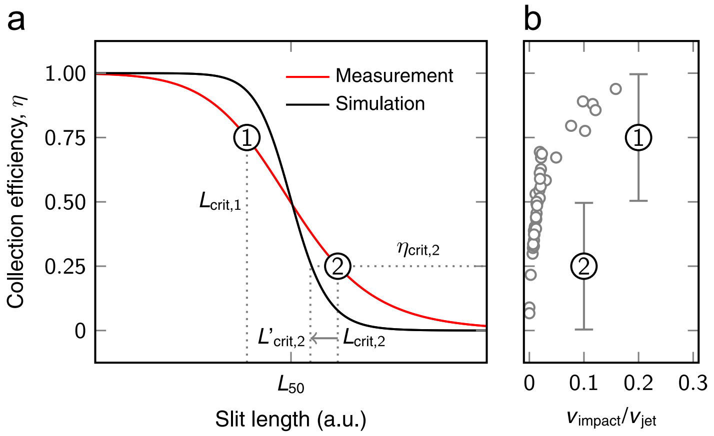

Fig. 5. (a) An example of a measured and simulated collection efficiency curve as a function of the slit length. Two different methods for defining the critical slit length are presented. (b) Normalized impact velocity as a function of the collection efficiency and the operation ranges of the methods.

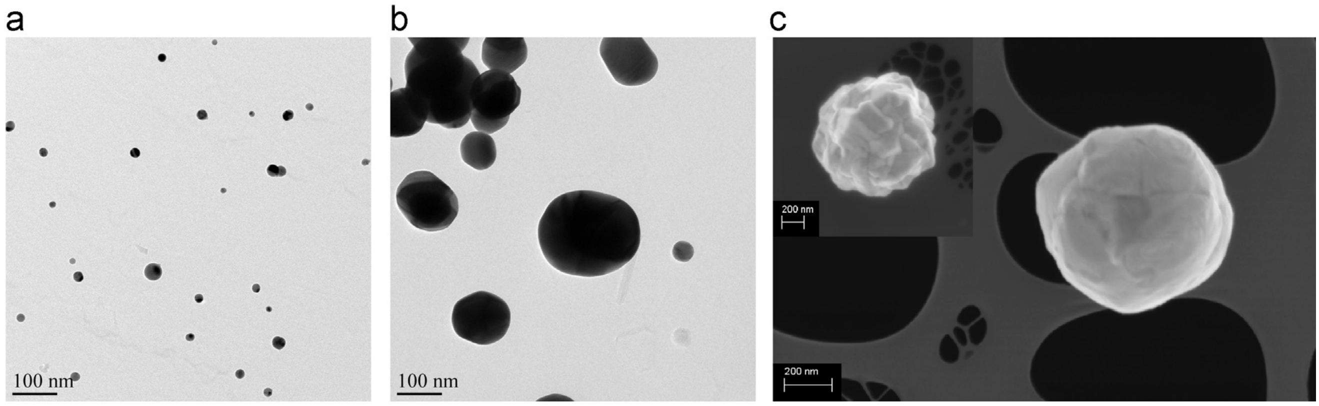

Fig. 6. (a–b) TEM micrographs of the silver nanoparticles generated with the evaporation–condensation method. The temperature of the evaporation furnace (°C), the temperature of the first sintering furnace (°C) and the flow rate in the sintering furnaces (lpm) were (a) 1200, 600 and 1.0 and (b) 1500, 800 and 0.3, respectively. Both micrographs have the same size bar of 100 nm. (c) An SEM micrograph of a micron-sized silver powder particle sintered at 600 °C. The inset shows an unsintered particle. The size bars are 200 nm.

5. Results and discussion

5.1. Morphology and density

In order to be certain that the generated silver particles were spherical, both the morphology and density of the particles were characterized. Figure 6(a) and (b) shows TEM micrographs of the extreme cases, i.e., smallest (~20 nm) and largest (>100 nm) silver particles generated using the evaporation–condensation method. It should be noted that the TEM samples were collected before the size selection. However, even the largest particles (~200 nm) are quite spherical with smooth surfaces. An SEM micrograph in Fig. 6(c) shows that an unsintered micron-sized powder particle is near spherical, although somewhat angular shaped. After sintering, the particle surface becomes smoother.

The effective density of the particles was measured and calculated by a method described by Ristimäki et al. (2002), and more recently by Kuuluvainen et al. (2015). In this study, the particles classified by the DMA were measured with an electrical low pressure impactor (Dekati ELPI+) (Järvinen et al., 2014; Keskinen et al., 1992). The first instrument classifies the particles according to their mobility diameter while the latter measures the aerodynamic diameter of the particles. These two particle sizes can be used to calculate the effective density of the particles with Eq. (4).

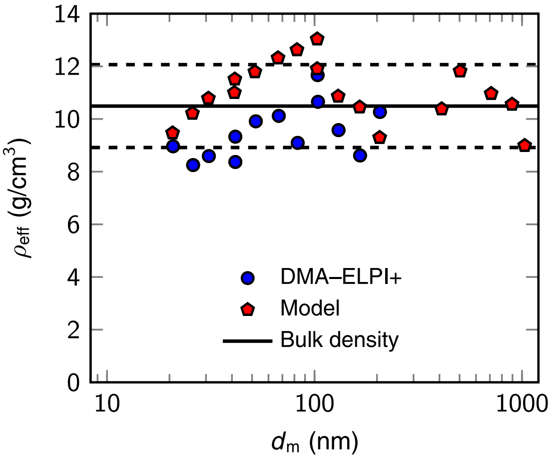

Fig. 7. The effective density of the silver particles as a function of the particle mobility size. Both measured values (DMA–ELPI+) and values obtained from the model are shown. The black line corresponds to the bulk density of silver and the dashed lines give an idea of the estimated experimental error of the method (±15%).

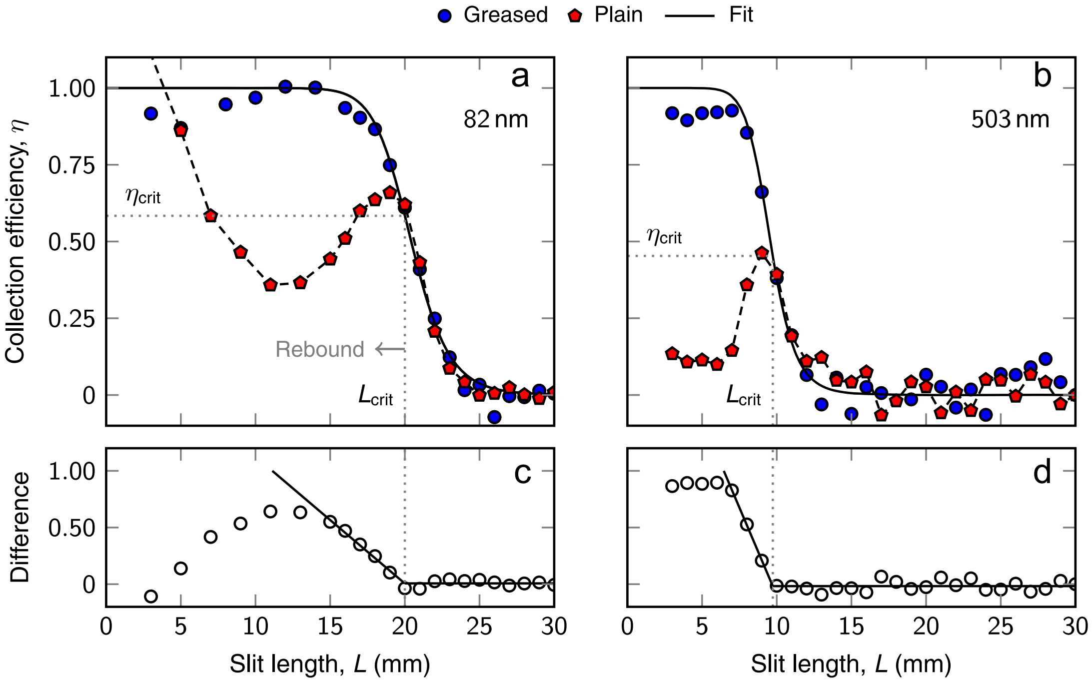

Fig. 8. The collection efficiency of (a) 82 nm (pressure 156 mbar, flow rate 1.18 lpm) and (b) 503 nm (960 mbar, 1.0 lpm) silver particles as a function of the slit length for a greased and a plane impaction surface. An electrical and an optical detection was used for the 82 nm and the 503 nm particles, respectively. (c–d) The onset of rebound is determined from the difference between the fitted collection efficiency curve and the results obtained for the plain surface.

The obtained results (Fig. 7), ranging approximately from 8 to 11 g/cm^3, are close to the bulk value of silver (10.49 g/cm^3), indicating that the particle material is silver and the shape is spherical. The experimental error using a similar method was reported to be approximately 15% (Ristimäki et al., 2002). Additional discrepancies from the bulk value at smaller particle sizes are likely caused by impurities (de la Mora et al., 2003), whereas, lower effective density of larger particles can most likely be attributed to minor deviations from spherical shape (Brockmann & Rader, 1990). The modeled densities are calculated as described in Section 4. The modeled effective densities are close to the bulk value and measured densities which verifies the validity of the used simulation methods.

5.2. *Collection characteristics*

Figure 8 shows two examples of the particle collection efficiency curves measured by using a plain and a greased surface in the variable nozzle area impactor. The measurement procedure started in every case with the slit fully open at 30 mm, and the slit length was gradually shortened at intervals of 1 mm down to 3 mm. At longer slit lengths, corresponding to lower particle velocities, no particle impaction on the surface occurs. When the slit length decreases, the particle velocity increases, and, thus, the particles start to impact. When using a greased surface, the collection efficiency reaches ~100% at a sufficiently low slit length.

In the case of the plain surface, the collection efficiency follows the curve obtained with the greased surface, until, at shorter slit lengths it begins to decrease due to the particle rebound from the surface. The slit length corresponding to the point where the efficiency curves diverge is the critical slit length L_{crit}, that is used to calculate the critical velocity of rebound. To define the critical slit lengths from the experimental data, the difference between the fitted collection efficiency curve and the results obtained for the plain surface is used as shown in Fig. 8(c) and (d). The onset of rebound is determined from the intersection of two linear fits.

Interestingly, when using electrical detection, the “collection efficiency” in the case of the plain surface begins to increase again at the shortest slit lengths (high velocities), at some cases reaching even values much higher than 1. This can be inferred as charge transfer between the particles and the surface. There seems to be a certain velocity limit after which the charge transfer phenomenon rapidly increases and starts to dominate the electrical detection at higher velocities. This may refer to the onset of plastic deformation strongly affecting the material properties of the particle or the contact area between the surface and the particle. From Fig. 8(a), we can estimate that this onset for 82 nm particles is at a slit length of approximately 15 mm, which corresponds to an impact velocity of approximately 7.8 m/s. In order to better understand this phenomenon, further research is required.

Figure 9 shows the critical slit values and corresponding critical collection efficiencies as a function of the mobility particle size. As already discussed in Section 4, depending on the critical collection efficiency value either critical collection efficiency or the critical slit value is used to simulate the critical velocities. Error bars in the critical collection efficiency values are calculated by assuming uncertainty of 1 mm in the measured critical slit length.

5.3. *Critical velocity of rebound*

Figure 10 shows the determined critical velocities of rebound for silver particles as a function of the particle diameter. Colors indicate different operation pressures used in the measurements. Also, the critical velocities for large unsintered particles are shown (see inset in Fig. 6(c)). The different operation pressures were mainly used in order to adjust the cutpoint and operate in different particle size ranges. To be sure that the operation pressure does not affect the results, several particle sizes were measured with different operation pressures. The flow rates were 1.18 and 1.0 lpm for the operation pressures of 106–256 and 960 mbar, respectively. The error bars in Fig. 10 describe the sensitivity of the method

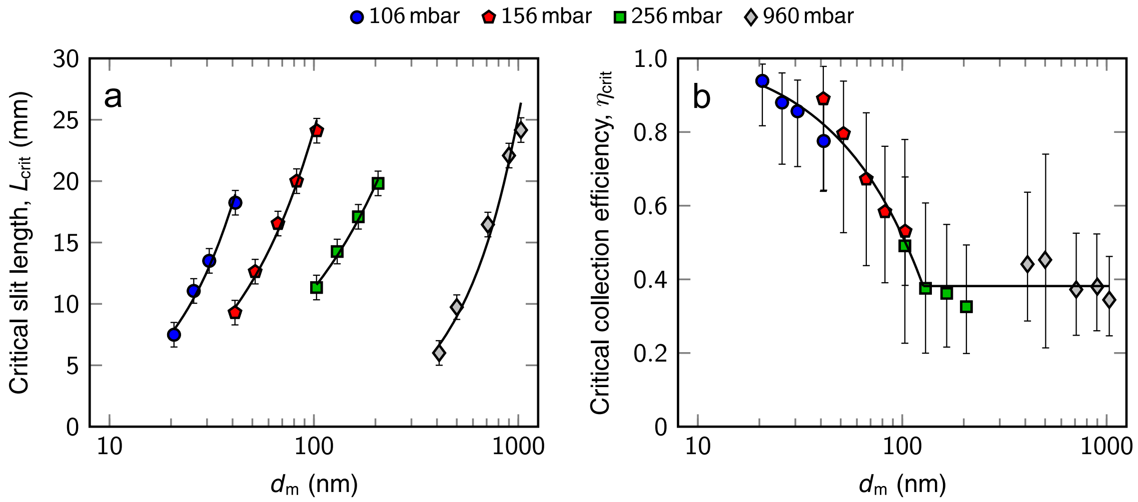

Fig. 9. (a) The critical slit length and (b) the critical collection efficiency as a function of the particle mobility size. The error bars represent an uncertainty of 1 mm in the determined slit length. Solid lines are guides for an eye.

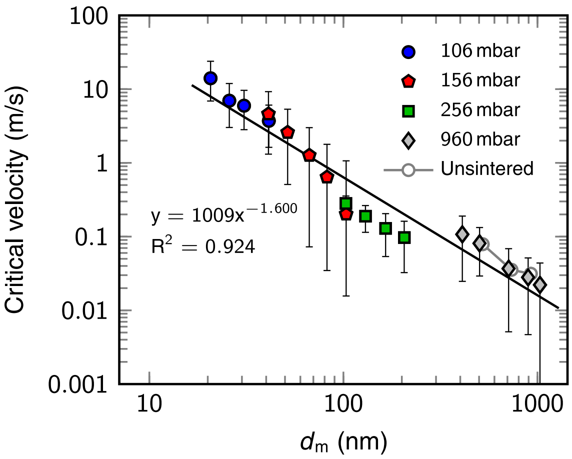

Fig. 10. The critical velocity as a function of the particle mobility diameter. The error bars correlate to an uncertainty of ±1 mm in determining the critical slit length. Note that the asymmetric error bars are not an effect of the log scale. A power fit (solid line) to the results gives an exponent of −1.6. (For interpretation of the references to color in the text, the reader is referred to the web version of this paper.)

Table 1
The results and important parameters corresponding to the experiments and the determination of the critical velocity. The effective density ρ_{eff} is a fitting parameter obtained from the model.

d_m (nm)	p (mbar)	L_{50} (mm)	L_{crit} (mm)	ρ_{eff} (g/cm^3)	v_{crit} (m/s)
21	106	9.8	7.5	9.4	14.03
26	106	12.9	11.1	10.2	6.97
31	106	15.5	13.5	10.8	5.96
41	106	20.1	18.2	11.5	3.71
41	156	10.6	9.3	11.0	4.60
52	156	13.7	12.6	11.8	2.59
67	156	17.3	16.5	12.3	1.26
82	156	20.4	20.0	12.6	0.641
103	156	24.3	24.1	13.1	0.202
103	256	11.8	11.3	11.9	0.281
130	256	13.7	14.3	10.9	0.189
165	256	16.8	17.1	10.4	0.129
206	256	18.8	19.8	9.3	0.097
410	960	6.0	7.1	10.4	0.107
503	960	9.6	9.7	11.8	0.081
710	960	15.6	16.5	11.0	0.037
895	960	21.2	22.1	10.6	0.028
1030	960	22.9	24.2	9.0	0.022
522*	960	9.7	10.0	11.2	0.079
735*	960	15.9	16.8	10.3	0.035
924*	960	22.2	23.0	10.5	0.031

* Unsintered.

with respect to the critical slit length. The sensitivity analysis limits are calculated by adding and subtracting 1 mm from the defined critical slit values. Table 1 shows the critical velocity values for each experiment and all the important parameters. As explained in Section 2, according to the current theoretical knowledge, the critical velocity of rebound is inversely proportional to the particle size with an exponent of −1. However, a fit to the entire experimental data of this work provides an exponent value of −1.6 ($R^2 = 0.924$). The results for unsintered particles show that the fine structure of the particle surface has practically no effect on the critical velocity.

Figure 11 shows the results of this work in relation to the results of other studies. As seen in the variation of the results for micron-sized particles, particle and surface materials significantly affect the critical velocity of rebound. The results of this work are unfortunately not strictly comparable to these, because there are no previous results available for micron-sized spherical silver particles. However, the dependency on the particle size seems to be very similar with several other studies, and the exponent values in Eq. (3) are close to each other. The results of this work differ most from the results by Rogers & Reed (1984) for copper particles on a glass substrate. The amount of data points and the observed particle size range in their study are rather small, which most likely results in a significant uncertainty in the obtained exponent value of −4.8. However, even if copper can be regarded as similar material compared to silver, there is a difference of several orders of

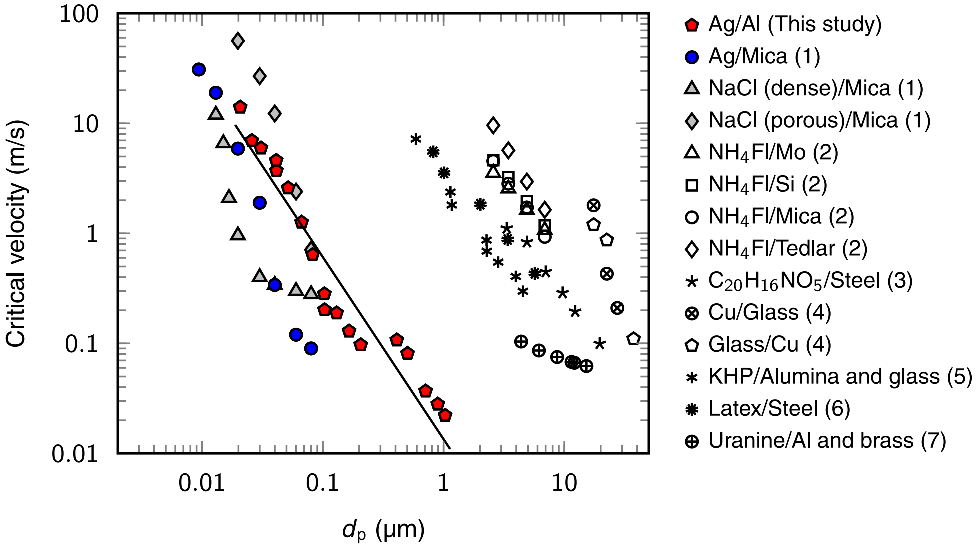

Fig. 11. The results of this work in relation to the previous studies by (1) Rennecke & Weber (2013a), (2) Wall et al. (1990), (3) Wang & John (1988), (4) Rogers & Reed (1984), (5) D'Ottavio et al. (1982), (6) Cheng & Yeh (1979) and (7) Esmen et al. (1978). The legend shows the material of the particle/surface. For spherical particles, the mobility diameter equals the physical particle size.

magnitude in the critical velocity. This implies that the critical velocity of rebound can be highly dependent on both the particle and surface materials.

The results of Rennecke & Weber (2013a), shown in Fig. 11, are determined for spherical silver nanoparticles. Their results differ by a factor of 3–10 from the results of this work. The dependency on the particle size is steeper compared to the results of this work as the exponent value is -3.0. A power fit to their data set is fairly good ($R^2 = 0.978$), but the size range is restricted and the uncertainty of single data points has not been estimated, except a lower resolution limit. The data points above 40 nm were even below the resolution limit, serving only as an upper limit for the critical velocity. However, compared to the results of micron-sized particles, the results of this work and the results of Rennecke & Weber (2013a) are actually rather close to each other. The discrepancies could be explained by the difference in the surface material used in the experiments. The surface material in this study was aluminum while Rennecke & Weber (2013a) used mica. Unfortunately, there are no literature values of Hamaker constants available for these material pairs. Also the coefficient of restitution is unknown.

One aspect that was theoretically speculated by Rennecke & Weber (2013a) was that they see a transition from the elastic to plastic deformation in their results, and therefore the dependency of critical velocity of rebound on particle size is very steep in their results. They explained that their results cover this transition region, and that the slope of the critical velocity is changing after approximately 40 nm with increasing particle size. Within the accuracy of the method, the results of this study refer to a completely different conclusion: the critical velocity will decay exponentially at least up to one micron. On the other hand, even if the methods exploited in these two studies are close to each other, there are differences in the impactor design, experimental procedures, data interpretation and simulation of the impaction velocities. It might be difficult to recognize all the possible factors affecting the accuracy of the determined critical velocities. We believe that the variable nozzle area impactor with its advantages, connected to the simulation of the impaction velocities and the precise analysis of the particle effective density, provides an accurate method for determining the critical velocity of rebound.

6. Conclusions

The critical velocity of rebound was determined for spherical silver particles covering for the first time the size range from nanoparticles to micron-sized particles. The results show that the critical velocity of rebound decreases from 14 m/s to 0.022 m/s as the particle size increases. Furthermore, a clear exponential decay was observed and the proportionality to the power of -1.6 of the particle size maintained throughout the wide size range. No transitions were seen, even if the present theories, including different approaches to the plastic and elastic deformation of particles, would predict this exponent to be -1. The obtained exponent value is also very close to the average value of the previous experimental studies. The reliability of the exponent value obtained in this work is also supported by the wide particle size range and a large number of data points. It seems that there might be a yet theoretically unknown physical factor affecting the size dependency of the critical velocity, or the transition from elastic to plastic deformation is evenly covering almost the whole size range of aerosol particles. One possible reason for this would be a size dependency in the Hamaker constant or in the coefficient of restitution.

Comparing the results of this work to the previous studies, it is evident that both the particle and surface material properties can highly affect the critical velocity of rebound. The critical velocities for the micron-sized particles, if extrapolated into the submicron size range, would be one to two orders of magnitude higher than the values measured here for silver particles. Most of the particle materials measured earlier in the supermicron size range would even require supersonic velocities to bounce in the nanoparticle range. The best agreement with the previous studies was obtained for nanoparticles (Rennecke & Weber, 2013a). However, there were still discrepancies of a magnitude at the maximum. The reason for these discrepancies may lie in the different surface material used in the experiments. Because the methods determining the critical velocities are not so straightforward, it may be difficult to assess the accuracy of the results.

The results of this work fill the gap between the previous experimental studies of the critical velocity for micron-sized particles (Wall et al. 1990) and the more recent results for silver nanoparticles (Rennecke & Weber, 2013a). This is an important step towards understanding the fundamental phenomenon of particle bounce from the molecular to macroscopic size range. As shown in the previous studies for micron-sized particles, the critical velocity can strongly be dependent on the particle and surface materials. This is most likely true also in the case of smaller particles and extended size ranges. Thus, further research is required with different particle materials and different surfaces. The methods introduced in this work, including the variable nozzle area impactor and the determination of the impact velocities with numerical simulations, will be useful in future studies.

Acknowledgements

H. Kuuluvainen and J. Harra acknowledge the TUT's graduate school for financial support. The authors thank Dr. Mari Honkanen and Dr. Essi Sarlin at the Department of Materials Science (TUT) for the electron microscopy images.

References

Arffman, A., Marjamäki, M., & Keskinen, J. (2011). Simulation of low pressure impactor collection efficiency curves. *Journal of Aerosol Science*, *42*(5), 329–340.

Arffman, A., Yli-Ojanperä, J., Kalliokoski, J., Harra, J., Pirjola, L., Karjalainen, P., Rönkkö, T., & Keskinen, J. (2014). High-resolution low-pressure cascade impactor. *Journal of Aerosol Science*, *78*, 97–109.

Arffman, A., Yli-Ojanperä, J., & Keskinen, J. (2012). The influence of nozzle throat length on the resolution of a low pressure impactor—An experimental and numerical study. *Journal of Aerosol Science*, *53*, 76–84.

Bateman, A., Belassein, H., & Martin, S. (2014). Impactor apparatus for the study of particle rebound: Relative humidity and capillary forces. *Aerosol Science and Technology*, *48*(1), 42–52.

Brockmann, J.E., & Rader, D.J. (1990). A response to nonspherical particles and experimental determination of dynamic shape factor. *Aerosol Science and Technology*, *13*(2), 162–172.

Cheng, Y.-S., & Yeh, H.-C. (1979). Particle bounce in cascade impactors. *Environmental Science and Technology*, *13*(11), 1392–1396.

Dahneke, B. (1971). The capture of aerosol particles by surfaces. *Journal of Colloid and Interface Science*, *37*(2), 342–353.

de la Mora, J.F., de Juan, L., Liedtke, K., & Schmidt-Ott, A. (2003). Mass and size determination of nanometer particles by means of mobility analysis and focused impaction. *Journal of Aerosol Science*, *34*(1), 79–98.

D'Ottavio, T., Goren, S.L., & Samuvel, D. (1982). Aerosol capture in granular beds in the impaction dominated regime. *Aerosol Science and Technology*, *2*(2), 91–108.

Esmen, N.A., Ziegler, P., & Whitfield, R. (1978). The adhesion of particles upon impaction. *Journal of Aerosol Science*, *9*(6), 547–556.

Froeschke, S., Kohler, S., Weber, A.P., & Kasper, G. (2003). Impact fragmentation of nanoparticle agglomerates. *Journal of Aerosol Science*, *34*(3), 275–287.

Harra, J., Mäkitalo, J., Siikanen, R., Virkki, M., Genty, G., Kobayashi, T., Kauranen, M., & Mäkelä, J.M. (2012). Size-controlled aerosol synthesis of silver nanoparticles for plasmonic materials. *Journal of Nanoparticle Research*, *14*(6), 870.

Harra, J., Nikkanen, J.-P., Aromaa, M., Suhonen, H., Honkanen, M., Salminen, T., Heinonen, S., Levänen, E., & Mäkelä, J.M. (2013). Gas phase synthesis of encapsulated iron oxide-titanium dioxide composite nanoparticles by spray pyrolysis. *Powder Technology*, *243*, 46–52.

Ihalainen, M., Lind, T., Arffman, A., Torvela, T., & Jokiniemi, J. (2014). Break-up and bounce of TiO_2 agglomerates by impaction. *Aerosol Science and Technology*, *48*(1), 31–41.

Järvinen, A., Aitomaa, M., Rostedt, A., Keskinen, J., & Yli-Ojanperä, J. (2014). Calibration of the new electrical low pressure impactor (ELPI+). *Journal of Aerosol Science*, *69*, 150–159.

Kelly, W.P., & McMurry, P.H. (1992). Measurement of particle density by inertial classification of differential mobility analyzer-generated monodisperse aerosols. *Aerosol Science and Technology*, *17*(3), 199–212.

Keskinen, J., Pietarinen, K., & Lehtimäki, M. (1992). Electrical low pressure impactor. *Journal of Aerosol Science*, *23*(4), 353–360.

Kuuluvainen, H., Arffman, A., Saukko, E., Virtanen, A., & Keskinen, J. (2013). A new method for characterizing the bounce and charge transfer properties of nanoparticles. *Journal of Aerosol Science*, *55*, 104–115.

Kuuluvainen, H., Karjalainen, P., Bajamundi, C.J.E., Maunula, J., Vainikka, P., Roppo, J., Keskinen, J., & Rönkkö, T. (2015). Physical properties of aerosol particles measured from a bubbling fluidized bed boiler. *Fuel*, *139*, 144–153.

Rennecke, S., & Weber, A. (2013a). The critical velocity for nanoparticle rebound measured in a low pressure impactor. *Journal of Aerosol Science*, *58*, 135–147.

Rennecke, S., & Weber, A. (2013b). A novel model for the determination of nanoparticle impact velocity in low pressure impactors. *Journal of Aerosol Science*, *55*, 89–103.

Reuter-Hack, K., Weber, A.P., Rösler, S., & Kasper, G. (2007). First LDA measurements of nanoparticle velocities in a low-pressure impacting jet. *Aerosol Science and Technology*, *41*(3), 277–283.

Ristimäki, J., Virtanen, A., Marjamäki, M., Rostedt, A., & Keskinen, J. (2002). On-line measurement of size distribution and effective density of submicron aerosol particles. *Journal of Aerosol Science*, *33*(11), 1541–1557.

Rogers, L.N., & Reed, J. (1984). The adhesion of particles undergoing an elastic-plastic impact with a surface. *Journal of Physics D: Applied Physics*, *17*(4), 677–689.

Saukko, E., Kuuluvainen, H., & Virtanen, A. (2012). A method to resolve the phase state of aerosol particles. *Atmospheric Measurement Techniques*, *5*(1), 259–265.

Scheibel, H.G., & Porstendörfer, J. (1983). Generation of monodisperse Ag- and NaCl-aerosols with particle diameters between 2 and 300 nm. *Journal of Aerosol Science*, *14*(2), 113–126.

Schmidt-Ott, A. (1988). New approaches to *in situ* characterization of ultrafine agglomerates. *Journal of Aerosol Science*, *19*(5), 553–563.

Seipenbusch, M., Rothenbacher, S., Kirchhoff, M., Schmid, H.-J., Kasper, G., & Weber, A. (2010). Interparticle forces in silica nanoparticle agglomerates. *Journal of Nanoparticle Research*, *12*(6), 2037–2044.

Seipenbusch, M., Toneva, P., Peukert, W., & Weber, A.P. (2007). Impact fragmentation of metal nanoparticle agglomerates. *Particle and Particle Systems Characterization*, *24*(3), 193–200.

Tsai, C.-J., Pui, D.Y., & Liu, B.Y. (1990). Capture and rebound of small particles upon impact with solid surfaces. *Aerosol Science and Technology*, *12*(3), 496–507.

Virtanen, A., Joutsensaari, J., Koop, T., Kannosto, J., Yli-Pirilä, P., Leskinen, J., Mäkelä, J.M., Holopainen, J.K., Pöschl, U., Kulmala, M., Worsnop, D.R., & Laaksonen, A. (2010). An amorphous solid state of biogenic secondary organic aerosol particles. *Nature*, *467*(7317), 824–827.

Virtanen, A., Kannosto, J., Kuuluvainen, H., Arffman, A., Joutsensaari, J., Saukko, E., Hao, L., Yli-Pirilä, P., Tiitta, P., Holopainen, J.K., Keskinen, J., Worsnop, D.R., Smith, J.N., & Laaksonen, A. (2011). Bounce behavior of freshly nucleated biogenic secondary organic aerosol particles. *Atmospheric Chemistry and Physics*, *11*(16), 8759–8766.

Wall, S., John, W., Wang, H.-C., & Goren, S.L. (1990). Measurements of kinetic energy loss for particles impacting surfaces. *Aerosol Science and Technology*, *12*(4), 926–946.

Wang, H.-C., & John, W. (1988). Dynamic adhesion of particles impacting a cylinder. In K.L. Mittal (Ed.), *Particles on Surfaces 1: Detection, Adhesion, and Removal*. Plenum Press: New York, pp. 211–224.

Wang, H.-C., & Kasper, G. (1991). Filtration efficiency of nanometer-size aerosol particles. *Journal of Aerosol Science*, *22*(1), 31–41.

Weir, G., & McGavin, P. (2008). The coefficient of restitution for the idealized impact of a spherical, nano-scale particle on a rigid plane. *Proceedings of the Royal Society A: Mathematical, Physical and Engineering Sciences*, *464*(2093), 1295–1307.

Zihlmann, S., Lüönd, F., & Spiegel, J.K. (2014). Seeded growth of monodisperse and spherical silver nanoparticles. *Journal of Aerosol Science*, *75*, 81–93.

Paper 4

Arffman A., Yli-Ojanperä, J., Kalliokoski, J., Harra, J., Pirjola, L., Karjalainen, P., Rönkkö, T., Keskinen J., A high-resolution low-pressure cascade impactor, *Journal of Aerosol Science*, 78, 97–109, 2014.

Journal of Aerosol Science 78 (2014) 97–109

Contents lists available at ScienceDirect

Journal of Aerosol Science

journal homepage: www.elsevier.com/locate/jaerosci

High-resolution low-pressure cascade impactor

A. Arffman [a,*], J. Yli-Ojanperä [a], J. Kalliokoski [a], J. Harra [a], L. Pirjola [b],
P. Karjalainen [a], T. Rönkkö [a], J. Keskinen [a]

[a] *Tampere University of Technology, Department of Physics, Aerosol Physics Laboratory, P.O. Box 692, FI-33101 Tampere, Finland*
[b] *Metropolia University of Applied Sciences, Department of Technology, P.O. Box 4021, FIN-00180 Helsinki, Finland*

A R T I C L E I N F O

Article history:
Received 5 May 2014
Received in revised form
19 August 2014
Accepted 25 August 2014
Available online 3 September 2014

Keywords:
Low-pressure impactor
Cut-curve
Cutpoint
ELPI
NanoMOUDI

A B S T R A C T

This study introduces the calibration and performance evaluation of a new high-resolution low-pressure cascade impactor (HRLPI). It is a 10-stage cascade impactor designed to be used with the electrical detection of aerosol particles. The particle size range with the filter stage is approximately from 5 nm to 200 nm, and the flow rate is 1.2 lpm. The cutpoint of the first stage is 7.7 nm, which is so far the lowest cutpoint introduced for cascade impactors. The HRLPI stages have sharp cut-curves, which improve the performance significantly when the cutpoints are brought as close to each other as in the HRLPI. The HRLPI was calibrated with monodisperse dioctylsebacate particles. The average cut-curve steepness parameter was 9.9, and for the ELPI+ the corresponding value was 3.5. The HRLPI was tested in laboratory measurements together with five other commercial instruments. The HRLPI could resolve the location of the size distribution mode down to 10 nm, whereas for the ELPI with an additional low cutpoint stage, the minimum size was around 24 nm. Measurements also showed that the HRLPI and SMPSs were the only instruments of the tested five size-distribution measurement instruments that could resolve a bimodal distribution in which the geometric mean diameters of the modes were around 15 nm and 30 nm.

1. Introduction

The trend in the last few latest decades in aerosol science (e.g., in emission, synthesis, and atmospheric research) has been towards nanoparticles and real-time measurement (Harra et al., 2012; Kulmala et al., 2004; Lähde et al., 2009; Mädler et al., 2002; Shi et al., 2001). One wide class of instruments used in measuring the particle size distribution of aerosol is cascade impactors (see, e.g., Marple, 2004). To measure nanosized particles, low-pressure impactors (LPI) have been introduced. In cascade low-pressure impactors, the pressure is reduced either by having a separate pressure-reducing stage (e.g., Hering et al., 1978,1979) or by gradually reducing the pressures by using high jet velocities (e.g., Berner, 1972; Vanderpool et al., 1990). To make LPI measurements in real-time and to improve the sensitivity, Keskinen et al. (1992) developed the electrical low-pressure impactor (ELPI).

---

* Corresponding author.
E-mail addresses: anssi.arffman@tut.fi (A. Arffman), jaakko.yli-ojanpera@tut.fi (J. Yli-Ojanperä), joni.kalliokosi@tut.fi (J. Kalliokoski), juha.harra@tut.fi (J. Harra), liisa.pirjola@metropolia.fi (L. Pirjola), panu.karjalainen@tut.fi (P. Karjalainen), topi.ronkko@tut.fi (T. Rönkkö), jorma.keskinen@tut.fi (J. Keskinen).

http://dx.doi.org/10.1016/j.jaerosci.2014.08.006
0021-8502/

The performance of a cascade impactor is difficult to define unambiguously because no single parameter can describe it. It should include the number of the measurement channels per order of magnitude in the size axis, the time response, the shape of the kernel functions, and the sensitivity of the instrument. This study investigates performance mainly from the perspective of distinguishing both modes of bimodal size distributions and determining the lower limit at which the relevant information from a size distribution can still be resolved. At the moment, if we confine the parameters to the particle size range less than 100 nm and to cascade impactors, the largest number of measurement channels is found with the ELPI+ (Järvinen et al., 2014) and NanoMOUDI (MSP Corporation). The ELPI+ has three stages in the size range, and its lowest cutpoint is 17 nm, whereas the NanoMOUDI has four stages, and its lowest cutpoint is 10 nm.

In this study, we introduce and characterize a new high-resolution low-pressure cascade impactor (HRLPI). The HRLPI has eight stages in the size range under 100 nm, and its lowest cutpoint stage is 7.7 nm. The impactor was first calibrated with monodisperse dioctylsebacate (DOS) particles, and then its performance was compared to five commercial instruments in laboratory conditions by measuring uni- and bimodal size distributions generated from DOS and NaCl. Finally, the instrument is compared to an extra-stage low-pressure impactor (EELPI, Yli-Ojanperä et al. 2010a) and an Engine Exhaust Particle Sizer (EEPS, TSI Inc.) in a transient measurement, where the emissions of a modern passenger car diesel engine were measured over the US06 cycle.

2. Description of instrument

The HRLPI is a ten stage, low-pressure cascade impactor. The lowest cutpoint is 7.7 nm, and the largest cutpoint is 142 nm. The impactor operates in the pressure range of 8–39.5 mbar, and the pressure is reduced from the atmospheric conditions using a separate pressure reduction inlet. The total number of stages has been restricted to 10 in order to prevent too high nanoparticle losses in the upper stages. The essential features of the HRLPI are short-throated slit-type nozzles (Arffman et al., 2012), and an electrical detection method (Keskinen et al., 1992). The short-throated nozzles provide sharp cut-curves, which allow narrow measurement channels without significant overlapping of the kernels. The electrical detection provides a high sensitivity for nanoparticles and a real-time detection of the particle size distribution.

2.1. Inlet and charger

A separate pressure reduction inlet is used in the HRLPI to reduce the pressure from atmospheric conditions to the upstream pressure of the highest cutpoint stage. The inlet is constructed from a set of critical orifices and a minor bypass flow after them. The adjustable bypass is needed for fine tuning the upstream pressure, for example, when the ambient pressure changes. A few different inlet configurations were tested experimentally in order to achieve a high penetration throughout the complete measurement size range.

A self-made, unipolar corona charger was placed before the HRLPI in order to enable the electrical detection of the particles. The corona current was kept constant (1 μA) by adjusting the voltage (2–3 kV). The charger was calibrated in the size range of 3.5–150 nm with Ag, DOS, and NaCl particles.

2.2. Impactor

The HRLPI stages have slit-type nozzles and short jet-to-plate distances. The flow rate of the impactor is 1.2 lpm. The upstream and downstream pressures of the impactor are 39.5 mbar and 8 mbar, respectively. Table 1 shows the important dimensions and parameters of the stages and the measured stage pressures (stagnation pressure downstream of each impactor stage). Figure 1 shows a schematic cross section of the HRLPI inlet, two impactor stages, and the filter stage. Pressure-measuring taps are also shown. Stages are composed of the following parts: a body, a nozzle plate, a collection plate, an insulation ring, a spacer ring between the collection plate and the body, and a support for the nozzle plate. All parts

Table 1
Dimensions of the HRLPI stages. L is the length of the slit, W the width of the slit, T the length of the nozzle throat, S the jet-to-plate distance, P_d the downstream pressure of the stage, and V_j the adiabatic jet velocity calculated from the measured stage pressures. The inlet pressure of the stage 10 is 39.5 mbar.

Stage	L (mm)	W (mm)	T (mm)	S (mm)	T/W	S/W	P_d (mbar)	V_j (m/s)
1	26	0.4	0.1	0.7	0.25	1.75	7.98	238
2	22	0.3	0.1	0.5	0.33	1.66	12.93	216
3	20	0.3	0.1	0.5	0.33	1.66	19.51	152
4	20	0.3	0.1	0.5	0.33	1.66	24.32	119
5	20	0.3	0.1	0.5	0.33	1.66	27.94	111
6	22	0.3	0.1	0.5	0.33	1.66	31.61	87
7	24	0.3	0.1	0.5	0.33	1.66	34.12	78
8	27	0.3	0.1	0.5	0.33	1.66	36.28	62
9	20	0.4	0.1	0.7	0.25	1.75	37.74	60
10	23	0.4	0.1	0.7	0.25	1.75	39.17	45

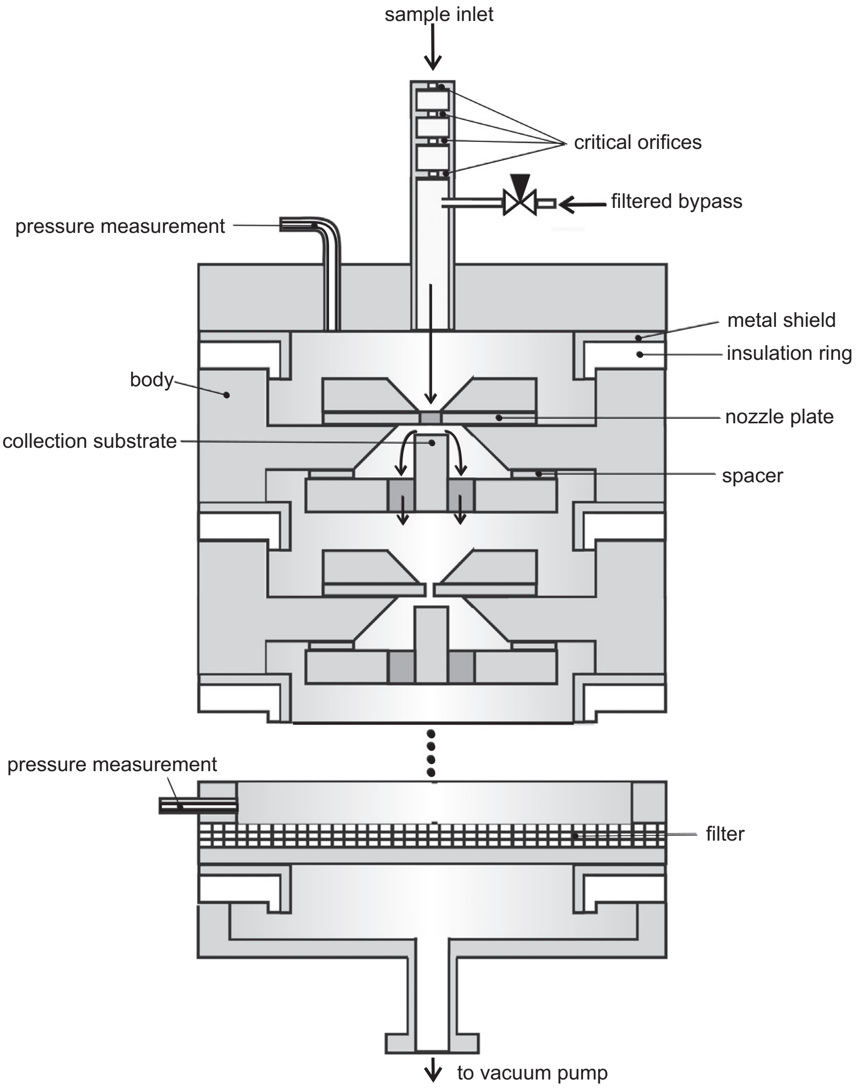

Fig. 1. Schematic cross section of HRLPI with inlet and filter stage.

are bolted together by two screws. Insulation rings are covered by metal shields to prevent the insulator from being seen by the particles in order to decrease Coulombic particle losses.

3. Calibration methods

3.1. Inlet and charger

The inlets were calibrated using a reference Faraday cup electrometer (FCE). The inlets were assembled to the impactor part as in the normal measurement configuration. The reference FCE measured the concentration of the particles before the impactor, and the concentration after the inlet was measured by the impactor. The penetration of the inlet was calculated from the measured currents with the following equations:

$$P_{inlet} = \frac{I_{impactor}}{I_{fce}} \tag{1}$$

$$I_{impactor} = \sum_{i=0}^{n} I_i, \tag{2}$$

where n is the number of the impactor stages and $i=0$ is the filter stage. The particles were generated using a single charged aerosol reference (SCAR, Yli-Ojanperä et al., 2010b) in a similar way as in the case of the impactor calibrations.

The charger was calibrated using DOS, NaCl, and silver particles generated with evaporation–condensation techniques. Monodispersity was accomplished with a differential mobility analyzer (DMA) after the particle generators. The DOS calibrations were performed with a method described in Marjamäki et al. (2000), whereas the method used in the NaCl and Ag calibrations can be found in Marquard et al. (2006).

3.2. Impactor

The impactor was calibrated using DOS particles. The particle sizes up to 30 nm were produced by using an evaporation–condensation particle generator (ECG). Particle sizes above 30 nm were produced using the SCAR instrument. The lowest particle sizes were produced with an evaporation–condensation generator because the particles produced by the SCAR include a 10 nm NaCl nucleus that has higher density than pure DOS particles. After the generation, the particles were size classified using a TSI's 3071 DMA that was coupled to the impactor inlet. The impactor was fitted to the ELPI impactor body, and the calibration was performed using the electrical calibration method presented by Keskinen et al. (1999).

The collection efficiency of each stage was calculated from the measured stage currents with the following equation:

$$E_i = \frac{I_i}{\sum_{k=0}^{i} I_k}, \tag{3}$$

where I_i is the current measured from the ith stage. Stage numbering is so that the filter stage corresponds to the index $i=0$, the lowest cutpoint stage corresponds to $i=1$, the second lowest stage $i=2$, etc. The essential property of the calibration particles produced by the SCAR is that the particles are singly charged. This way, multiple-charge correction is not needed.

The kernel functions of the impactor were calculated with the following equations:

$$\begin{aligned} &k_n(D_p) = E_n(D_p) \\ &k_i(D_p) = E_i(D_p) \prod_{j=i+1}^{n} [1 - E_j(Dp)], \quad i = (0), 1, \ldots, n-1, \end{aligned} \tag{4}$$

where E_n is the highest cutpoint stage collection efficiency and index $i=0$ corresponds to the filter stage. E_js also include the particle losses that are caused by diffusion, and image charging effects. E_js were calculated with the following equations:

$$E_j = 1 - (1 - E_j^I)(1 - E_j^S), \tag{5}$$

where E_j^I is the collection efficiency by impaction, and E_j^S is the collection efficiency by secondary collection mechanism, i.e., diffusion and image charge. If one wants to simulate the impactor response, the currents measured by the stages can be determined from the kernel functions:

$$I_i = \int_{D_{p,min}}^{D_{p,max}} k_i(D_p) E_{ch} f(D_p)\, dDp, \tag{6}$$

where $f(D_p)$ is the particle size distribution and E_{ch} is the charging efficiency.

4. Results of calibration

4.1. Inlet and charger

Four different types of pressure-reducing inlets (valve + critical orifices) were characterized. Figure 2 shows schematically the three different valve types. The fourth one is similar to the one in Fig. 2(a) but there are only two critical orifices. Figure 2(a) shows the bypass inlet that was chosen to be used in the HRLPI. The flow rate through the critical orifices is approximately 1.1 lpm, and the bypass is from 0 to 0.1 lpm depending on ambient pressure. Figure 2(b) shows the micrometer valve inlet with four critical orifices, and Fig. 2(c) the needle valve inlet.

The results of the calibrations are shown in Fig. 3. Penetrations are shown as a function of the aerodynamic diameter, and the inlet of the HRLPI is shown with blue squares. For comparison, the penetration of the Aerodyne AMS (Liu et al., 2007)

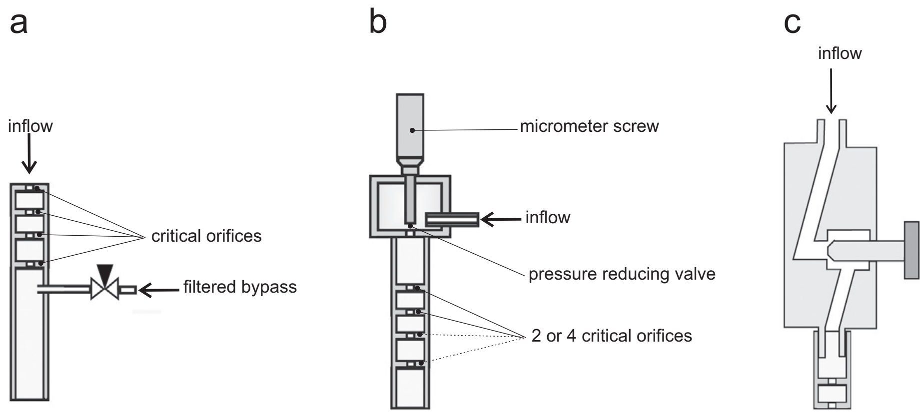

Fig. 2. Schematic of inlets: (a) bypass inlet; (b) micrometer valve inlet; (c) needle valve.

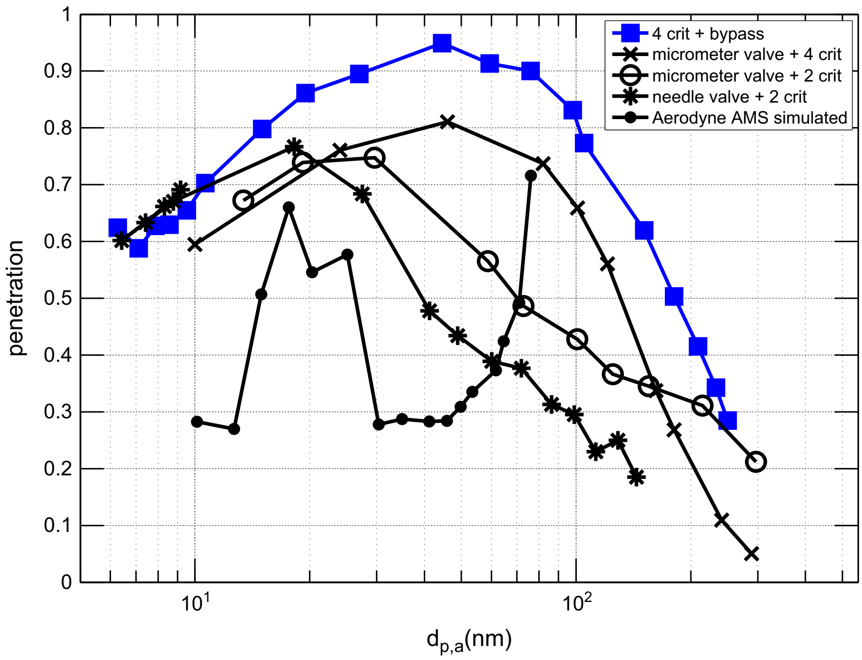

Fig. 3. Penetrations of the different pressure-reduction inlets as a function of the aerodynamic particle diameter. The penetration of the Aerodyne AMS inlet is adapted from Liu et al. (2007). (For interpretation of the references to color in this figure caption, the reader is referred to the web version of this paper.)

inlet is also shown. All of the curves except the AMS have a similar profile. In the size range of 10–40 nm, penetrations drop because of diffusion, and in the upper end, impaction decreases the penetration. The more detailed shapes are difficult to explain, but some reasoning can be given.

Increasing the number of pressure-reducing critical orifices increases the penetration in the impaction collection region. This implies that there are some losses in the critical orifices or in the valve that decrease when the pressure drop over the components is decreased. Some simulation efforts were made to reveal the location of the inertial losses. Simulations implied that the inertial losses would occur solely in the valve part. The problem with the simulations was that the results were very sensitive to the geometric parameters. Nevertheless, combining experimental results and numerical observation suggests that the inertial losses would decrease because the flow velocity decreases in the valve flow path.

Also, the effect of the valve type on the penetration can be roughly estimated. Fewer turnings in the valve lead to higher penetration in the inertial collection region. Around 10 nm, the micrometer valve has lower penetration than the needle valve because of the larger residence time in the micrometer valve.

The AMS inlet is composed of serially connected components: a critical orifice, a valve body, and an aerodynamic lens. It decreases the sample pressure from the atmospheric conditions to approximately 1 mbar, and the aerodynamic lens focuses particles into a beam. The pressure drop across the AMS inlet is quite different compared to the inlet of the HRLPI, but this was the closest similar type of pressure-dropping inlet that we found from the literature. The penetration of the AMS inlet increases rapidly above 70 nm because there are no steep flow path turns in the AMS inlet. The measurement size range of the AMS is approximately 40–1000 nm.

Figure 4 shows the calibration results of the corona charger. The result is the Pn-curve of the charger (penetration multiplied by the average number of charges per particle). The results obtained with different particle materials and calibration methods are consistent with each other. The slope of the logarithm of the Pn-curve changes around 10 nm because the charging efficiency decreases and the losses of the charged particles increase. Therefore, two different parametrizations were fitted to the measurement results. The fittings are shown in the following equation:

$$E_{ch} = Pn(d_p) = \begin{cases} 2.811 \times 10^5 \cdot d_p^{2.937}, & d_p < 0.0092\ \mu\text{m} \\ 111.2 \cdot d_p^{1.267}, & d_p \geq 0.0092\ \mu\text{m}. \end{cases} \tag{7}$$

4.2. Impactor collection efficiencies

The collection efficiencies of the stages were measured using the electrical calibration method, as already discussed in Section 3.2. Figure 5 presents the results of the calibration of the inlet and the HRLPI impactor. Crosses represent the measured collection efficiencies, plus signs the diffusion loss corrected collection of the stage 1, open dots the collection efficiency of the inlet, and lines the fittings to the measurements. Numbers indicate the different stages. The fittings are composed of two parts, impaction collection (E^I) and diffusion losses (E^s; Brockmann, 2001), as shown in Eq. (5). The fitted

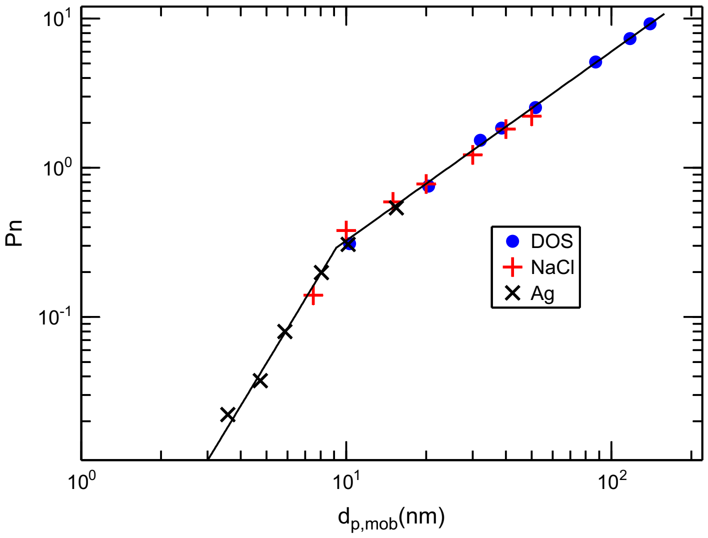

Fig. 4. Pn-curve of the corona charger used in this study.

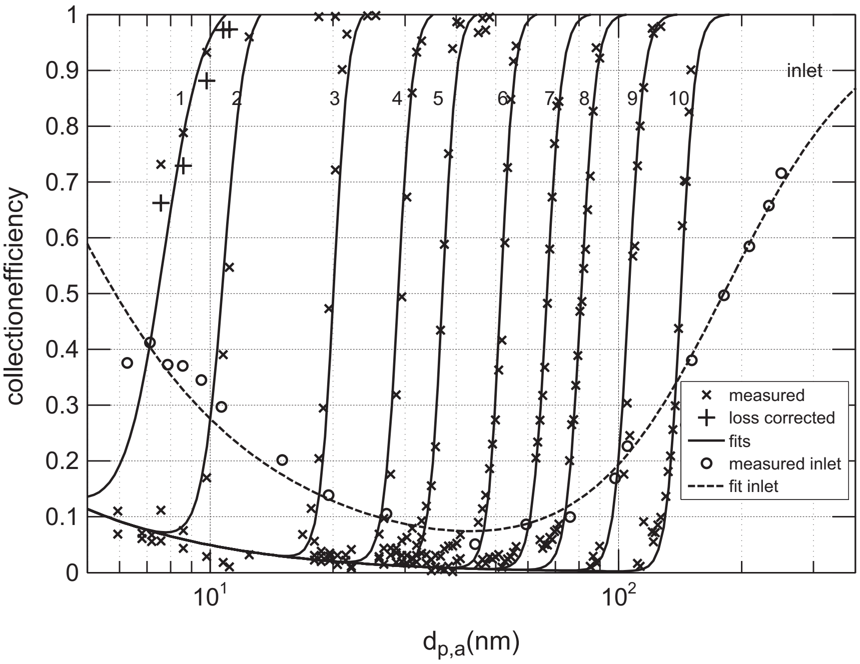

Fig. 5. Collection efficiencies of the HRLPI stages as a function of the aerodynamic particle diameter. For the stage 1, the diffusion corrected collection efficiency is shown with "+" marks. Lines are the fittings.

Table 2
Values of the fitted parameters for each stage and the inlet.

Stage	$d_{p,50}$ (nm)	s	L (m)
1	7.7	5	0.01
2	10.8	8.1	0.01
3	19.5	12.2	0.01
4	28.7	11.5	0.01
5	37.6	12.7	0.01
6	51.5	13.5	0.01
7	66.8	11.9	0.01
8	81	12.1	0.01
9	105.9	12	0.01
10	142	12.6	0.01
Inlet	183	–	–

functions are of the form

$$E^I = (1 + (d_{p,50}/d_p)^{(2s)})^{-1} \tag{8}$$

$$E^S = 1 - e^{kSh} \tag{9}$$

$$k = \frac{\pi DL}{Q}$$

$$Sh = 3.66 + \frac{0.2672}{k + 0.10079k^{(1/3)}},$$

where $d_{p,50}$ is the cutpoint of the stage, s a fitting parameter (describes the steepness of the collection efficiency curve), D the diffusion coefficient (m^2/s), L the effective length of the tube (m), and Q the volumetric flow rate (m^3/s). The fitted parameters are the cutpoints, steepnesses, and the effective tube length. Table 2 presents the results of the fitting. The volumetric flow rate (Q) is 1.2 lpm for all cases.

All the stages except the first have similar steepnesses. These steepnesses correspond very well with the slit-type impactor collection efficiency curves that were introduced in a previous paper by the authors (Arffman et al., 2012). In that paper, a single-stage LPI with a short nozzle throat was numerically simulated and experimentally investigated and found to have very high cut-curve steepness. The "tails" of the stages are caused by the diffusion and image charge losses. The lower steepness of the stage 1 collection efficiency may be caused by the uncertainty in the diffusion loss correction that was performed, i.e., there is uncertainty in the fitting of the losses curve.

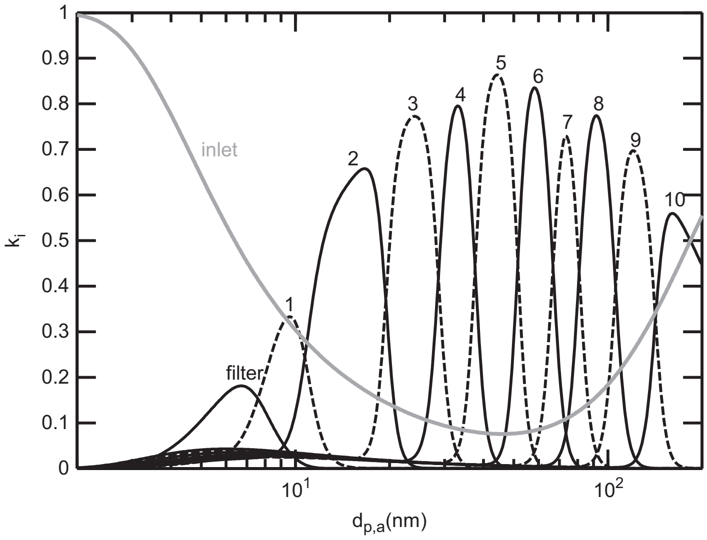

Fig. 6. Kernels of the HRLPI as a function of the aerodynamic particle diameter.

Table 3
Cutpoints and collection efficiency curve steepness parameters of the HRLPI, ELPI+ (Järvinen et al., 2014), and NanoMOUDI (MSP Corporation).

Stage	HRLPI			ELPI+			NanoMOUDI		
	$d_{p,50}$	s	k_{height}	$d_{p,50}$	s	k_{height}	$d_{p,50}$	s	k_{height}
1	7.7	5	0.33	15.7	3.3	0.66	9.7	2.1	0.60
2	10.8	8.1	0.60	30.4	3.7	0.73	17.7	2.2	0.60
3	19.5	12.2	0.77	54.1	3.9	0.72	31.1	2.2	0.64
4	28.7	11.5	0.79	94.3	3.1	0.64	52.5	3.1	0.79
5	37.6	12.7	0.86	154	3.6	0.69	98.1	3.6	0.83
6	51.5	13.5	0.84				172	5.0	0.88
7	66.8	11.9	0.73						
8	81	12.1	0.77						
9	105.9	12	0.70						
10	142	12.6	0.56						

4.3. Impactor kernels

Figure 6 shows the kernels of the HRLPI. The penetration of the inlet mainly reduces the height of the outermost stage kernels. The first and the seventh channel have the narrowest measurement size ranges, which further reduce the heights of their kernels.

Table 3 lists the cutpoints, the collection efficiency curve steepnesses, and the kernel heights of the HRLPI, the ELPI+, and the NanoMOUDI impactors (stages with $d_{p,50} < 200$ nm). The height of the HRLPI kernels is in the same order with the ELPI+ and the NanoMOUDI, although the measurement channels are much narrower in the HRLPI than in the ELPI+ or the NanoMOUDI.

The average logarithmic channel width, $\log(d_{p,50,i+1}/d_{p,50,i})$, is 0.36 for the HRLPI and approximately 0.6 for the ELPI+ and for the NanoMOUDI. Despite the narrow measurement channels, the HRLPI has less cross talk between the consecutive stages compared to the ELPI+ and the NanoMOUDI. To quantify the amount of cross talk, the portion of the stage i current signal that is caused by the particles belonging to the size interval, $d_{p,50,i} - d_{p,50,i+1}$, can be calculated. This portion is on the average 69% in the HRLPI and 61% and 62% in the ELPI+ and the NanoMOUDI, respectively (excluding particles smaller than 7 nm). This is mostly a consequence of the lower steepness of the collection efficiency curves of the EELPI and the NanoMOUDI ($s \approx 3$–4) compared to the HRLPI ($s \approx 11$–12). The adjacent stages start to collect the particles of the same size when the collection efficiency curves of the stages overlap.

5. Test measurements

The performance of the HRLPI was tested in the laboratory and in the field measurements. In the laboratory measurements, the HRLPI was compared to other instruments by measuring DOS and NaCl particles. In the field tests, the HRLPI was compared to other real-time instruments by measuring the particulate matter emissions of a passenger car operated with diesel over a transient driving cycle.

Table 4
List of compared instruments in the laboratory measurements. TSI's 3025 Ultrafine CPCs were used in the NanoSMPS and LongSMPS configurations.

Manufacturer/instrument	Abbreviation	Measurement range (nm)	Flow rates (lpm)
TSI/Nano SMPS	NanoSMPS	2–65	Sample 1.5, Sheath 15
TSI/Long SMPS	LongSMPS	10–245	Sample 1.5, Sheath 15
TSI/Engine Exhaust Particle Sizer	EEPS	5.6–560	10
Dekati/Classic ELPI	EELPI	6–10,000	10
Dekati/ELPI+	ELPI+	6–10,000	10
–/HRLPI	HRLPI	3–200	1

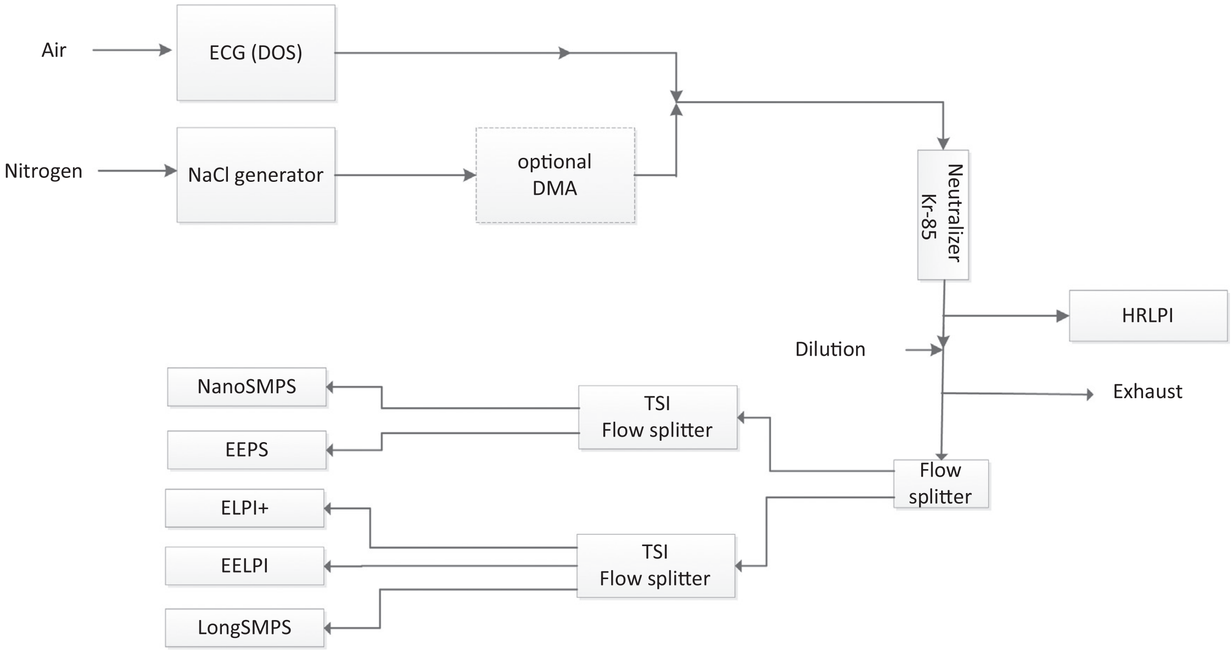

Fig. 7. Measurement setup of laboratory experiments.

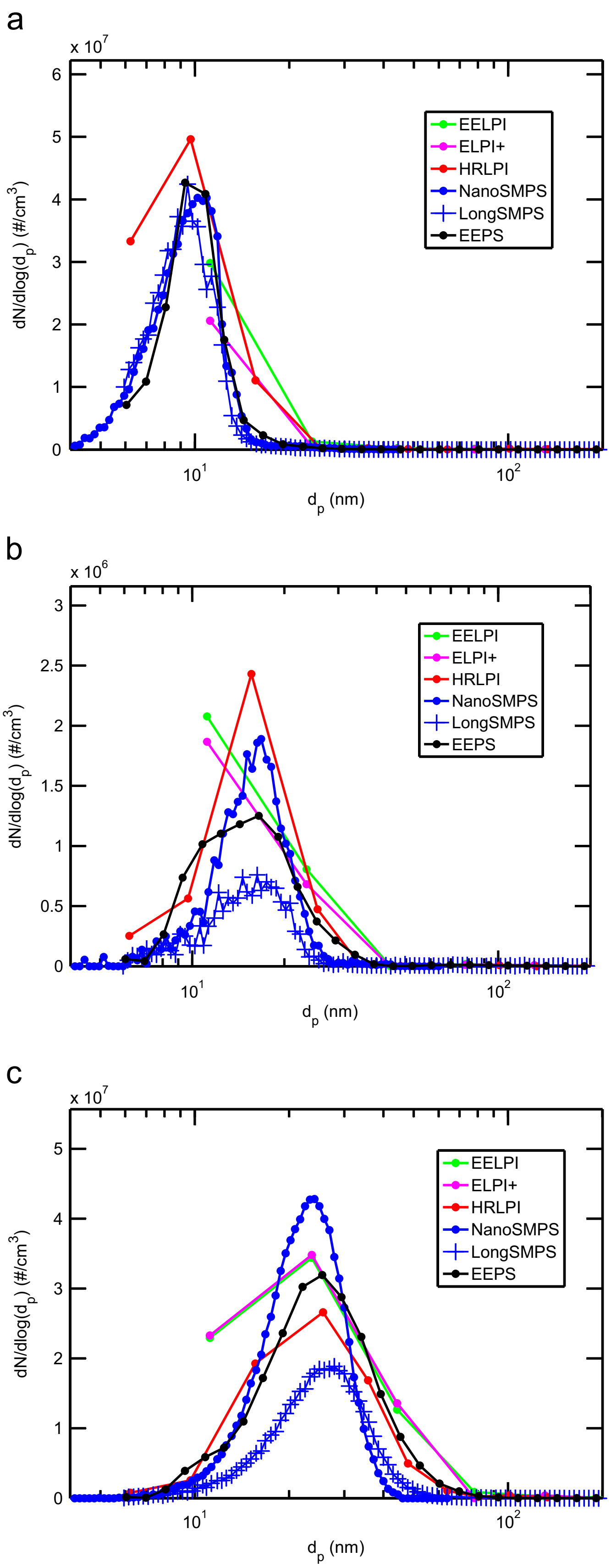

Fig. 8. DOS size distributions measured by different instruments. GMD is the geometric mean diameter of the NanoSMPS size distribution. (a) GMD 10 nm, (b) GMD 17 nm, and (c) GMD 24 nm.

5.1. Laboratory tests

The HRLPI was compared in laboratory measurements with five commercial instruments. Instruments, corresponding abbreviations, measurement size ranges, and flow rates are shown in Table 4. Size ranges are in the mobility or aerodynamic diameters, depending on the classification method of the corresponding instrument. The HRLPI, EELPI, and ELPI+ particle size distributions were calculated using the cutpoint concept (Kauppinen et al., 1986; Keskinen et al., 1992). The correction for fine particle losses was performed as presented by Moisio et al. (1999), and the penetration of the inlet was included in the calculation of the size distributions. The EEPS and SMPSs results were exported using the measurement software's export.

Figure 7 presents the laboratory measurement setup. The sample flow was diluted after the HRLPI in order to have similar current signal levels for the HRLPI as for the EELPI and the ELPI+. The EELPI was used without a trap voltage, and the ELPI+ was used in the default factory settings, which include the trap voltage (20 V). The electrometer zero levels were subtracted from the measured signals. Charger ions collected by the few highest cutpoint stages in the EELPI, and the measurement artefact introduced by the ions were compensated with the zero level correction. The dilution ratio and the sampling line losses were also corrected from the measured size distributions.

Figure 8 shows the measured DOS particle size distributions generated with the ECG. The aerodynamic size distributions measured by the impactors were transformed to mobility size distributions assuming the bulk density of DOS (920 kg/m^3). From the figure, it can be seen that when the GMD is 24 nm, all of the instruments perform quite well. In the case of a GMD of 17 nm, the HRLPI, SMPSs, and EEPS can show the shape of the size distribution. In the EELPI and ELPI+, particles are mostly collected by the filter stage and by the lowest cutpoint stage, and thus the shape is not any more fully resolved. When the GMD is reduced to 10 nm, the HRLPI, EEPS, and SMPSs can still resolve the mode location of the size distributions.

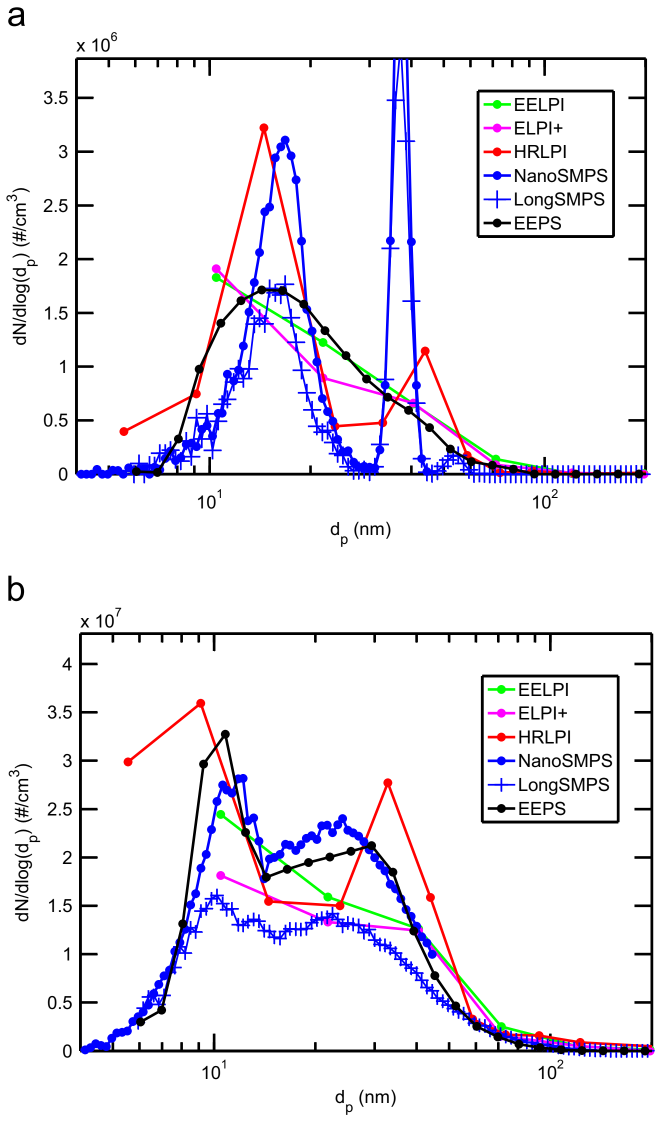

Fig. 9. DOS and NaCl particles externally mixed and measured by different instruments: (a) DOS mode is on the left and NaCl (classified by DMA) on the right; (b) overlapping DOS and NaCl size distributions.

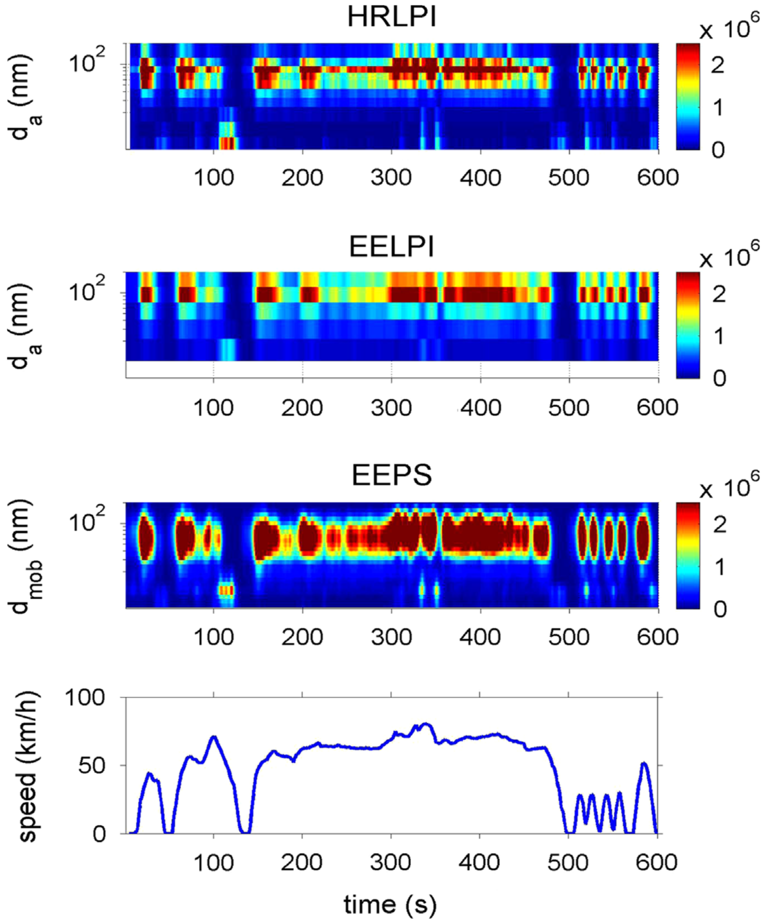

Fig. 10. Exhaust particle number size distributions measurement results from a passenger car diesel engine over a transient US06 cycle with the HRLPI, EELPI and EEPS. On the horizontal axis is the time, and the color shows the number concentration in unit #/cm^3. The bottom graph is the vehicle speed over the cycle. (For interpretation of the references to color in this figure caption, the reader is referred to the web version of this paper.)

The EEPS and SMPSs also measure the left side of the distribution in more detail than the HRLPI. It is unclear why the LongSMPS showed lower concentrations when the GMDs were larger than 10 nm. A similar trend was observed throughout the laboratory measurements.

Figure 9 presents externally mixed DOS and NaCl aerosol particle size distributions measured by different instruments. The DOS particles were generated by the ECG, and the NaCl particles were generated by evaporating NaCl in a tube furnace and then rapidly diluting the vapour to almost room temperature. In Fig. 9(a), the NaCl aerosol is first classified by the DMA, and after that, it is mixed with polydisperse DOS aerosol. In Fig. 9(b), the polydisperse DOS and NaCl particles are directly mixed after they have been generated.

The HRLPI performs very well in both bimodal cases. In Fig. 9(a), the concentration of the narrow NaCl mode measured by the HRLPI is lower compared to the SMPS because aerodynamic size distributions are calculated assuming unit density for the particles. If the correct effective density would be used for the NaCl mode, the Pn-values would be smaller, which would bring the concentrations of the HRLPI to the same level as in the SMPS distributions. However, when the effective densities of the particles are not known, the size distributions measured by the impactor are usually calculated assuming unit density. Steep cut-curves and a higher number of measurement channels significantly improve the resolving power of the HRLPI in the size distribution measurement, as compared to the EELPI and the ELPI+. The distance between the modes is slightly smaller in the distributions measured by the SMPSs and EEPS than by the HRLPI. This is an expected result, as the effective density of the NaCl particles in this size range is larger than 1 g/cm^3, and correspondingly, their aerodynamic size is larger than the mobility size. The EEPS resolves clearly only one mode in Fig. 9(a). This could be explained, for example, by the high smoothness assumption in the inversion of the size distribution.

5.2. Field measurements: comparison to EEPS and EELPI

The transient performance of the instrument was tested by measuring particulate emissions of a passenger car engine operated with diesel in a chassis dynamometer. The diesel passenger car emissions were measured during the US06 driving cycle. The exhaust sampling and dilution was performed using a partial flow sampling system (porous tube diluter) described by Ntziachristos et al. (2004). The total dilution ratio in the whole sampling system was about 150. In order to study the entire interesting particle size range, the exhaust gas sample was extracted from a sampling location upstream of the aftertreatment system consisting of a diesel oxidation catalyst (DOC) and a diesel particulate filter (DPF). Figure 10 shows the number size distribution measured by the HRLPI, EELPI, and EEPS, and corrected by the total dilution ratio. For the readers more interested in emissions, the vehicle speed is also shown at the bottom of the figure. The results of the instruments correlate temporally, and in particle size. All instruments measure the mode around 10 nm, and the soot mode around 100 nm. The distributions measured by the EEPS are wider, and consequently, the total concentrations are higher compared to the HRLPI (approximately 15% on average). The size distributions by the HRLPI are narrower because of the fractal structure of soot particles (Maricq & Xu, 2004). The effective density of the soot particles increases with decreasing particle size. Thus, the aerodynamic particle size spectrum is narrower than the mobility size spectrum. The EELPI and the HRLPI show quite similar results except the width of the soot mode size distribution and the concentration of the nucleation mode particles. The size distributions of the EELPI are wider because it has coarser resolution compared to the HRLPI. The lower concentration of the nucleation mode in the EELPI results is mostly caused by the lack of information on the *Pn*-values in the size range below 10 nm, as was already discussed in the previous section.

6. Summary & conclusions

In this study, a new high-resolution low-pressure impactor (HRLPI) was built, characterized, and performance tested. The HRLPI has 10 stages; the lowest cutpoint is 7.7 nm, and the highest 142 nm. The upstream and downstream pressures of the HRLPI are 39.5 mbar and 8 mbar, respectively, and the total flow rate is 1.2 lpm. The cutpoint of the first stage of the HRLPI is only 7.7 nm, which is by far the lowest cutpoint stage introduced for cascade impactors. The HRLPI employs impactor stages with sharp cut-curves that were presented in a previous study of the authors (Arffman et al., 2012). Sharp cut-curves improve the performance significantly when the cutpoints are brought as close to each other as in the HRLPI.

The impactor and the inlet were fully calibrated with monodisperse DOS particles. Most of the kernels peak at 0.8 to 0.9, and cross talk between the channels is only between the consecutive stages. This is a good result because the measurement channels are narrower compared to other commercially available cascade impactors (approximately 60% narrower than, e.g., in the ELPI+ or the NanoMOUDI).

The performance of the HRLPI was tested in laboratory measurements and field tests. The HRLPI was compared with several commercially available instruments: TSI's NanoSMPS, LongSMPS, and EEPS, and Dekati's EELPI and ELPI+. The HRLPI and NanoSMPS showed similar size distributions for monomodal dioctylsebacate (DOS) particles where the GMDs were in the size range of 10–24 nm. Bimodal test aerosols were generated by externally mixing NaCl and DOS particles. In the case of a bimodal size distribution, where the DOS mode was located at around 15 nm and the NaCl at around 30 nm, only the SMPSs and the HRLPI were able to resolve the shape of the bimodal size distributions. Field measurements were performed by measuring the size distributions of a passenger car diesel exhaust in parallel with the EELPI and the EEPS during the transient US06 test cycle. Results of the instruments were consistent by taking into account that soot particles have fractal structure.

The HRLPI was found to be a well-suited cascade impactor for the cases where the interesting size range is approximately from 5 to 200 nm. Compared to other low-pressure impactors, it has better resolution, and the measurement size range is down to 7.7 nm. The sharp cut-curves of the stages make the interpretation of the measurement signal straightforward and reliable, as the cutpoint concept works very well with the HRLPI. Compared to the existing impactors, for example, the bimodal size distributions can be resolved with significantly better accuracy. Applications where the HRLPI can be very beneficial compared to other cascade impactors are, for example, the nanoparticle synthesis and the emission studies. By combining the mobility and aerodynamic particle size distribution measurement results of the EEPS and HRLPI, a real-time information about the effective density of the particles down to 7 nm can be determined.

Acknowledgments

This work was conducted in the MMEA research program of the Cluster for Energy and Environment (CLEEN Ltd.), funded by Tekes. Test measurements were performed in the measurement campaign of the TREAM project (trends in real-world particle emissions of diesel and gasoline vehicles) funded by Tekes, AGCO Power, Neste Oil Oyj, Dinex Ecocat Oy, and Oy Nanol Technologies Ab.

References

Arffman, A., Yli-Ojanperä, J., & Keskinen, J. (2012). The influence of nozzle throat length on the resolution of a low pressure impactor—An experimental and numerical study. *Journal of Aerosol Science*, *53*, 76–84.

Berner, A. (1972). Praktische Erfahrungen mit einem 20-Stufen-Impactor. *Staub-Reinhaltung der Luft*, *32*, 315.

Brockmann, J.E. (2001). Sampling and transport of aerosols. In: *Aerosol Measurement; Principles Techniques and Applications*. John Wiley & Sons, Inc., New Jersey (Chapter 8).

Harra, J., Mäkitalo, J., Siikanen, R., Virkki, M., Genty, G., Kobayashi, T., Kauranen, M., & Mäkelä, J.M. (2012). Size-controlled aerosol synthesis of silver nanoparticles for plasmonic materials. *Journal of Nanoparticle Research*, *14*(6), 870.

Hering, S.V., Flagan, R.C., & Friedlander, S.K. (1978). Design and evaluation of new low-pressure impactor. I. *Environmental Science & Technology*, *12*, 667–673.

Hering, S.V., Friedlander, S.K., Collins, J.J., & Richards, L.W. (1979). Design and evaluation of new low-pressure impactor. II. *Environmental Science & Technology*, *13*, 184–188.

Järvinen, A., Aitomaa, M., Rostedt, A., Keskinen, J., & Yli-Ojanperä, J. (2014). Calibration of the new electrical low pressure impactor (ELPI+). *Journal of Aerosol Science*, *69*, 150–159.

Kauppinen, E., Hillamo, R., Ruuskanen, J., Hakkarainen, T., & Rouhiainen, P. (1986). Theoretical and experimental study of particle collection characteristics of high-velocity multijet cascade impactors. *Journal Aerosol Science*, *17*, 506–510.

Keskinen, J., Marjamäki, M., Virtanen, A., Mäkelä, T., & Hillamo, R. (1999). Electrical calibration method for cascade impactors. *Journal of Aerosol Science*, *30*, 111–116.

Keskinen, J., Pietarinen, K., & Lehtimäki, M. (1992). Electrical low pressure impactor. *Journal of Aerosol Science*, *23*, 353–360.

Kulmala, M., Vehkamäki, H., Petäjä, T., Maso, M.D., Lauri, A., Kerminen, V.-M., Birmili, W., & McMurry, P. (2004). Formation and growth rates of ultrafine atmospheric particles: A review of observations. *Journal of Aerosol Science*, *35*(2), 143–176.

Lähde, T., Rönkkö, T., Virtanen, A., Schuck, T., Pirjola, L., Hämeri, K., Kulmala, M., Arnold, F., Rothe, D., & Keskinen, J. (2009). Heavy duty diesel engine exhaust aerosol particle and ion measurements. *Environmental Science & Technology*, *43*(1), 163–168.

Liu, P.S.K., Deng, R., Smith, K.A., Williams, L.R., Jayne, J.T., Canagaratna, M.R., Moore, K., Onasch, T., Worsnop, D.R., & Deshler, T. (2007). Transmission efficiency of an aerodynamic focusing lens system: Comparison of model calculations and laboratory measurements for the Aerodyne aerosol mass spectrometer. *Aerosol Science and Technology*, *41*, 721–723.

Mädler, L., Kammler, H., Mueller, R., & Pratsinis, S. (2002). Controlled synthesis of nanostructured particles by flame spray pyrolysis. *Journal of Aerosol Science*, *33*(2), 369–389.

Maricq, M., & Xu, N. (2004). The effective density and fractal dimension of soot particles from premixed flames and motor vehicle exhaust. *Journal of Aerosol Science*, *35*(10), 1251–1274.

Marjamäki, M., Keskinen, J., Chen, D.-R., & Pui, D.Y. (2000). Performance evaluation of the electrical low-pressure impactor (ELPI). *Journal of Aerosol Science*, *31*(2), 249–261.

Marple, V. (2004). History of impactors – the first 110 years. *Aerosol Science and Technology*, *38*, 247–292.

Marquard, A., Meyer, J., & Kasper, G. (2006). Characterization of unipolar electrical aerosol chargers – Part I: A review of charger performance criteria. *Journal of Aerosol Science*, *37*(9), 1052–1068.

Moisio, M., Marjamäki, M., Virtanen, A., & Keskinen, J. (1999). Correction algorithm for fine particle losses in cascade impactor. *Journal of Aerosol Science*, *30* (Supplement 1), S773–S774 (Proceedings of the 1999 European Aerosol Conference).

Ntziachristos, L., Giechaskiel, B., Pistikopoulos, P., & Samaras, Z. (2004). Performance evaluation of a novel sampling and measurement system for exhaust particle characterization. *SAE Technical Paper*, *01*, 1439.

Shi, J.P., Evans, D.E., Khan, A., & Harrison, R.M. (2001). Sources and concentration of nanoparticles (<10 nm diameter) in the urban atmosphere. *Atmospheric Environment*, *35*(7), 1193–1202.

Vanderpool, R., Lundgren, D., & Kerch, P. (1990). Design and calibration of an in-stack low-pressure impactor. *Aerosol Science and Technology*, *12*, 215–224.

Yli-Ojanperä, J., Kannosto, J., Marjamäki, M., & Keskinen, J. (2010a). Improving the nanoparticle resolution of the ELPI. *Aerosol and Air Quality Research*, *10*, 360–366.

Yli-Ojanperä, J., Mäkelä, J.M., Marjamäki, M., Rostedt, A., & Keskinen, J. (2010b). Towards traceable particle number concentration standard: Single charged aerosol reference (SCAR). *Journal of Aerosol Science*, *41*(8), 719–728.

Tampereen teknillinen yliopisto
PL 527
33101 Tampere

Tampere University of Technology
P.O.B. 527
FI-33101 Tampere, Finland

ISBN 978-952-15-3703-5
ISSN 1459-2045